Cardiff University

Computer simulations of biomolecules and membranes

Rangeen O Salih

A thesis submitted in fulfillment of the requirements for the degree of Doctor of Philosophy

School of Physics and Astronomy

29 September 2016

Abstract

The important properties of biological membranes such as elasticity and structure, and their interaction with nanoparticles is of great importance to nanomedicine applications such as drug delivery and gene therapy. This thesis reports on studies carried out using molecular dynamics (MD) simulations to investigate the physics and chemistry of POPC lipid bilayer membranes and their interactions with ions and nanoparticles. In this study two techniques were employed; all atomic (AA) and coarse grained (CG) MD simulations. In the first part of our investigations, the elastic properties of a 1-palmitoyl-2-oleoyl-sn-glycero-3-phosphocholine (POPC) membrane with missing leaflets as well as a defect-free membrane were determined. The calculated bulk moduli compare well with the results of other researchers. Most interestingly, we established that the removal of a whole leaflet or half a leaflet does significantly affect the elastic properties. In studying of diffusivity of Na and Cl ions as well as of water molecules across a POPC membrane, we constructed systems to model the flow of ions across a membrane separating two different aqueous solutions. We were able to show that in order to force diffusion across the membrane, it was necessary to introduce an imbalance of positively and negatively charged ions on either side of the membrane. We have been able to confirm that the diffusion process takes place by the creation of a pore in the membrane. The diffusion coefficients of the ions have been determined from the mean square displacements (MSD) of the particles as a function of time. We found that both the Na and Cl ions diffuse rapidly through the pore with diffusion coefficients ten times larger than in water. Also, we observed that although the Na ions are the first to begin the permeation process due to the lower potential barrier it experiences, the Cl ions complete the permeation across the barrier more quickly due to their faster diffusion rates. AAMD simulations were carried out to determine the adsorption sites of neutral and charged gold nanoparticles on the surface of the POPC membrane in order to understand the first step of translocation process. We have found that the adsorption of a neutral gold nanoparticle is more likely than that of a charged nanoparticle. We were also able to demonstrate the partial penetration of a neutral nanoparticle through the surface of the POPC membrane. CGMD was used to study the stability of a carbon nanotube (CNT) inside the POPC lipid bilayer membrane. We found that the CNT was indeed stable inside the POPC membrane suggesting that such nanotubes could be used as a targeted drug delivery.

Acknowledgments

First and foremost, my deepest and greatest acknowledgement is to my supervisor, Dr. Clarence Matthai, for his guidance and never-ending support during my time of study. His help and generosity has been enormous from the very beginning of my PhD and he has kept me on my path to continue my research. I would also like to give my most sincere thank you and acknowledgements to my co-supervisor, Dr. Emyr MacDonald, for all of his help and personal support during my studies, thanks again for everything you have done for me.

I would like to offer a special thanks to Dr. Jeff Comer, who has helped and guided me throughout my work and assisted me in learning NAMD and VMD programs. He introduced to me these programs in such a way that I found myself constantly engaged with them.

Most of the MD simulations were carried out on the ARCCA computing facilities at Cardiff University without which, this research would not have been possible. I would like to thank Professor Martyn F. Guest, Wayne Lawrence and all other members of ARCCA for their help and guidance during my time at Cardiff.

Many thanks go to Dr. Agostino Migliore for his guidance and help during my study.

Many thanks to the I.T department, both past and present, for you dedication to solving any and all computer issues whenever I had them.

Thanks also go out to the ministry of higher education in the Kurdistan region of Iraq for giving me the permission and fellowship that allowed me to experience this wonderful opportunity. Many thanks to my University of Sulaimani in Kurdistan/Iraq, in particular the department of physics, for letting me take the position.

A big thank you to the Nanoscale Science and Technology research group at the school of physics and astronomy in Cardiff University, Dr Martin Elliot, Dr Andriy Mosalenko and all the members of the department both past and present.

I would also like to thank my colleagues and friends; Athraa Zaki, Isam Abdullah, Adam Beachey, Suzanne Thomas, Dunia Giliyana, Atheel Jameel and Watheq Elias. Each of you made me laugh whenever the lights were off and brought me up when I was down.

A special thanks go to my long suffering, lovely, supportive, best friend, and caring husband, Rebeen. You have always been there for me and always been there for our beautiful children throughout the four long years of my PhD. Every single day, I love you more and more, and I will never forget all the help you have given. I would never have

come this far without your unending support and love. Thank you to my little angels, Lano and Aavel, for being patient with me, my apologies if I could not be there for you as much as I wanted to my loves.
Finally I would like to acknowledge my uncle Ewmed for being a guarantor of my work and encouraging me to pursue this opportunity. Thanks to all the members of my family, especially my mum, and all the members of my family in law for their love, support and encouragement. I love you all! Last, but not least, a great thanks to all my friends, especially Barham and her family, Rafaet and her family, I hope I have not missed anyone out....

Publications

The following publications have resulted from the work presented in this thesis.

1. Computer simulations of the diffusion of water molecules and ions across POPC lipid bilayer membranes by R Salih and C Matthai.
   Submitted to Journal Chemical Physics.

2. Interaction of charged gold nanoparticle with POPC lipid bilayer membranes by R Salih, J Comer and C Matthai.
   In preparation, to be submitted to Journal Chemical Physics.

3. Coarse grained molecular dynamics simulations of the interaction a carbon nanotube with POPC bilayer membrane, by R Salih and C Matthai.
   In preparation.

Contents

1 Introduction **1**

2 Biomolecules, nanoparticles and their applications **7**

2.1 Proteins . . . 8

2.2 Biomembranes . . . 10

2.2.1 The structure of lipid bilayers . . . 10

2.3 Force fields for modelling water (TIP3P) . . . 13

2.4 Nanoparticles . . . 16

2.4.1 Gold nanoparticles . . . 17

2.4.2 Carbon nanotubes . . . 18

3 Computational methodology **21**

3.1 Computer simulations . . . 21

3.2 Monte Carlo simulations . . . 22

3.2.1 The Metropolis algorithm . . . 23

3.3 Molecular dynamics simulations . . . 25

3.3.1 The classical MD algorithm . . . 26

3.3.2 Verlet algorithm . . . 27

3.3.3 Langevin Dynamics . . . 28

3.3.4 Periodic boundary conditions . . . 29

3.3.5 Neighbour lists . . . 30

3.4 Models for the simulation of molecular systems . . . 31

3.4.1 All-Atom Molecular Dynamics (AAMD) . . . 31

3.4.2 Coarse-Grained molecular Dynamics (CGMD) . . . 32

3.5 Force fields . . . 33
3.5.1 Bonded interactions . . . 34
3.5.2 Non-bonded interactions . . . 36
3.5.3 The total energy . . . 38
3.5.4 CHARMM All-Atom force field . . . 38
3.5.5 Martini Coarse-Grained (CG) force field . . . 40
3.6 Molecular Dynamics with NAMD . . . 41
3.6.1 Using NAMD . . . 42
3.6.2 Data files . . . 43
3.7 Calculation of the Free Energy . . . 44
3.7.1 Adaptive biasing force (ABF) . . . 50
3.8 Steered Molecular Dynamics simulations . . . 51

4 Elastic properties of POPC lipid bilayer 54
4.1 Introduction . . . 54
4.2 Calculations of the elastic constants of POPC lipid bilayers . . . 56
4.2.1 Voigt notation . . . 57
4.2.2 Determination of the elastic constants . . . 58
4.2.3 Modelling the system . . . 61
4.2.4 Computational Methods . . . 63
4.3 Results and discussion . . . 64
4.4 Conclusion . . . 67

5 Computer simulations of the diffusion of water molecules and ions across POPC lipid bilayer membranes 71
5.1 Introduction . . . 71
5.2 Modelling the diffusion across the lipid bilayer membrane . . . 75
5.2.1 Systems . . . 75
5.3 Computational methodology and analysis . . . 77
5.3.1 Molecular dynamics simulations . . . 77
5.3.2 Area per lipid and bilayer thickness . . . 79
5.3.3 Calculation of the diffusion coefficients . . . 80
5.3.4 The electrostatic potential across the membrane . . . 81

5.4 Simulations of single Na^+ and Cl^- ion interactions with a membrane surrounded by water . . . 82
5.5 Simulations of single Na^+ and Cl^- ion interactions with a membrane immersed in an ionic solution . . . 85
5.5.1 APL and BLT . . . 86
5.5.2 Ion diffusion coefficients and their spatial distribution . . . 88
5.6 Diffusion of ions across a POPC lipid bilayer membrane with different fluids on either side . . . 92
5.6.1 Results of simulations of System D . . . 93
5.6.2 Results of simulations of System E . . . 96
5.7 Conclusion . . . 108

6 Interaction of gold nanoparticles with POPC lipid bilayer membranes 110
6.1 Introduction . . . 110
6.1.1 Aim of the study . . . 112
6.1.2 Layout of this chapter . . . 113
6.2 Gold nanoparticle structure . . . 113
6.3 Adsorption of gold nanoparticles on the membrane surface . . . 115
6.3.1 Systems and simulation method . . . 115
6.3.2 Results and discussion . . . 117
6.3.3 Conclusion . . . 120
6.4 Free energy calculations of gold nanoparticles on the membrane surface . . . 125
6.4.1 The ABF method and systems . . . 126
6.4.2 Results and discussions . . . 128
6.4.3 Conclusion . . . 135
6.5 Constant velocity pulling of gold nanoparticles through the lipid bilayer . . . 139
6.5.1 Steered molecular dynamics simulations . . . 139
6.5.2 System and method . . . 139
6.5.3 Analyzing data . . . 141
6.5.4 Results and discussions . . . 141
6.5.5 Conclusion . . . 142

7 Coarse grained molecular dynamics simulations of the interaction a carbon nanotube with a bilayer membrane **146**
7.1 All-atom (AA) and coarse-grained (CG) simulations of biomolecular systems 146
7.2 Equilibrium structure of the ubiquitin protein molecule 148
7.2.1 Introduction 148
7.2.2 Simulations 150
7.3 Results and discussions 152
7.4 Simulation studies of the interaction of a POPC lipid membrane bilayer with a carbon nanotube (CNT) 156
7.4.1 Introduction 156
7.4.2 System and computational method 158
7.4.3 Results and discussion 160
7.5 Conclusion 166

8 Conclusion **167**
8.1 Future plans 170

List of Figures

1.1 Schematic image of the cell membrane. 2

2.1 Structure illustration of a protein from primary to quaternary structures . . 9
2.2 Schematic illustration of a membrane cell showing the membrane. 11
2.3 The POPC cell membranes are arranged so that it has hydrophilic heads and hydrophobic tails. 12
2.4 The structual formula of the POPC phospholipid molecule 12
2.5 Schematic diagram of a POPC lipid bilayer. 12
2.6 Permeation of lipid bilayer by important molecules 14
2.7 Different interaction sites of different models. 15
2.8 Solution of gold nanoparticles of different sizes (submicrometre-size). . . . 18
2.9 Models of CNTs exhibiting different chiralities arrangement 19
2.10 Schematic of a two-dimensional graphene sheet illustrating lattice vectors a_1 and a_2, and the chiral vector 19

3.1 A flow chart representing the Metropolis Monte Carlo algorithm to simulate a polymer. 24
3.2 A schematic of periodic boundary conditions in two dimensions. 30
3.3 The difference between All-Atom and Coarse-Grained models in lipid bilayer molecule for example. 33
3.4 Bonded versus non-bonded interactions. 34
3.5 Internal coordinates for bonded interactions: r governs bond stretching; θ represents the bond angle term; ϕ gives the dihedral angle; the small out-of-plane angle α is governed by the so-called "improper" dihedral angle φ. 36

3.6 The variation of Lennard-Jones potential energy as a function of separation distance between the two carbon atoms. 37
3.7 Charge models for N-methylacetamide for two of the CHARMM force field parameterizations. In CHARMM19, the methyl groups are treated as united atoms, so that there is no breakdown into separate C and H charges.. 39
3.8 Mapping between the chemical structure and the coarse-grained model . . . 41
3.9 Flowchart specifies the role of files as used by NAMD, VMD and Psfgen. . 43
3.10 A section from a typical PDB file. 44
3.11 A section from a typical PSF file. 44
3.12 A typical CHARMM parameter file which embraces the parameters for the different force-filed components. 45
3.13 A typical configuration file which embraces set up of the MD simulations in this case the gold nanoparticle placed at the top of the lipid bilayer. . . 46
3.14 Continue of the previous figure. 47
3.15 Pulling in a one-dimensional case. The dummy atom is colored red, and the SMD atom blue. As the dummy atom moves at constant velocity the SMD atom experiences a force that depends linearly on the distance between both atoms. This picture is taken from 52

4.1 The lipids bilayer POPC in water. 62
4.2 The lipid bilayer POPC with one upper leaflet removed. The water molecules have not been shown to give a better view of the lipid bilayer. 62
4.3 The lipids bilayer POPC after removing one whole leaflet (upper and lower). The water molecules have not been shown to give a better view of the lipid bilayer. 63
4.4 An example of the POPC leaflet without (blue) and with (red) applying strain to the z-axis. 65
4.5 The strain-energy ($\Delta E = E - E_o$) as a function of applied strain at 300 K for system 1. The red dots are the data and the green line is a fitting parameter. 68

4.6 The strain-energy ($\Delta E = E - E_o$) as a function of applied strain at 300 K for system 1. The red dots are the data and the green line is the fitting parameter. 69

5.1 Cell structure showing the cellular membrane enclosing the cytoplasm. The extracellular fluid is on the outside of the membrane. 76
5.2 Configurations used to model a lipid bilayer membrane between two fluids. The lipids forming the membrane, shown as chain molecules, are surrounded by water molecules (red), Na ions (yellow) and Cl ions (cyan). 77
5.3 Representation of MSD for Na ion in System A at different regions in the simulation box. 83
5.4 Figure showing the MSD for Cl ion in System A at different regions in the simulation box. 85
5.5 Typical trajectories (in green) over 2 ns of Na (left) and Cl (right) ions in simulation System A. 86
5.6 The simulation cell with a single POPC lipid bilayer surrounded by water containing Na^+ and Cl^- ions with (left) equal concentration and with (right) different concentration. 87
5.7 Typical trajectories (in green) over 10 ns of Na (a) and Cl (b) ions in simulation System B. 88
5.8 Time averaged over 50 ns density distribution of Na (red lines) and Cl (green lines) ions in simulation systems B (top) and C (bottom). The bilayer regions are indicated by the shaded areas. 91
5.9 The net charge distribution on the lipid bilayer. The red areas are regions of negative net charge while blue is of net positive charge. Also shown are the positions of the Na and Cl ions. 92
5.10 Figure showing the ion distribution in System D after 50 ns together with the two POPC lipid bilayers. The water molecules are not shown in order to highlight the positions of the Na (yellow) and Cl (blue) ions. 95
5.11 Typical MSD plots over the last 10 ns of the simulation Na (a) and for Cl (b) ions in System D 96

5.12 Typical trajectories (in green) for Na and (in blue) for Cl over last 10 ns in simulation System D. 97
5.13 The time averaged over 50 ns number density of both ions as a function of z-axis for System D. The bilayer regions are indicated by the shaded areas. 98
5.14 Figure showing the water molecules and ion distribution in System E at different times of the diffusion process. Here, the Na ions are coloured yellow and the Cl ions cyan. The atoms comprising the two POPC lipid bilayers are not shown in order to highlight the opening up of the pore. . 99
5.15 Top view of the membrane showing the pore that allows for the passage of ions through the membrane. 100
5.16 The ion distribution for System E at the end of the simulation run. The Na ions are coloured yellow, the Cl ions are cyan while the phosphorous atoms which mark the lipid bilayer surface edges are colored tan. The approximately equal numbers of Na and Cl ions in both fluid regions show that near equilibrium has been established. 100
5.17 The electrostatic potential plotted across the simulation cell at different times, t for System E. Note that soon after diffusion commences, there is a sharp drop in the electrochemical potential. This is reflected in the voltage scales on the vertical axis 101
5.18 Electrostatic potential map ($x - z$ plot) across the two lipid bilayers at different times, t for System E. 102
5.19 Electrostatic potential profiles at different times, t, as a function of distance across the two bilayers for System E. The bilayer edges are at approximately -7 Å, 30 Å, 88 Å and 126 Å. The different colors denote different coordinates (x,y) on the bilayer surface. 103
5.20 Figure showing density distribution of Na (red) and Cl (green) ions in System E at different times of the diffusion process. The bilayer regions are indicated by the shaded areas. 105
5.21 Typical trajectories (in green) for Na ions, (in blue) for Cl ions, and (in red) for water molecules over 0.62 ns in simulation System E. 106
5.22 Showing the MSD for ions and water molecules in System E of the diffusion process inside the pore. 107

5.23 Showing the reduction in the ion numbers for both Na and Cl in each of the fluid regions I and II respectively, as a function of time. The difference between the two at the end of the simulation points to the cessation of ion diffusion when the electrochemical potential is small. 108

6.1 The structure of a neutral gold nanoparticle with a diameter of 2.2 nm. . . 113
6.2 The structure of charged a gold nanoparticle with diameter of 2.2 nm. The red gold atoms on the surface of the nanoparticle are charged, while the atoms inside the nanoparticle are neutral. 114
6.3 A lipid bilayer membrane with a gold nanoparticle all solvated in a box of water: (a) Side view; (b) Top view. 115
6.4 Figure showing two samples of the system only the phosphorous atoms of the bilayer surface and AuNP are shown. 118
6.5 The BLT of the POPC bilayer membrane for the three types of AuNP. . . 119
6.6 The APL of the POPC bilayer membrane for the three types of AuNP. . . 120
6.7 Figures showing the distance between the center of mass of the POPC bilayer membrane and AuNPs 121
6.8 The neutral charged gold nanoparticle with headgroups of lipids (P) after 50 ns at 300 K, (nanoparticle placed at site C). 122
6.9 The positive gold nanoparticle with headgroups of lipids (P) after 50 ns at 300 k, (nanoparticle placed at site C). 122
6.10 The negative charged gold nanoparticle with headgroups of lipids (P) after 50 ns at 300 K, (nanoparticle placed at site C). 122
6.11 The neutral charged gold nanoparticle with headgroups of lipids (P) after 50 ns at 400 K,(nanoparticle placed at site C). 123
6.12 The positive charged gold nanoparticle with headgroups of lipids (P) after 50 ns at 400 k, (nanoparticle placed at site C). 123
6.13 The negative charged gold nanoparticle with headgroups of lipids (P) after 50 ns at 400 K, (nanoparticle placed at site C). 123
6.14 The neutral charged gold nanoparticle with headgroups of lipids (P) after 50 ns at 300 K (nanoparticle placed at site X). 124
6.15 The positive gold nanoparticle with headgroups of lipids (P and N) after 50 ns at 300 K (nanoparticle placed at site X). 124

6.16 The negative charged gold nanoparticle with headgroups of lipids (P) after 50 ns at 300 K (nanoparticle placed at site X). . . . 124
6.17 Calculated free energy as a function of reaction coordinate ξ for the neutral gold nanoparticle. . . . 128
6.18 Calculated free energy as a function of reaction coordinate ξ for the positive gold nanoparticle. . . . 129
6.19 Calculated free energy as a function of reaction coordinate ξ for the negative gold nanoparticle. . . . 129
6.20 Number of force samples gathered by the ABF algorithm in a total of 360 ns (all windows) as a function of reaction coordinate ξ for the neutral gold nanoparticle. . . . 130
6.21 Number of force samples gathered by the ABF algorithm in a total of 542 ns (all windows) as a function of reaction coordinate ξ for the positive gold nanoparticle. . . . 131
6.22 Number of force samples gathered by the ABF algorithm in a total of 340 ns (all windows) as a function of reaction coordinate ξ for the negative gold nanoparticle. . . . 131
6.23 A typical trajectory for all frames from 0 to 2000 every 3 frames of the neutral gold nanoparticle on the lipid bilayer surface. . . . 132
6.24 A typical trajectory for all frames from 0 to 2000 every 3 frames of the positive gold nanoparticle on the lipid bilayer surface. . . . 133
6.25 A typical trajectory for all frames from 0 to 2000 every 3 frames of the negative gold nanoparticle on the lipid bilayer surface. . . . 134
6.26 Comparison of calculated free energy between the first and the second halves of the trajectories for the neutral AuNP. Also shown is the free energy obtained when combining both halves. The error bars indicate the uncertainty in the results. . . . 135
6.27 Comparison of calculated free energy between the first and the second halves of the trajectories for the positive AuNP. Also shown is the free energy obtained when combining both halves. The error bars indicate the uncertainty in the results. . . . 136

6.28 Comparison of calculated free energy between the first and the second halves of the trajectories for the negative AuNP. Also shown is the free energy obtained when combining both halves. The error bars indicate the uncertainty in the results. . . . 136
6.29 Area per lipid for the system with neutral gold nanoparticle. . . . 137
6.30 Area per lipid for the system with positive gold nanoparticle. . . . 137
6.31 Area per lipid for the system with negative gold nanoparticle. . . . 138
6.32 Trajectory of the neutral gold nanoparticle on the lipid bilayer surface which shows partial penetration of the AuNP by the lipid bilayer surface at 60 ns. . . . 138
6.33 The trajectory of the AuNP after 20 ns at each constant velocity. . . . 143
6.34 The velocity profile as a function z-coordinate when the constant velocity is 0.044 Å/ps. . . . 143
6.35 The velocity profile as a function z-coordinate when the constant velocity is 0.0044 Å/ps. . . . 144
6.36 The velocity profile as a function z-coordinate when the constant velocity is 0.00044 Å/ps. . . . 144
6.37 The force profile as a function z-coordinate for the different applied velocities. 145

7.1 Modelling and simulation methods with associated time and length scales. 148
7.2 A structural view of UBQ using VMD. . . . 149
7.3 The structures of the UBQ protein in the systems of : a) AA b) CG simulations. . . . 151
7.4 CPU time as function of number of steps in AAMD simulation for UBQ on single machine. . . . 152
7.5 CPU time as function of number of steps in CGMD simulation for UBQ on single machine. . . . 152
7.6 CPU time as function of number of nodes in both AAMD and CGMD simulation for UBQ on Raven cluster. . . . 153
7.7 The RMSD of UBQ protein as a function of time in the: a) AA b) CG simulations. . . . 154
7.8 RMSF of protein and backbone with respect to the average coordinates of both simulations. . . . 155

7.9 Structure UBQ from NMR and reverse back from CG simulation. 156
7.10 Martini lipid layout. 159
7.11 The schematic structure of CG carbon nanotube 4:1 mapping: a) the blue circles represent 4 atoms per bead as assigned by red circles b) VDW viewing. 160
7.12 A system representation of the CG lipid membrane with CG carbon nanotube all solvated in CG water: (a) top view without water; (b) side view all the system. 161
7.13 Temperature of the system of CNT with POPC during 300 ns of simulation. 162
7.14 Visualization of the CG membrane (POPC) and the CG carbon nanotube (CNT) during different times of MD simulation: (a) 5 ns; (b) 25 ns; (c) 50 ns; (d) 200 ns; and (e) 300 ns. Picture created using VMD. 163
7.15 The thickness of the POPC lipid bilayer during simulations. 164
7.16 The RMSD value of the CNT at 300 K during 300 ns evolution time. . . . 164
7.17 The RMSD value of the POPC at 300 K during 300 ns evolution time. . . 164
7.18 The RMSF of the CNT atoms at 300 K during 300 ns evolution time. . . . 165
7.19 The force of the lipids on the nanotube at three axis during 300 ns evolution time. 165
7.20 The tilt angle between carbon nanotube and the normal axis lipid membrane (z) during 300 ns evolution time. 166

List of Tables

4.1 Anisotropic elastic constants of POPC lipid bilayer membrane in units of GPa. . . . 65
4.2 A comparison of the calculated and experimentally determined bulk and shear moduli of a POPC lipid bilayer membrane in units of GPa. . . . 67

5.1 Details of systems investigated by molecular dynamics . . . 78
5.2 Lennard Jones parameters for the ions in CHARMM36 and used in this study. . . . 79
5.3 Diffusion coefficients, D ($\times 10^{-5}$ cm^2/s), of Na^+ and Cl^- ions at different positions in the simulation box for System A. Also shown is the diffusion coefficient for a water molecule. . . . 84
5.4 Diffusion coefficients, D ($\times 10^{-5}$ cm^2/s), of Na^+ and Cl^- ions at different times for system B and C. . . . 90
5.5 Diffusion coefficients, D ($\times 10^{-5}$ cm^2/s), of Na^+ and Cl^- ions averaged for System D. . . . 94
5.6 Diffusion coefficients, D ($\times 10^{-5}$ cm^2/s), of H_2O molecules, Na^+ and Cl^- ions at different times during their passage through the pore. . . . 104

6.1 Systems details . . . 117
6.2 Results . . . 118
6.3 Windows given for the free energy calculations . . . 127
6.4 The velocities given to the neutral AuNP . . . 140
6.5 Results of the APL and BLT . . . 142

7.1 Simulation details . . . 151

7.2 Residue numbers for AAMD and CGMD systems of the UBQ. 155

To Rebeen, Mum, Lano, Avel,

and family....

Chapter 1

Introduction

In recent years there has been much progress in the application of techniques from quantum chemistry and physical modelling to studying biological systems. Thus electronic structure calculations based on Hartree-Fock theory and density-functional-theory (DFT) have been used to give information about the structure of amino-acids and proteins as well as helping in the understanding of protein and DNA folding. In addition, physical theories based on statistical mechanics and phase transitions have a role to play in furthering our understanding of the energy and structural aspects of large biomolecules.

However, the complexity of these types of calculations has meant that in the simulations of proteins and large biological molecules, with a view to learning about their structure in the condensed or globular phase, it is necessary to resort to empirical methods to provide much of the answers to these questions. Therefore, a calculation or simulation is only as good as the models utilised in describing these complicated systems. For this reason, many years of effort have been given to the construction of force field models which are transferable robust and particularly adapted for biological systems [1, 2].

In this thesis, we report on work carried out to examine how ions, atoms, molecules and nanoparticles interact the with the bilipid membrane of a living cell. As shown in Figure 1.1, a cell has a membrane which defines the shape and extent of the cell. All

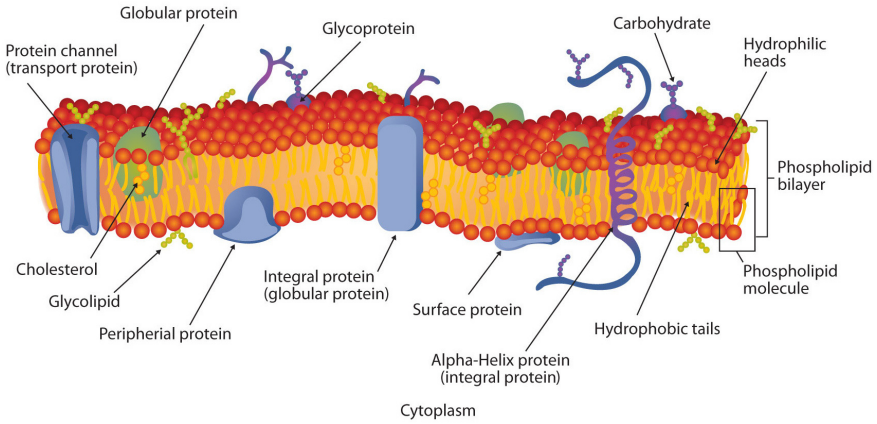

Figure 1.1: Schematic image of the cell membrane.

particles entering and leaving the cell has to pass through this membrane. The way by which these particles can pass through the membrane can be either through pores in the membrane itself or by the creation of pores by the presence of electrical or chemical gradients across the membrane. Our investigations have focussed on the latter method.

In carrying out this work, it is important that the actual membrane is well described by the interatomic forces and in particular the response of the membrane to external forces must be accurate. In empirical modelling, this is usually done by ensuring that the elastic response of the membrane to external forces is realistic. So the first sets of simulations were focussed on ensuring that the elastic constants and compressibility were well reproduced for the force fields in question. Once this was established, the molecular dynamics methods were applied to studying how particles interacted with the membrane.

The interest in ion permeation across lipid cellular membranes has been around for a long time. This is no doubt due to the importance of hydration of biological cells and the need for their proper functioning. This in turn depends on how the membrane interacts with water molecules and with other small molecules dissolved in water. Many of the studies have examined the different possible processes by which ions can diffuse through a membrane. Therefore, realistic molecular dynamics simulations allow for the possibility of

not only extracting the mechanisms and pathways for ion diffusion but also for accurately assessing how the diffusion constants of these ions, atoms or molecules depend on factors like the temperature, the electric field gradient and so on. Our investigations into studying this process form one of the major themes of this thesis.

Nanoparticles are materials with dimensions less than 100 nm. This feature means that nanoparticles are novel materials. In addition to that, they have high electrical and thermal conductivity, high tensile strength and can be used in many industrial applications such as in bioscience and nanomedicine [3]. In recent years, the interaction of nanoparticles with cellular membranes have provoked much interest.

Gold nanoparticles have been proposed as having the potential to be used in a whole range of clinical applications because of their unique atomic and chemical properties. Thus, for example, gold nanoparticles can be used in therapeutics by targetting them on to specific tissues. The size of these particles also allows them to be used as drug carriers. In particular, conjugating oligonucleotides, pharmaceuticals or proteins on the gold nanoparticle surfaces allows them to be used as agents for pharmaceutical delivery. Thus it is of much interest to examine how functionalization of these nanoparticles can help penetrate cellular membranes. In order to improve understanding of the interaction of gold nanoparticles with a lipid bilayer membrane, experimental and compuational investigations have focussed on different types of nanoparticle structures. Also, using different types of nanoparticles is to manipulate and control the ability of circulation in order to take advantage of using them in delivering drugs, genes and so on. A better understanding of the interaction between the nanoparticle with pentapeptides may results in providing new tools in the design of new engineering materials for biomedical applications [4].

It is well recognised that nanoparticles in general can have a detrimental effect on living bodies exposed to them. The cytotoxicity can depend on the shape and size of the nanoparticles. One of the ways by which these nanoparticles can enter in the cell is by diffusing through the cell membrane. There have been many studies aimed at investigating

how the hydrophobicity and the charge of the nanoparticle affects the diffusion process.

Thus, for both these types of applications, investigations of the interaction of gold nanoparticles with the membrane surface and of the translocation of these nanoparticles across a cellular membrane is of paramount importance. In our investigations, we have therefore considered the interaction of gold nanoparticles with bilipid membranes including the conditions which allow for membrane penetration by these nanoparticles.

In many simulation studies of biological materials and molecules, it is often found that the size and time-scales required are beyond the scope of computation facilities. As a result a host of techniques and methods have been proposed and tested as to their efficacy. Coarse-grained models have the advantage of being used in molecular dynamics simulations without the need to consider every individual atom. This allows for greater speed in the computations and as a result may be applied to systems previously inaccessible. However, it is important that the results obtained from these coarse grained models are correct and reproducible. In this thesis, we report on work carried out on the interaction of carbon nanotubes with cellular membranes and demonstrate the usefulness of this approach in such studies.

A short summary of each chapter in this thesis is given below.

Chapter 2: In this chapter an introduction to biomolecules such as proteins and lipid bilayer membrane, force filed for modelling water (TIP3P), and description of nanoparticles with examples of gold nanoparticle and carbon nanotube are given.

Chapter 3: This chapter provides a description of computational methodology used in this thesis. An introduction to molecular simulations methods such as Monte Carlo (MC) and molecular dynamics (MD) simulations with their algorithms are given. Then, models for simulations of molecular systems such as All-Atom (AA) and coarse-grained (CG) molecular dynamics (MD) are explained. Typical examples of force fields such as CHARMM All-Atom and Martini coarse-grained model, which they were used in this thesis, are given. The equations used for calculating the bonded and non-bonded inter-

actions between the atoms are also included. Then, a particular package of molecular simulations, namely the NAMD package is explained together with a discussion of how to prepare the input files. Finally, free energy calculations using the adaptive biasing force (ABF) method and steered molecular dynamics (SMD) are also presented.

Chapter 4: This chapter provides the results of MD simulations of the palmitoyloleoylphosphatidylcholine (POPC) lipid bilayer membrane using the (AA) method to determine the elastic properties of POPC bilayer membrane. Methods for calculating elastic constants with modeling systems are discussed. Then, the results of our simulations are compared with available experimental data.

Chapter 5: Based on the techniques used in the previous chapter, the results of computer simulations of the diffusion of water molecules and ions across POPC lipid bilayer membranes are given in this chapter. Extensive (AA) MD simulations with different systems of ions in POPC lipid bilayer (one lipid bilayer and two lipid bilayer on the top each other) are provided. Results for the diffusion coefficient for different ions and water molecules inside and around the bilayer are reported with and without the presence of an electrostatic potential. A novel part of this study was a detailed study of the variation of the the diffusion coefficients as a function of time. Also, the results of a study of the electrostatic potential across the lipid bilayer are given and found to be in qualitative agreement with the work of other researchers and experimental data.

Chapter 6: In this chapter the adsorption of gold nanoparticles on a membrane surface was investigated in order to gain an understanding of the first step in the translocation process of the permeation of a nanoparticle across a membrane. Differently charged gold nanoparticles placed on a POPC bilayer surfece were studied and the simulations carried out using different random starting positions of the gold nanoparticles. The simulations were also carried out at different temperatures. Then, the determination of the adsorption energy of the nanoparticles was carried out by calculating the potential mean force in order to estimate the free energy using the (ABF) method. Finally, the results

of a SMD study are reported in which different constant velocities were applied to gold nanoparticles in order to find the minimum force required to cross the POPC bilayer.

Chapter 7: The results of CG MD simulations of carbon nanotubes within a bilayer membrane are reported in this chapter. A comparison of the results of AA and CG MD simulations for the simple ubiquitin protein molecule are first given to show that the results are consistent with each other. Based on this, the CG model was applied to describe a carbon nanotube inside a POPC lipid bilayer. This was done to demonstrate the usefulness and efficacy of the CGMD method for such simulations.

Chapter 8: Finally, all the results of reported in this thesis are brought together as a summary of the thesis. This includes a critical assessment of the our results which are also compared with the results with other investigations.

Chapter 2

Biomolecules, nanoparticles and their applications

Macromolecules such as proteins and lipid bilayer membranes have an important role in biological processes such as gas transport, enzymatic catalyzing reactions, the building block of living cells and so on. Complex tiny cells complete all the activities needed to ensure the proper working of living organisms. They also perform the actions that control the flow of ions and molecules across the cell membranes. It is interesting that the biomolecules and their metabolism have been the subject of comprehensive and, in many respects, successful biochemical and medical research for a long time. The view has also been advanced by scientists that macromolecules have the ability to transport foreign objects such as nanoparticles into the cells. This has advantages in nanotechnological applications such as agent therapy and nanoinjectors because of their small sizes and their ability to enter cells. This chapter gives an overview of the background of biomolecules such as proteins and the lipid bilayer membrane. A description of the model of water, which has been used in this thesis, will be given as well. In addition, a short section describing nanoparticles such as gold and carbon nanotube are given in this chapter.

2.1 Proteins

Proteins in biological cells are essentially heteropolymers consisting of different types of beads. Each bead has a different shape and comprises smaller particles called amino acids of which there are a standard number of 20 types [5]. The amino acids are connected to each other by a peptide backbone and so make a polypeptide chain with different side-chains comprising different amino acids. Each amino acid side-chain has a different size, shape, charge, and property. They can also be classified into hydrophobic and hydrophilic parts. Some side-chains of hydrophobic amino-acids have only carbon and hydrogen atoms and are called aliphatic side-chains. Side-chains of hydrophilic amino acids can be ionized or can be polar. The hydrophobicity of an amino-acid means that these molecules avoid interactions with the surrounding water and prefer to interact with other hydrophobic molecules.

In general, proteins can be classified into two types; globular and fibrous. Globular proteins are compact, with spherical shapes and are soluble. By contrast, fibrous proteins are insoluble and typically have extended shapes.

Proteins are complex structures with configurations that are formed at different levels. The way in which the linear sequence of amino acids is constructed leads to the primary structure of the protein. This is then followed by the secondary structure which is made up from combining hydrogen bonds between amino acids. Two particularly stable structural elements thus formed are the alpha helices and the beta sheets. The arrangement of alpha helices and beta sheets together with other molecules results in the formation of the three dimensional protein structure called the tertiary structure. Its stabilization is due to hydrogen bonds, salt bridge and van der Waals interactions. Finally, the connection of two or more amino acid (folded polypeptide) chains or a complex of multiple proteins forms the quaternary structure. Examples of the different levels of the protein structure hierarchy are shown in Figure 2.1. In complex biological organisms, there are different types of proteins each with its own activity inside cells.

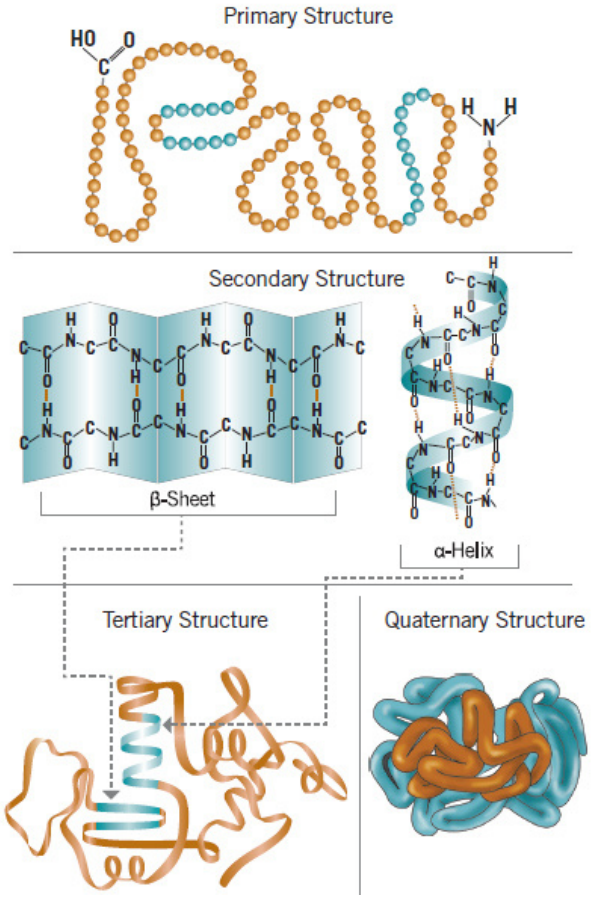

Figure 2.1: Structure illustration of a protein from primary to quaternary structures [6].

2.2 Biomembranes

Biological membranes enclose cells, thus allowing for the separation between the inside and outside of an organism. They are thus fundamental building blocks that influence the structure and functions of biological entities. An example of a membrane is shown in Figure 2.2. They do not just simply provide a covering for cells, but they also perform more important functions that are essential to all cells. Every cell is covered by a membrane which gives structure to the cell and allows for the passage of nutrients and waste into and out of the cell. The principal function of the biological membrane is to separate the cell contents from the outside environment. So membranes must be able to maintain huge differences in chemical composition between the cell and its surroundings. Moreover, membranes need to allow for the flow of information between all the components of cells with the outside. Finally, while membranes must be mechanically stable enough to withstand a hostile environment, the function and growth of cells is intimately tied to their shape. Thus, membranes must be sufficiently malleable to allow cell growth, cell division, and dynamic changes of cell shape. All of this has to be achieved in a reproducible manner. Thus, membranes must be able to reconcile a dazzling array of partly contradictory demands. More information about the biological cell membranes can be found in the literature [5, 7, 8].

2.2.1 The structure of lipid bilayers

Lipid bilayers are general components of all cell membranes and mainly consist of phospholipids, glucolipids and sterols. All of these lipid molecules have a hydrophilic "polar" head and the hydrophobic "non-polar" tail region and comprise carbon C, hydrogen H, oxygen O, phosphate P, and nitrogen N atoms, as shown in Figures 2.3 and 2.4. In general the lipids are fats which means they are insoluble in water. One of the significant properties of lipids is their ability to dissolve in organic solvents, such as benzene. They

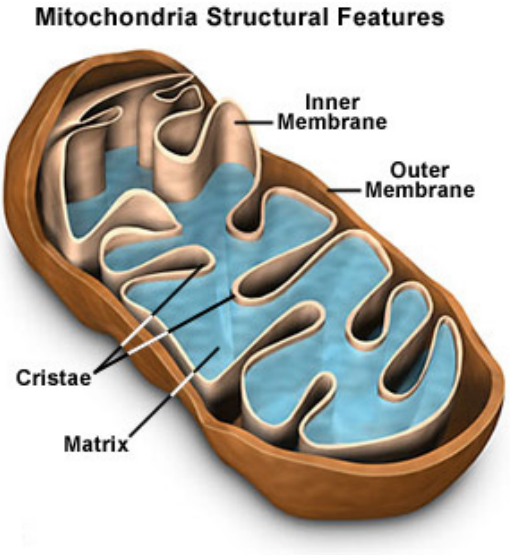

Figure 2.2: Schematic illustration of a membrane cell showing the membrane.

have a typical thickness of 0.5 nm and can be observed by electron microscopy.

The lipid bilayers (referred to as leaflets) consist of two hydrocarbon chains that are connected to the polar headgroups. Figure 2.4 shows structural formula of POPC which is one type of lipid bilayer membrane. Like all lipid bilayers, the POPC bilayer comprises of 2 leaflets, each in turn made up of a number of phospholipid molecules. The phospholipid molecule has a hydrophilic headgroup and a hydophobic tail group (Figure 2.5). Because of this, the heads of the molecule prefers to be in an aqueous environment while the tails are more stable in a lipid environment. This then leads to the natural formation of bilayers in which the headgroups point outwards into the water while the tailgroups point towards each other.

This bilayer arrangement leads to the spontaneous formation of liposomes in an aqueous environment. Liposomes are spherical structures with the boundary layer formed of lipid bilayers and with water outside as well as inside the boundary.

Phospholipids and membrane proteins can diffuse laterally across the membrane. Membrane proteins perform many important functions including allowing for the trans-

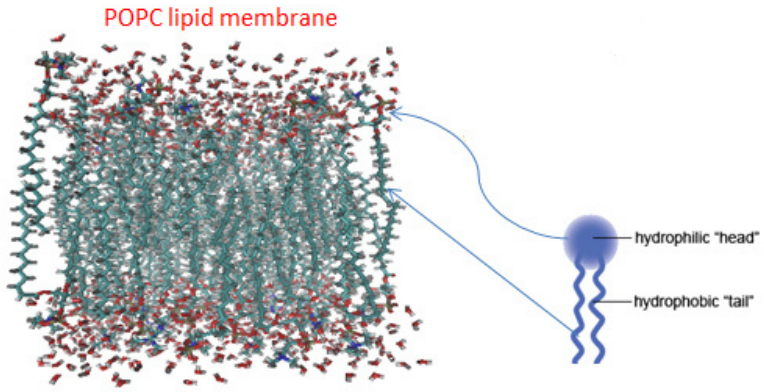

Figure 2.3: The POPC cell membranes are arranged so that it has hydrophilic heads and hydrophobic tails.

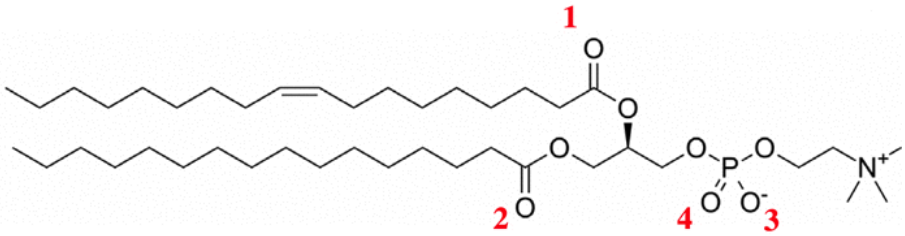

Figure 2.4: The structual formula of the POPC phospholipid molecule [9].

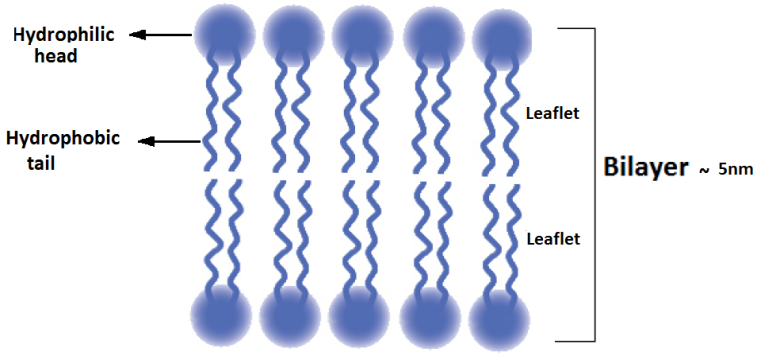

Figure 2.5: Schematic diagram of a POPC lipid bilayer.

mission of messages and the transport of molecules into and out of the cells. Without these, the membrane can be an impenetrable barrier. The membrane proteins can have different structures and functions and can also act as pores for the transmission of molecules [10, 11].

Thus lipid bilayers have unique properties including anisotropic internal dynamics, impermeability to water or non-organic solutions, and allows lipid molecules and proteins to diffuse laterally into two dimensions. Because of their interior hydrophobicity, the bilayers serve as a barriers or gates to the passage of most polar molecules, large biological molecules, and hydrophilic molecules through the membrane as shown in the Figure 2.6 [12]. Ions and large molecules are forbidden to pass through the lipid bilayers even through passive diffusion [12], unless through an ion or protein channel which do allow transportation of biopolymers through channels [10, 11]. However, different electrical potentials across a lipid bilayer can allow for charged particles, such as ions, to permeate and pass through the lipid bilayer. This is very useful in biomedical applications for example, where this property can be used to allow for the passage of drugs through the cell membrane. In general, understanding the structure and other physical properties such as the dynamic properties of lipid bilayers is an important precursor to the study of ion diffusion across bilipid membranes.

2.3 Force fields for modelling water (TIP3P)

Water has been the subject of computational modelling for many years. Any modelling of water needs to consider three important points. These are the atomic sites, which explain the number of interaction points, the flexibility of the model - whether it is rigid or flexible, and finally the polarization effects. The main issues associated with modelling water is thus in obtaining a good representation of the hydrogen bonding potentials and by correctly describing the polarization of the hydrogen and oxygen atoms. The different

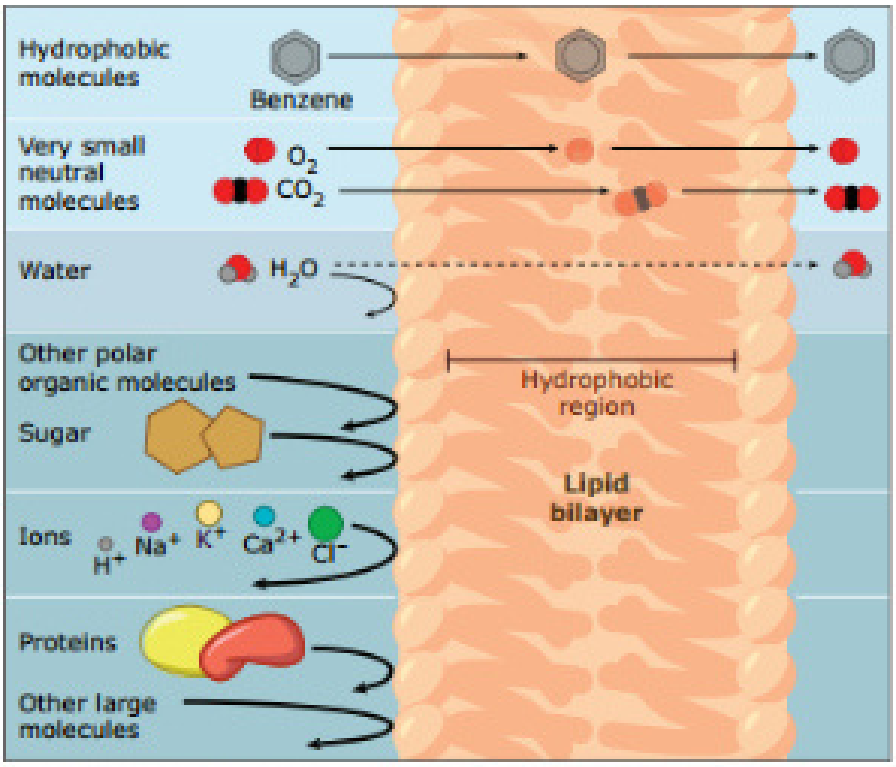

Figure 2.6: Permeation of lipid bilayer by important molecules [12].

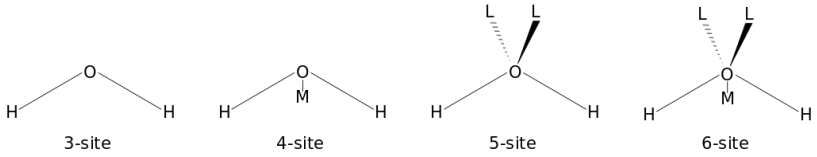

Figure 2.7: Different interaction sites of different models.

models that have been constructed are usually characterised by their interactions sites. Of these, the most commonly used are the: SPC (simple point charge); SPC/E (extended simple point charge); TIP4P (transferable intermolecular potential 4P); TIP3P (transferable intermolecular potential 3P) models. These use between three to six interaction sites as shown in the Figure 2.7. There are other models which have also been employed and references to these can be found in Wallqvist et al [13].

The biomolecular simulations carried out in this thesis cannot be done without the membranes being immersed in an aqueous solution. Essentially, a minimum of between 100 and 1000 water molecules need to be introduced for simple molecular simulations. However, in simulating larger systems, it is necessary to introduce more than 10,000 water molecules. The potential energy functions used in modelling water are based on the Hamiltonian chosen for the model representation. The parameter values in the energy functions are derived from a combination of sources: experimental results, molecular mechanics and quantum mechanics.

The TIP3P model is the simplest rigid model which also accounts for non-bonded interactions. It uses three interaction sites for the electrostatic interactions. Each site includes a point of charge and the hydrogen atoms have a partial positive charge which is balanced by the negative charge on the oxygen atom. The inter-molecular interactions between two water molecules is calculated using the Lennard-Jones interaction potential centred on just the oxygen atom. This means that there are no van der Waals interactions for hydrogen atoms in TIP3P model. However, the CHARMM force field modified the original TIP3P model in that Lennard-Jones interactions were also taken into account

for the hydrogen atoms. In general, the choice of computational model can result in changes from the exact geometric parameters such as the distance between the hydrogen and oxygen atoms, and the angle between hydrogen atoms and the oxygen atom. In our simulations work, the TIP3P model which is based on the CHARMM36 force field has been used.

2.4 Nanoparticles

Nowadays such small microscopic particles with dimensions between 1 nm to 100 nm have begun to play an important role in scientific and technological applications. It is interesting to note that these nanoparticles are generated naturally in volcanoes or forest fires or can be produced by human beings from anthropological sources. The term nanoparticles sometimes applied to 'ultrafine particles' refers to the nature of the particles which are either man-made or natural. The properties of nanoparticles are different from those particles which have larger scales. This means that their size is significant in determining the properties of materials at nanoscale range. For example, gold nanoparticles are different from bulk gold particles in colour; they are red, orange and sometimes green [14] depending on the size of the particle in contrast to bulk gold particles which are yellow. Similarly, other properties such as the melting point, electrical conductance, and other chemical properties are also different due to the nature of the interactions between the atoms. In general, particles of different sizes can behave differently in quantum mechanical systems. When the particles are very small, quantum mechanics needs to be used to explain the observations whereas classical mechanics can be used to treat larger particles. The materials which make nanoparticles are various such as metal oxide ceramics, silicate, and metals nanoparticles. Materials can also be engineered to have novel properties due to their sizes. These include fabricated quantum dots, nanotubes, and fullerenes.

The fields of applications using nanoparticles are wide in nanotechnology such as com-

puter memories, electronic circuits, cosmetics, solar system, sensors and so on. Apart from nanotechnology, nanoparticles can also prove to be more powerful in microelectromechnical field systems. Such systems used in biomedical applications of drug delivery, bloodstream, and tissue repairing. In this thesis, the term nanoparticles has been used to define particles of nanometre scale that interact with the biological lipid bilayer membrane. In this thesis, we have focused on two such particles; gold nanoparticles and carbon nanotubes and on their interactions with lipid bilayers.

2.4.1 Gold nanoparticles

Gold nanoparticles (AuNP) are among the most important particles in many areas of research. As discussed above, differences in sizes can cause the colors of the particles to be different as shown in the Figure 2.8. The role of different sized particles are also important in medical applications. For example, in photothermal cancer therapy [15], uniform sized gold particles are required. The colour differences as a function of size are also significant in the synthesis of gold nanoparticles as these colours are indicators of reduction [16]. The absorption wavelength depends on not just the size but also on the shape of the gold nanoparticles. For example, spherical shaped particles tend to absorb in the NIR region. The charge on the gold nanoparticle can also make a difference as the electrostatic interactions with the cell membrane and can have implications, such as in toxicity. Temperature is another factor that needs to be considered when examining the interaction of gold nanoparticles with biological systems. This is because the lattice cooling rate is a measure of heat distribution to its surroundings [17]. Apart from these uses, gold nanoparticles can be used in treatment of HIV, Hepatities B, and Tuberculosis.

In our investigations, we have been concerned with the interaction of spherically shaped gold nanoparticles with bilipid membranes. We have also investigated the effect of charged gold nanoparticles and how these affect the interactions.

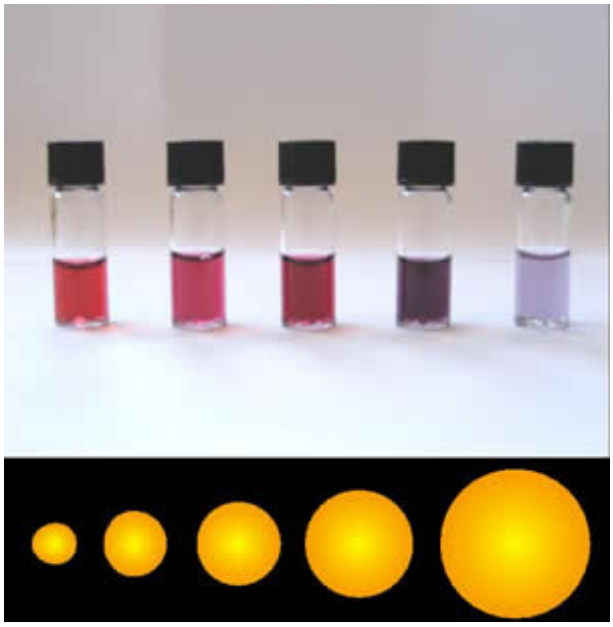

Figure 2.8: Solution of gold nanoparticles of different sizes (submicrometre-size).

2.4.2 Carbon nanotubes

Carbon nanotubes (CNT) are nanoparticles which have cylindrical structures. They are basically graphene sheets rolled into cylinder shapes and comprise of carbon atoms bonded through *s-p* bonding. They have diameters in the range 1 nm to 50 nm. The unique geometries of carbon nanotubes can be classified into three different types. These are also referred to as flavours and are categorized by how the carbon sheets are wrapped to form the tubular structures. The three flavors are the armchair (n, n), zig-zag (n, 0), and chiral (n, m) as shown in the Figure 2.9. In two dimensional graphene (Figure 2.10), the lattice vectors a_1 and a_2 are connects crystallographically equivalent sites on that sheet is called the chiral vector C_h which depends on the integers of m and n.

$$C_h = \hat{n}a_1 + \hat{m}a_2 \tag{2.4.1}$$

Because of CNTs physical properties such as strength and conductivity, many scien-

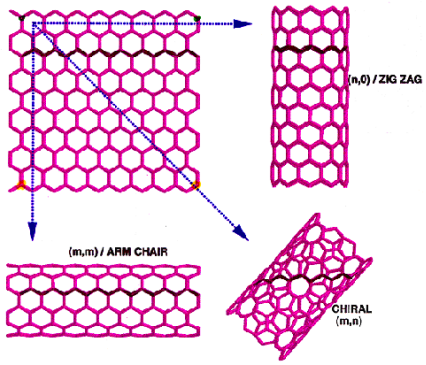

Figure 2.9: Models of CNTs exhibiting different chiralities arrangement [18].

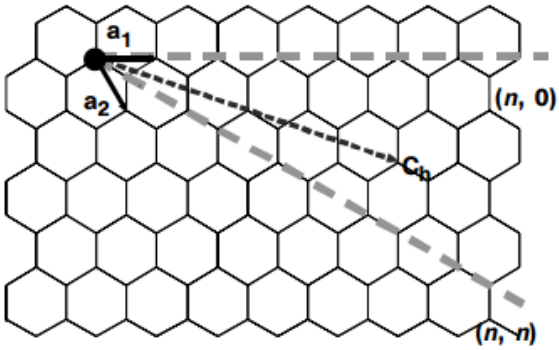

Figure 2.10: Schematic of a two-dimensional graphene sheet illustrating lattice vectors a_1 and a_2, and the chiral vector [19].

tists have investigated their use in building tiny transistors for computer chips and other electronic devices [18]. It has also been suggested that CNTs could have many applications in nanotechnology and medicine. In our studies, we have examined the interactions of CNTs with the bilipid membranes. We have carried out coarse grained simulations with a view to assessing the usefulness of the former in very large scale molecular dynamics studies.

Chapter 3

Computational methodology

3.1 Computer simulations

A computer simulation is a technique by which a system in the real world is represented by a model which is then allowed to evolve in time. By carrying out computer simulations some of the properties of a system may be determined. In other words, a software program is developed so that it tries to simulate some phenomenon based on a scientist's principle and mathematical understanding of the phenomenon. One can test a theory by carrying out simulations using the same model and by varying some of the parameters. This is similar to what is done experimentally in the laboratory.

There are many fields in condensed matter physics have been investigated using computer simulations. It has played a significant role in solving crucial problems in statistical physics, physical chemistry and biophysics. The important advantage of a simulation is the ability to extend the range of the complexity that separates the solvable from the unsolvable. Basic physical theories applicable to biologically important phenomena, such as quantum, classical and statistical mechanics, lead to equations that cannot be solved exactly except for a few special cases. For example, the classical Newton's equations of motion for a system of more than two point masses or the quantum Schrödinger equa-

tion of any atom except hydrogen can only be solved approximately. This is called the many-body problem by physicists and approximate numerical methods need to be used in such investigations. The structure and microscopic interactions between molecules can be calculated from atomistic input using computer simulations to understand their properties. The mechanical and structural properties of condensed matter or molecular systems can be simulated using methods like the Monte Carlo (MC) and/or Molecular Dynamics (MD) simulations.

In the next sections, outlines of both MC and MD methods are described. The work carried out and reported in this thesis was carried out using Molecular Dynamics methods.

3.2 Monte Carlo simulations

The term Monte Carlo simulation is employed to studies that use stochastic methods to make a new structure of a system of significance and is based on the use of random numbers. MC methods have been used to calculate physical properties of matter such as electrical, thermal conductivity, etc. Monte Carlo simulations have also been used in polymer physics to model polymer conformations and other physical properties.

Generally the process of carrying out Monte Carlo simulations of a polymer system can be explained as follows.

A basic Monte Carlo simulation starts with constructing an initial configuration of the polymer. Then, a particle (atom or molecule) comprising the polymer is chosen randomly and given a small displacement. This 'move' is then either accepted or rejected based on how the total energy of the system compares with that before the move has been carried out. If the move is accepted, the new configuration is used as the starting point before the next trial move. However, if it is rejected, the original configuration will used again. This process is carried out repeatedly until the system has been sufficiently sampled. Once this has been done, the potential energy of the system and other physical properties can

be calculated [20].

There are a number of MC schemes that have been used in polymer simulations. Below, the Metropolis scheme for arriving at the minimum energy configurations of polymers is described.

3.2.1 The Metropolis algorithm

As mentioned earlier, there are two different approaches that are used for simulating polymers. These are the Molecular Dynamics (MD) and Monte Carlo (MC) simulations. In these two approaches, all interaction energies between monomers in the system have to be calculated. In order to minimize the energy configuration of polymer both approaches of simulation have been used to simulate polymers in general. The flow chart of this method as applied to polymer simulations is shown in Figure 3.1.

In general this can be done by constructing a polymer chain (N monomers) using a random walk or a self-avoiding walk. The energy of the initial configuration (E_{old}) of the polymer, is determined using the non-bonded Lennard Jones or Morse potentials. Then one or more monomer is chosen randomly and moved by some small random amount. The energy of this new configuration (E_{new}) is calculated. Then the energy difference between these two configurations is

$$\Delta E = E_{new} - E_{old} \tag{3.2.1}$$

In the Metropolis scheme, the new configuration is accepted or rejected with some probability. This can be done by comparing the transition probability (Boltzman probability) with a random number $r \in (0,1)$.

$$r < \exp\left(-\Delta E/\mathrm{K}_B T\right) \tag{3.2.2}$$

where K_B is the Boltzman constant and T is the temperature of the system. Note that the new configuration is accepted, if the new energy is smaller than the old energy or if

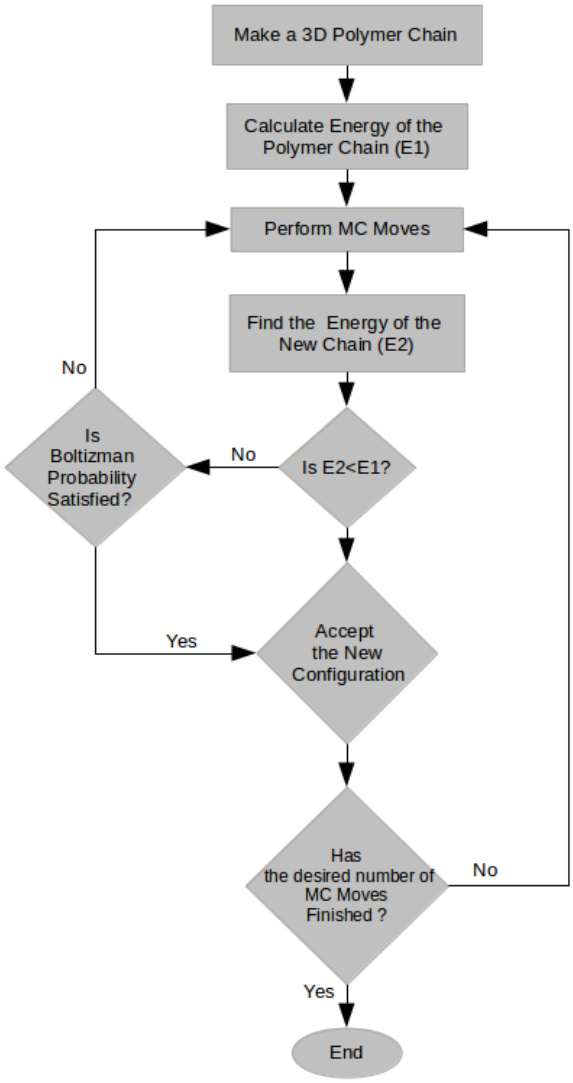

Figure 3.1: A flow chart representing the Metropolis Monte Carlo algorithm to simulate a polymer.

the condition in equation (3.2.2) is met. Otherwise the new configuration will be rejected and a new set of movements will be made and the energy will be recalculated. The process continuous until the system reaches equilibrium [21].

3.3 Molecular dynamics simulations

In order to compute the equilibrium and transport properties of many-particle systems the MD technique has been used. MD simulation is one of the most common methods has been used in the theoretical study of physics, chemical-physics, and biophysics. This technique has produced detailed information on the conformational changes and fluctuation of molecules (polymers) such as proteins and nucleic acids [22]. MD simulations can be classified into two approaches; classical mechanics and quantum MD methods. These can be recognized according to the model chosen to represent a physical system. In the classical MD technique, molecules or atoms are treated as classical objects in which atoms are represented as balls and the bonds as sticks (ball and stick model). In this approach Newton's equation of motion are solved numerically for a set of many particles interacting via pair potentials. From their trajectories, MD is able to determine the positions and velocity of the particles according to time. In the quantum MD approach, the electron density function of a system of many electrons and nuclei are numerically solved from the Schrödinger equation. There are advantages and disadvantages of these two methods explained in [23]. The main advantage of classical MD technique is that it is several orders of magnitude faster than the quantum MD. However, the advantage of the quantum MD approach is that it can be used in providing knowledge on a number of biological problems. Quantum mechanics describe the basic physics of condensed matter. Nevertheless, trying to solve the Schrödinger equation numerically for a system consists of many electrons and nuclei is still premature. Thus quantum MD demands more computational facilities [24].

3.3.1 The classical MD algorithm

In the classical MD scheme, all the particles in a system are given a mass, m_i, and these particles interact with each other through an interatomic potential. Thus, each atom in the system has a position vector, $\mathbf{r}_i$, based on the initial configuration. Then, the force acting on each atom is derived from the sum of the pair potentials involving that particle and is written as

$$\mathbf{F}_i = m_i \ddot{\mathbf{r}}_i \tag{3.3.1}$$

where $\mathbf{F_i}$ is the net vector force acting on i^{th} atom, m_i is the mass of the atom i, and $\ddot{\mathbf{r}}_\mathbf{i}$ is its acceleration. The equations of motion are then integrated numerically using the information of the force acting on each atom to find their positions and velocities after a time step. By carrying out the integration successively, a trajectory that describes how the positions and velocities of the particles vary with time is obtained. In order to ensure that the integration errors are small enough to be ignored, a small enough time must be taken. The MD simulation of a system starts with an initial configuration of the particles making up the system. The particles are then given velocities from a Maxwell-Boltzmann distribution for each coordinate, scaled to the temperature at which simulation is run. The total momentum of the system is made equal to zero by adjusting the velocities of each particle. At each time step, the forces on each particle are determined and the positions of each particle are calculated. This process is carried out repeatedly for a desired number of time steps. So the entire energy of the system is estimated from a composite potential energy which reflects all the diverse interactions in the system.

In general, two types of MD simulations may be carried out. In the first, the aim is to often to determine the equilibrium configuration of the system of interest. If it is to find the minimum energy configuration, the simulation is usually carried out zero kelvin and the simulation continues until the forces on all the atoms is near zero.

When it is of interest to determine the properties of system at some temperature T,

the system is allowed to evolve over a number of steps until the energy fluctuates about some value, with the size of the fluctuations of the order of the k_BT. Then the simulation is continued over more time steps in order that some equilibrium properties - eg, the mean square deviation of atoms, the radius of gyration in polymers, etc - may be determined by time averaging.

3.3.2 Verlet algorithm

There are many algorithms that can be used to integrate the equation of motions in a MD simulation. All these use Taylor expansions to arrive at the approximate positions and velocities from one time step to the next. One of the methods is the so called Verlet algorithm[25, 26], which is simple and easy to compute. In this algorithm, positions of atoms $\mathbf{r}(t)$ and accelerations $\mathbf{a}(t)$ at one time t as well as the positions at the previous time steps $\mathbf{r}(t-\delta t)$ at time $(t-\delta t)$ are necessary to calculate the positions $\mathbf{r}(t+\delta t)$ at the next time step $(t+\delta t)$. Here δt is the time step. By using Taylor expansions for the positions $\mathbf{r}(t)$ leads to the standard Verlet algorithm which can be written as follows.

$$\mathbf{r}(t+\delta t) = \mathbf{r}(t) + \mathbf{v}(t)\delta t + \frac{1}{2}\delta t^2\mathbf{a}(t) + ... \tag{3.3.2}$$

$$\mathbf{r}(t-\delta t) = \mathbf{r}(t) - \mathbf{v}(t)\delta t + \frac{1}{2}\delta t^2\mathbf{a}(t) + ... \tag{3.3.3}$$

Then, adding these two equations obtains

$$\mathbf{r}(t+\delta t) = 2\mathbf{r}(t) - \mathbf{r}(t-\delta t) + \mathbf{a}(t)\delta t^2 \tag{3.3.4}$$

In this Verlet algorithm, it is not necessary to know the velocities directly. However they are required for the calculation of the kinetic energy, which in turn is necessary in testing the conservation of the total energy ($E_{total} = K.E + P.E$) during a simulation. It

is also needed to perform some kind of temperature control. The velocities can be easily approximated from the positions of the atoms using the following equation

$$\mathbf{v}(t) = \frac{\mathbf{r}(t+\delta t) - \mathbf{r}(t-\delta t)}{2\delta t} \tag{3.3.5}$$

Another approximation leads to the so called velocity Verlet algorithm. In this approach, the positions and velocities are computed at each time step through the following formulas

$$\mathbf{r}(t+\delta t) = \mathbf{r}(t) + \mathbf{v}(t)\delta t + (1/2)\mathbf{a}(t)\delta t^2 \tag{3.3.6}$$

$$\mathbf{v}(t+\delta t) = \mathbf{v}(t) + (1/2)\delta t(\mathbf{a}(t+\delta t) + a(t)) \tag{3.3.7}$$

This velocity Verlet algorithm does not require extra calculations to find positions and velocities at time t.

3.3.3 Langevin Dynamics

Langevin Dynamics simulations [27] is used to model and simulate atoms and molecules in a solvent. Assume that a molecule is in a fluid and that its mass is heavier than those of solvent particles. When these molecules collide with the fluid (solvent) molecules, the colliding particles move off in opposite directions. Consequently, in one dimension Langevin proposed that, the force experienced by a molecule could be expressed as a sum of two contributions.

The first one is an average force which is proportional to and acts in the opposite direction to the molecular velocity. This may be thought of as a frictional force. Therefore the equation of motion can be written as

$$m\frac{d\mathbf{v}(t)}{dt} = -m\gamma\mathbf{v}(t) + \mathbf{F}(t) \tag{3.3.8}$$

where $m\gamma$ is the friction coefficient. The force $F(t)$ is assumed to be due to external fields. From this equation, it can be seen that in the absence of external forces the molecules in a solvent come to rest. The second contribution is modelled as a random force and describes the result of the impact between solvent atoms and the molecules. This is a rapidly changing (in time) force. On including this force, the equation of motion now becomes

$$m\frac{d\mathbf{v}(t)}{dt} = -m\gamma\mathbf{v}(t) + \mathbf{F}(t) + \mathbf{R}(t) \tag{3.3.9}$$

where $\mathbf{R}(t)$ is the random force modelling the collisions of the molecule with the fluid atoms. Because it is a random force, it is usually taken from a Gaussian distribution. In Langevin Dynamics, at each new time step in the integration of the equations of motion, a new random force value is taken from the Gaussian distribution and scaled to the simulation temperature.

3.3.4 Periodic boundary conditions

In carrying out a MD simulation the system is modelled as a collection of atoms and molecules in a simulation box. In practice, two types of simulations can be carried out. A box with fixed boundaries is one in which outside the simulation box, there are either no atom/molecules or the atoms/molecules are given some positions consistent with the physics of the simulation being performed. For example, in simulating crystals with defects, the atoms outside the simulation box may be given positions consistent with contiuum elasticity theory. Alternatively, in carrying out a simulation to find the minimum energy configuration of a molecule, the molecule is positioned inside the simulation box and there are no atoms outside the box.

For many physical modelling problems, it is necessary to simulate infinite or semi-infinite structures. In such cases, it is useful to consider the use of periodic boundary conditions (PBC). It is particularly useful in modelling the properties of periodic struc-

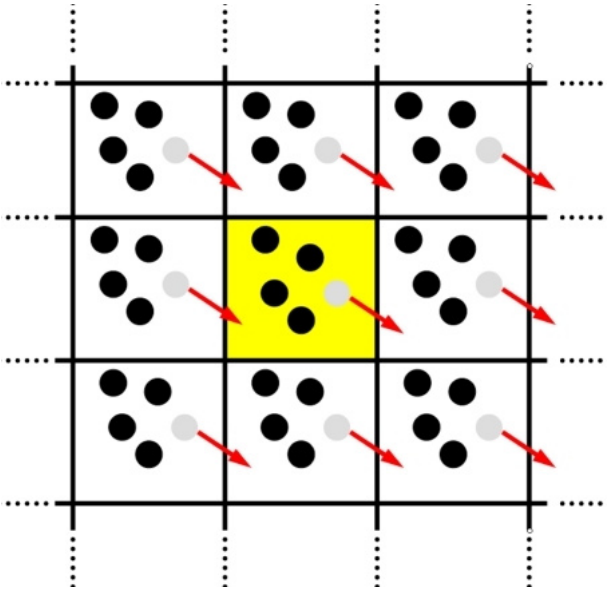

Figure 3.2: A schematic of periodic boundary conditions in two dimensions.

tures, like crystals. In this way, bulk properties of the system are determined by applying periodic boundary conditions. In these simulations, the particles (atoms and molecules) are positioned in a simulation cell that is infinitely replicated in all three dimensions. A feature of using PBC is that each particle in the main cell interacts with all the other particles in the cell and also with the atoms in neighboring cells. The periodic nature of the system means that when one particle leaves the simulation cell in one direction and enters a neighbouring cell, an identical particle moves into the simulation cell from the opposite side as shown in Figure 3.2. In this way, conservation of both momentum and particle density is achieved during the simulations. So, PBC is one way to model large systems which are periodic in one or more dimensions.

3.3.5 Neighbour lists

When carrying out a MD simulation, it is necessary to calculate the forces on each atom/molecule due to all the other atoms/molecules. If there are N atoms in a simulation,

the number of interactions that need to be considered goes like N^2. Such a scaling will have a strong impact on the computational time and severely affect the size of system that can be modelled. By constructing neighbour lists for each atom in the simulation box, it is possible to reduce the total number of computational operations and so reduce the computational time taken for a simulation. The neighbour list for each atom includes those atoms which are found within a distance less than r_n, where r_n is a specified distance which is in turn less than the cut-off distance of all the atom-atom interactions. This type of modeling improves the efficiency by neglecting the interactions at large separations. As the simulations proceeds the neighbour list requires updating as the particles are moving into or out of the region of radius r_n. However, this does not have to be done at every time step. To ensure the accuracy of the energy calculations, r_n should be chosen such that $r_n - r_c$ large enough that it does not neglect atoms that move across the potential cut-off radius.

3.4 Models for the simulation of molecular systems

3.4.1 All-Atom Molecular Dynamics (AAMD)

Although ab-initio methods at the electronic level would give the most accurate energies of molecular systems, these are too difficult to carry out because of the size of system and the time over which a simulation must be carried out. For this reason, empirical potential energy functions based on force fields between atoms are an appropriate and useful approach to give useful results. Therefore the AAMD model carries out simulations at the atomic level. In AAMD the motions of every atom including the solvent atoms are determined and thereby it simulates the behavior of a system with considerable accuracy. This allows the direct study of the dynamical and thermodynamical evolution of the system.

Due to high computational costs arising from the large number of atoms (more than

10 000 atoms) and the small time steps involved (10^{-15}s), a simulation of the equilibrium or non-equilibrium properties of a protein for just one nanosecond, for example, takes several weeks on a single processor. However, an accurate simulation of biomolecules in solution requires the ultimate level of detail in the internal representation of the system in molecular modeling and this is achieved by the use of the all atom model. There are a variety of force fields that have been employed to calculate forces on each atom. In this study, the CHARMM force field (which will be discussed later) was used to describe the interaction between all atoms.

3.4.2 Coarse-Grained molecular Dynamics (CGMD)

Coarse-grained molecular dynamics models were developed to reduce the computational costs in simulationg large biomolecular systems. Although they represent an approximation of biological macromolecules behavior, they can give some insight into molecular systems. In this model a small group of atoms is treated as a single bead (or particle) which is connected by (N-1) springs to neigbouring beads or particles. These beads represent a monomer of a chain as shown in the Figure 3.3. So, instead of looking at the system as a collection of atoms, it is approximated as a polymer chain formed by monomers.

An example of this is the lipid bilayer. It can be investigated using either the All-Atom model or by using the Coarse-Grained model. In the CG model all the atomistic details are not considered and so this allows the simulations to be carried out for a much longer periods of time. Thus CGMD allows a simulation to be carried for very long time periods which would be very difficult to achieve using micro μs scale dynamics involving all-atomic simulations. This advantage allows researchers to use CGMD simulations rather than AAMD simulations if the accuracy of energy calculations are of similar scale. In addition another advantage of CGMD is that it can be used for simulating very large systems for which AAMD simulations cannot be used easily as they require large computer resources. The monomer-monomer interactions in CGMD are defined by bonded and non-bonded

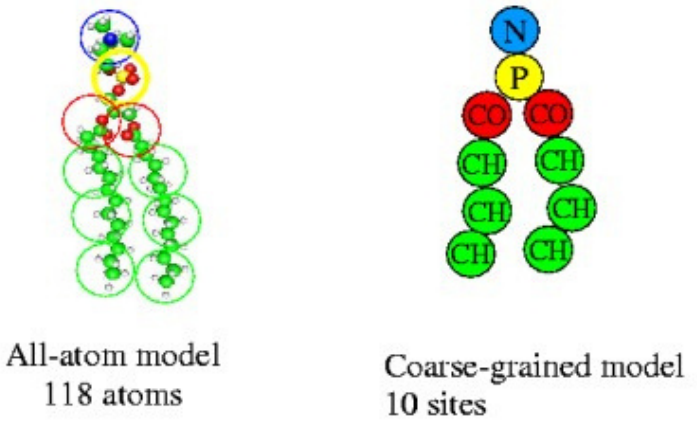

Figure 3.3: The difference between All-Atom and Coarse-Grained models in lipid bilayer molecule for example.

interactions. If it is important that if a more complicated set of interactions such as valence, torsional or electrostatic potentials force field needs to be used, these can be introduced into this model. With regard to the force fields that are popular, the Martini model has been used extensively. This model has also been used in some of the calculations reported in this thesis and will be explained in more detail later in this chapter.

3.5 Force fields

In a molecular dynamics simulation, an atom or molecule experiences the forces due to all the other atoms in the simulation cell.

Thus, the solution of the classical equations of motion for each atom are given by [28].

$$m_i \ddot{\mathbf{r}}_i = \mathbf{f}_i \tag{3.5.1}$$

$$\mathbf{f}_i = -\frac{\partial U}{\partial \mathbf{r}_i} \tag{3.5.2}$$

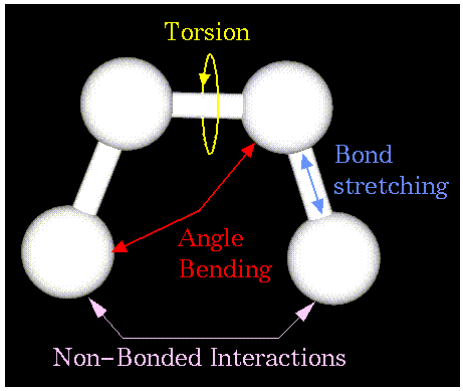

Figure 3.4: Bonded versus non-bonded interactions.

The force acting on each atom has to be calculated from differentiating the potential energy $U(\mathbf{r}^N)$, where $\mathbf{r}^N = (\mathbf{r}_1, \mathbf{r}_2 .... \mathbf{r}_N)$ represents the $3N$ atomic coordinates.

The total energy of the system at each stage of the MD or MC iteration process can be computed from the potential energy functions for a molecular system. In molecular interactions, the force field employed to describe the interactions between all particles is often refered to as a potential energy function. The force fields are a collection of equations and associated constants (parameters) designed to reproduce molecular geometry and selected properties of tested structures. In general, molecular interactions can be classified into two types of interactions; bonded with non-bonded interactions as shown in Figure 3.4. The following sections will explain the total interaction of the particles (bonding and non-bonded interactions) [29].

3.5.1 Bonded interactions

When atoms are connected to each other, it is often useful to describe the interaction as a bonding interacton. There can be more than one bond attached to one atom. Usually all nearest neighbours are connected to each other by bonds. The bonds can be thought of as springs attached to two atoms and as such they can stretch. So the simplest way of describing the bonding interaction is by a bond stretch energy term. If the distance

between two neighbouring atoms is at its equilibrium separation, the excess bond energy is zero. A useful representation of this is given by the equation below.

$$U_{bond} = \sum_{bonds\ i} K_i^{bond}(\mathbf{r}_i - \mathbf{r}_{oi})^2 \tag{3.5.3}$$

where $\mathbf{r}_i - \mathbf{r}_{oi}$ is the distance from equilibrium that the atom i has moved and K_i^{bond} is the bond force constant determines the strength of the bond.

When considering bonds between atoms, in addition to including the effects of bond stretching, it is also important to include the effects of bond bending (when there is a change in the bond angles) and torsion of the chain.

The bond bending energy is also represented by a quadratic potential, (see Figure 3.5)

$$U_{angle} = \sum_{angles\ i} K_i^{angle}(\theta_i - \theta_{oi})^2 \tag{3.5.4}$$

Here, $\theta_i - \theta_{oi}$ is the deviation of the bond angle from equilibrium between three bonded atoms, and K_i^{angle} is the bond angle force constant.

The dihedral angle describes the structure of a pair of atoms separated by three covalent bonds with the central bond subject to the torsion angle ϕ. The torsional twist of the chain can similarly be represented by the equation

$$U_{dihedral} = \sum_{dihedral\ i} \left\{ \begin{array}{ll} K_i^{dihedral}[1 + cos(n_i\phi_i - \gamma_i)] & n_i \neq 0 \\ K_i^{dihedral}(\phi_i - \gamma_i)^2 & n{=}0 \end{array} \right\} \tag{3.5.5}$$

where $K_i^{dihedral}$ is the dihedral force constant, n is an integer constant with a positive value and specifies the periodicity, and γ_i is the phase shift. The geometry of the structure between four atoms is described by the improper dihedral term.

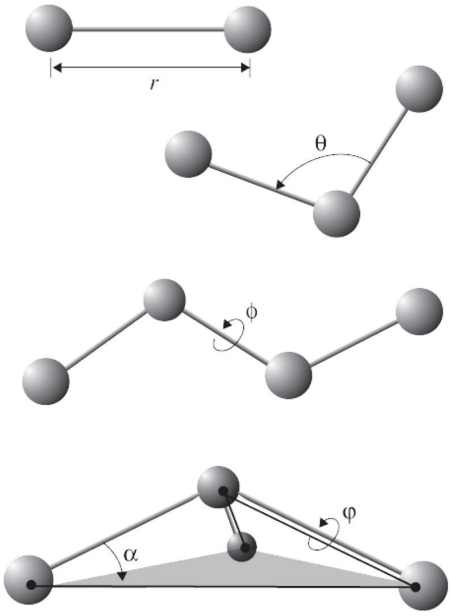

Figure 3.5: Internal coordinates for bonded interactions: r governs bond stretching; θ represents the bond angle term; ϕ gives the dihedral angle; the small out-of-plane angle α is governed by the so-called "improper" dihedral angle φ. [30]

3.5.2 Non-bonded interactions

The non-bonded interactions are those between atoms which are not connected to each other by bonds. One of these interactions is due to the dipole-dipole interactions which are often described by the Morse or Lennard-Jones functions. The functions describe the energy between two atoms (i and j) separated by a distance $r_{ij} = |\mathbf{r}_i - \mathbf{r}_j|$.

These interactions are weakly attractive for two atoms as they come close to each other from infinity and becomes repulsive at short ranges. Adding these two terms give rise to a minimum energy in the potential energy function. The repulsive term ensures that two atoms cannot occupy the same space due to Coulombic repulsion. The attractive interactions result from induced dipole-dipole interactions and so is referred to as the van der Waals interaction (vdw). The van der Waals potential energy U_{vdw} can be represented

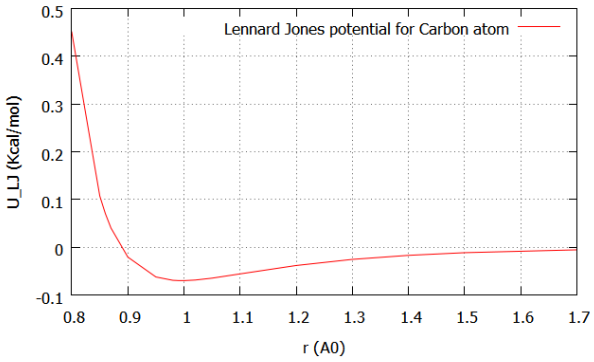

Figure 3.6: The variation of Lennard-Jones potential energy as a function of separation distance between the two carbon atoms.

by the Lennard-Jones potential energy function U_{LJ};

$$U_{LJ}(r_{ij}) = \frac{a}{r_{ij}^{12}} + \frac{b}{r_{ij}^{6}} \tag{3.5.6}$$

where r_{ij} represents the distance between monomers; i and j. a, b are parameters that depend on the type of interacting atoms and determine the depth of the potential energy function and the distance of closest approach. An example of the Lennard-Jones potential for carbon C atom is shown in Figure 3.6.

The interaction between non-bonded atoms can also be described by a Morse potential function U_{Morse};

$$U_{Morse}(r_{ij}) = D\{\exp^{-2\alpha(r_{ij}-R_e)} - 2\exp^{-\alpha(r_{ij}-R_e)}\} \tag{3.5.7}$$

where D is a depth of potential well, α determines the shape of the well and R_e is the equilibrium spacing between two atoms interacting via the Morse potential energy function. Of more importance, especially in modelling protein structures is the electrostatic interaction. This is due to the long range Coulomb force which can be either attractive

or repulsive depending on the signs of the partial charges on each atom

$$U_{coulomb}(r_{ij}) = \frac{Q_1 Q_2}{4\pi\epsilon_0 r_{ij}} \tag{3.5.8}$$

where Q_1, Q_2 are the charges and ϵ_0 is a permittivity.

3.5.3 The total energy

The total energy of a collection of atoms and molecules in a MD simulation can then be calculated from a knowledge of the interatomic potential energy functions by summing up the contributions. Then, we find

$$U_{total} = U_{bond} + U_{angle} + U_{dihedral} + U_{vdw} + U_{coloumb} \tag{3.5.9}$$

3.5.4 CHARMM All-Atom force field

CHARMM (Chemistry at HARvard Molecular Mechanics), is a type of force field and uses a common force field to present the total potential energy function as a sum of five contributions which is called CHARMM all-atom general force field or CGenFF [2]. The parameters used in the force fields can be used for proteins, nucleic acids, lipids and carbohydrates. The parameters were determined by comparing the results of the total energy to those obtained by quantum mechanical methods. There are a number of force fields that were developed for large molecules in condensed phases. The CHARMM program was one of the programs that was developed in 1980s and used an extended atom force field with no explicit hydrogens [31]. The subsequent CHARMM19 parameters were then produced and replaced the CHARMM program in which hydrogen atoms bonded to nitrogen and oxygen were explicitly presented, while hydrogens bonded to carbon or sulfur are treated as part of extended atoms. The parameterization of this model were fitted to quantum calculations which were used with implicit solvent models and aimed

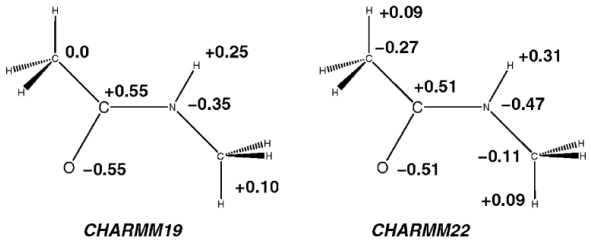

Figure 3.7: Charge models for N-methylacetamide for two of the CHARMM force field parameterizations. In CHARMM19, the methyl groups are treated as united atoms, so that there is no breakdown into separate C and H charges.[31].

to achieve a good balance of the interaction energies between water-water and solute-water. Then in 1990s, the group noticed that there is a need to refine the parameters to include interaction energies in explicit solvent simulations. This resulted in a new version of CHARMM which was named the CHARMM22 protein force field. One feature of the CHARMM force field parameter is the enforcement of neutral group which are small sets of adjacent atoms whose atomic charges are compelled to sum to zero as shown in the Figure 3.7.

After that CHARMM27 was released which is identical to the CHARMM22 which extensive reworking of the nucleic acid parameters. Those types of CHARMM models provided for proteins, nucleic acids, ethers, carbohydrates, and small molecules. More recently CHARMM27 was replaced by CHARMM36, which was optimised for heterogeneous biomolecular systems, because of the lower surface area lipids and higher deuterium order parameters compared to experiment. There are other good reasons for replacing CHARMM27 by CHARMM36 [32] in order to achieve good agreement with experiment. Six types of lipids were simulated with this model and the total density profiles, improving the hydration of lipids near the carbonylglycerol section of phospholipids and allowing to use for a tensionless ensemble (NPT) in MD simulations was demonstrated. In our simulations the CHARMM27 parameters were used to model the proteins structures and CHARMM36 parameters were employed in the modelling of the lipid bilayer. These were combined to calculate the potential energy due to the interactions of atoms.

3.5.5 Martini Coarse-Grained (CG) force field

The Martini force field is a coarse-grain force field suited for molecular dynamics simulations of biomolecular systems. This model was produced for lipids in 2004 by Marrink and *et al* for lipids and then further developed for other type of molecules in 2007 [33]. The MARTINI model, which is the extension of the CHARMM force field, has been used to calculate the forces between interaction sites. In this model, on average four heavy atoms are represented by a single coarse-grain bead. However, for other structures such as the ring structure, the mapping is different. The strategy of this model is therefore to include as many CG sites as necessary in order to keep the ring geometry, typically resulting in a 2 or 3 to 1 mapping of ring atoms onto CG beads. A special particle set, labeled "S", which can be used to model ring structures such as benzene and sterol bodies such as cholesterol. This is separated from the other structure because they reduced the effective interaction size and strength in the ring-ring interaction such as LJ potential. For this reason the ring particles are closely kept together without any freezing. The CG model for water is also different as water is the only molecule that has a specific problem in CG modelling as it has a freezing temperature that is somewhat too high compared to real water. In this case water is modeled as P4 particles. In practice the freezing process means that the CG water can remain fluid for very long times (microseconds, or for as long as the simulation is performed). In general, the interaction sites can be classified into four sites; polar (P), nonpolar (N), apolar (C) and charged (Q). Then they are divided into 5 numbers which represents the degree of polarity or by a letter indicating the hydrogen-bonding capability (d= donor, a= acceptor, da =both, and 0=none). This subdivision is for more accurate while being representative of the chemical nature of the atomic structure. Figure 3.8 shows the mapping between atomic structure and the coarse-grained model for DPPC, cholesterol and benzene. The Martini coarse-grained model has been used in some applications including vesicle formation and fusion, lamellar phase, transformations, the structure and dynamics of membraneprotein assemblies, the

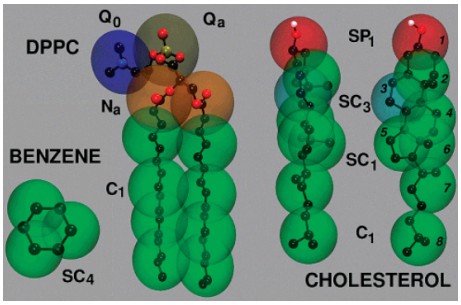

Figure 3.8: Mapping between the chemical structure and the coarse-grained model [33].

structure of bicelles, the equation of state of monolayers, and the effect of various molecules on membranes (butanol, DMSO, dendrimers). In our study we used this model to study coarse-grained of the protein Ubiqutin in order to compare the results with those obtained using all-atom force fields, and also to study CG of the lipids when interacts with CG of CNT.

3.6 Molecular Dynamics with NAMD

NAMD (Nanoscale Molecular Dynamics) [30] is a molecular dynamic code written in C++ and based on CHARMM++. It is a parallel, object-oriented program based on C++ and developed in the Parallel Programming Laboratory at the University of Illinois. It was developed for very fast powerful simulations of large systems of particles. It is free of charge and designed for efficient parallel computing, on a large parallel computer. Yet, it can be run on other platforms such as single computers including laptops. It uses the gradient of a scalar potential for the inter-atomic interactions. It was built by the theoretical and computational biophysics group in the Beckman Institute for advanced science and technology at the University of Illinois at Urbana-Champaign.

VMD [34] is a molecular graphics software written in C++ and developed for the three dimensional visualization, presentation and analysis of the molecular system. It is also a free of charge program and includes a documentation guide describing how to run,

install, use, and alter the program for different hardware and software layouts [35]. The molecules loaded into VMD can be represented in many styles such as coloring method, number of structures and etc. A main feature of NAMD is that it is compatible with VMD and can be linked to it. Thus, a simulation can be seen at the same time as it is being computed.

3.6.1 Using NAMD

There are several necessary inputs required by NAMD in an MD simulation. One of these is the Protein Data Bank (PDB) file which can be downloaded from (http://www.pdb.org) or made by a user manually. This includes knowledge about atomic coordinates for a whole structure. The second is a protein structure file (PSF). In order to get this, a topology file (as defined below) is needed. The (PSF) file contains structural information of the molecule such as atoms, bonds, angles, dihedrals, impropers and etc. The third is a parameter file which maintains bonding and non-bonding interaction parameters for all particles in the system. There are four different types of force-field parameters that have been developed such as CHARMM, X-PLOR, AMBER, and GROMOS, and NAMD is able to call all of them. The last input or simulation file is a configuration or NAMD file. This is made by the user and should specify all choices that is required by NAMD in order to run a simulation. The details of all four files have been explained in NAMD user Guide [36]. The following paragraph explains the steps to create PSF and PDB files and utilizing them to run an MD simulation using the NAMD package.

- PSFGEN is a package supplied with NAMD which can be applied to modify the coordinates of the PDB file or as a PSF builder.

- The topology file describes the link between atoms through the chemical bonds such as bonds, angles, and dihedrals to generate PSF files.

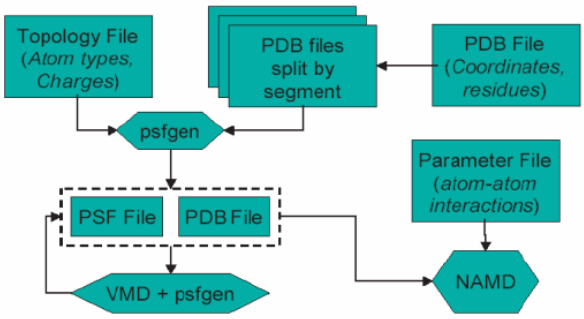

Figure 3.9: Flowchart specifies the role of files as used by NAMD, VMD and Psfgen.

Figure 3.9 shows the flowchart of using files by NAMD, VMD and PSFGEN. This explains how the PSF file is created from the topology files and the PDB file by running the PSFGEN plugin.

All information about any atoms in the PDB files must be given by the topology file. Then the PDB and PSF files can be built using PSFGEN. PSFGEN needs two files, one that includes all coordinates of the particles and the other one is a topology file to model the structure. Therefore, the PSF and a new PDB, which contains all coordinates of every atom in the whole system, of the structure are constructed. Subsequently, parameter files are then needed to run the NAMD program. In this thesis the CHARMM parameters and Martini model, which includes all force field parameters have been used in all the simulation studies.

3.6.2 Data files

The main data files needed to do carry out a simulation of a system using NAMD are the PSF, PDB, parameter and configuration files as explained in the previous section. An example of PDB and PSF files are shown in the Figures 3.10 and 3.11. The PDB file includes all information about type and number of atoms, residue number and residue name, and x, y, and z coordinates. The PSF file contains the mass and the partial charges and the structure information such as which atom bonded to other and so on. When the

```
ATOM      1  N    POPCL   1      -42.284 -47.357  21.137  0.00
0.00      L11  N
ATOM      2  C12  POPCL   1      -41.557 -46.575  22.255  0.00
0.00      L11  C
ATOM      3  C13  POPCL   1      -42.408 -46.598  19.912  0.00
0.00      L11  C
ATOM      4  C14  POPCL   1      -41.649 -48.638  20.820  0.00
0.00      L11  C
ATOM      5  C15  POPCL   1      -43.693 -47.770  21.555  0.00
0.00      L11  C
ATOM      6 H12A POPCL   1      -40.792 -45.931  21.659  0.00
0.00      L11  H
ATOM      7 H12B POPCL   1      -41.035 -47.263  22.932  0.00
0.00      L11  H
```

Figure 3.10: A section from a typical PDB file.

```
         1 L11  1    POPC N    NTL   -0.600000       14.0067
0
         2 L11  1    POPC C12  CTL2  -0.100000       12.0107
0
         3 L11  1    POPC C13  CTL5  -0.350000       12.0107
0
         4 L11  1    POPC C14  CTL5  -0.350000       12.0107
0
         5 L11  1    POPC C15  CTL5  -0.350000       12.0107
0
         6 L11  1    POPC H12A HL     0.250000        1.0079
0
         7 L11  1    POPC H12B HL     0.250000        1.0079
0
```

Figure 3.11: A section from a typical PSF file.

structure is made, all information of each atom in the system is needed which is called parameter file, a typical CHARMM parameter file has been shown in the Figure 3.12. Then to run a molecular dynamics simulations with NAMD one more file is needed which is called configuration file as shown in the Figures 3.13 and 3.14. In some cases such as moving an atom through a pore or calculating free energy or applying force to the system, there are other secondary files that are needed which can be found in the NAMD user Guide [36].

3.7 Calculation of the Free Energy

The free energy calculation method is an important one in investigating the structure biological systems particularly when it is desirable to understand the behavior of

```
BONDS
!V(bond) = Kb(b - b0)**2
!Kb: kcal/mole/A**2
!b0: A
!atom type Kb          b0
CTL3  CL    200.0       1.522    ! methyl acetate

ANGLES
!V(angle) = Ktheta(Theta - Theta0)**2
!V(Urey-Bradley) = Kub(S - S0)**2
!Ktheta: kcal/mole/rad**2
!Theta0: degrees
!Kub: kcal/mole/A**2 (Urey-Bradley)
!S0: A
!atom types     Ktheta    Theta0   Kub     S0
OBL  CL   CTL3    70.0     125.0     20.0   2.442  !

DIHEDRALS
!V(dihedral) = Kchi(1 + cos(n(chi) - delta))
!Kchi: kcal/mole
!n: multiplicity
!delta: degrees
!atom types             Kchi    n   delta
X    CTL1 OHL  X        0.14    3     0.00 ! glycerol

NONBONDED nbxmod  5 atom cdiel fshift vatom vdistance vfswitch
cutnb 14.0 ctofnb 12.0 ctonnb 10.0 eps 1.0 e14fac 1.0 wmin 1.5
!V(Lennard-Jones) = Eps,i,j[(Rmin,i,j/ri,j)**12 - 2
(Rmin,i,j/ri,j)**6]
!epsilon: kcal/mole, Eps,i,j = sqrt(eps,i * eps,j)
!Rmin/2: A, Rmin,i,j = Rmin/2,i + Rmin/2,j
!atom  ignored    epsilon      Rmin/2   ignored   eps,1-4
Rmin/2,1-4
HOL      0.0       -0.046     0.2245
CL       0.0       -0.0700    2.00   ! methyl acetate update
```

Figure 3.12: A typical CHARMM parameter file which embraces the parameters for the different force-filed components.

```
#############################################################
## ADJUSTABLE PARAMETERS                                   ##
#############################################################
structure          lipid_gold.psf
coordinates         lipid_gold.pdb
set temperature    300

 set outputname     lipid_gold_output
if (1) {
set inputname   restartfile
binCoordinates $inputname.coor
#binVelocities $inputname.vel ;#if the temperature is given
this file doesn't needed
extendedSystem $inputname.xsc
}
firsttimestep     1

#############################################################
## SIMULATION PARAMETERS                                   ##
#############################################################
# Input
paraTypeCharmm      on
parameters      par_all36_lipid_gold.prm
temperature      $temperature
# Force-Field Parameters
exclude             scaled1-4
1-4scaling          1.0
cutoff              12.0
switching           on
switchdist          10.0
pairlistdist        14.
outputPairlists      0
pairlistShrink       0.01
pairlistGrow         0.01
pairlistTrigger      0.3
margin               3.0
vdwForceSwitching      on
```

Figure 3.13: A typical configuration file which embraces set up of the MD simulations in this case the gold nanoparticle placed at the top of the lipid bilayer.

```
# Integrator Parameters
timestep            2.0  ;# 2fs/step
rigidBonds          all  ;# needed for 2fs steps
nonbondedFreq       1
fullElectFrequency  2
stepspercycle       10
# Constant Temperature Control
langevin            on    ;# do langevin dynamics
langevinDamping     10     ;# damping coefficient (gamma) of
1/ps
langevinTemp        $temperature
langevinHydrogen    off    ;# don't couple langevin bath to
hydrogens

useGroupPressure yes ;# needed for rigidBonds
useFlexibleCell yes
useConstantRatio yes
useConstantArea       no
langevinPiston         on
langevinPistonTarget  1.01325 ;#  in bar -> 1 atm
langevinPistonPeriod  400.0
langevinPistonDecay   300.0
langevinPistonTemp    $temperature
wrapAll          yes
wrapWater        yes

# PME (for full-system periodic electrostatics)
PME                 on
PMEGridSpacing      1.2

restartfreq         20000     ;# 500steps = every 1ps
dcdfreq             20000
xstFreq             20000
outputEnergies      10000
outputtiming        20000
outputPressure      20000
numsteps            30000000
```

Figure 3.14: Continue of the previous figure.

the processes involved. The absolute free energy for a physical state cannot usually be calculated directly but the relative free energies between physical states can be calculated using several different techniques. Through knowledge of this, it is possible to establish stable states, their thermodynamics properties, the phase transitions between states, and it is also possible to infer how stable states are changed by external conditions or other transformations. Based on the transform between different states, the calculation of the free energy of biological systems can be distinguished into two main terms; geometrical and alchemical transformations [37]. They both depend on changes in a function of atomic coordinates or changes in the Hamiltonian parameter. The geometrical transformation refers to those molecular systems which do not include any chemical modification, but embraces virtually any geometric alteration in a molecule. The alchemical transformation however encloses structural alteration of chemical species that rest upon the remarkable malleability of the potential energy function in molecular mechanics based simulations, reminiscent of the famed ability of alchemists to transmute base metals into noble ones such as gold. The methods used in free energy calculations for alchemical transformation are perturbation and thermodynamic integration methods. However, the adaptive bias force method has been used in free energy calculation of geometric transformations. The thermodynamic quantity of free energy can be calculated using the Helmholtz or Gibbs free energy which depends on the statistical ensembles. The canonical ensemble (constant temperature and volume) uses the Helmholtz free energy and the isothermal-isobaric ensemble (constant temperature, constant pressure) uses the Gibbs free energy G term. The Helmholtz free energy is given by:

$$A = U - TS \tag{3.7.1}$$

where U is the internal energy (kinetic plus potential energy), T the temperature, and S the entropy. The Gibbs free energy is similar but with an additional PV term where P is

the pressure and V the volume as follows:

$$G = A + PV \tag{3.7.2}$$

In this thesis, the Gibbs free energy has been used as the thermodynamic system at constant NPT. This absorbs heat energy from reservoir and the work energy expends to make room for it. The free energy differences ΔA can be calculated in three possible ways. First, by estimating the significant probability distribution,

$$\Delta A = \frac{-1}{\beta} \ln \frac{\rho(U(\vec{r}_1, ..., \vec{r}_N))}{\rho_0} \tag{3.7.3}$$

where ρ_0 is the normalization term, β is $(1/K_B T)$. Second, by calculating the free energy differences directly, and third, by computing the free energy derivative along some order parameter consistent with an average force and integrating the latter to obtain ΔA. There are other algorithms to compute the free energy, such as umbrella sampling, thermodynamic perturbation and thermodynamic integration, Metadynamics, and adaptive bias force. In umbrella sampling the free energy is calculated along the reaction coordinates from one thermodynamic state to another. The thermodynamic integration method is based on the difference in a free energy property of the system between some reference state and the state of interest by characterizing parameters of the system which are altered infinitely slowly so that the system is in equilibrium at each stage along the path. The metadynamics method takes the normal evolution of the system which is biased by a history dependent potential that is constructed as a sum of Gaussians centered along the trajectory followed by a suitably chosen set of collective variables. The last method, the adaptive biasing force which is advanced from umbrella sampling and has been used in this thesis and is explained in the following section.

3.7.1 Adaptive biasing force (ABF)

The adaptive bias force method is used for calculating the free energy along transition coordinates and can be seen as a potential from the average force. This method is based on the formalism of thermodynamic integration as the quantity of the average force is calculated directly. Subsequently, this force is integrated to provide the potential. The aim of this method is to improve the efficiency of molecular dynamics simulations by sampling the potential energy surface ineffectively due to free energy barriers. So this algorithm computes the free energy along a chosen reaction coordinate (ξ) such as the distance between the center of mass of two molecules using Collective Variables-based Calculations Module (Colvars) [38] with NAMD to define the transition coordinate as follows;

$$A(\xi) = \frac{-1}{\beta} \ln P_{\xi} + A_0 \tag{3.7.4}$$

where $A(\xi)$ is the free energy of the state at a particular value of (ξ). P_{ξ} is the probability density of finding the system of interest at ξ. A_0 is a constant. This method samples a reaction coordinate and implements a continued biasing force which is tuned during simulations to the progressively evaluate the free energy. This model works adaptively and requires no knowledge about the potential of mean force. This is achieved by on-the-fly evaluating the derivative of the free energy landscape at each point along the pathway. Then, at that moment, an external biasing force is employed exactly canceling of the average force. The derivative of the free energy with respect to the reaction coordinate represented as follows;

$$\frac{dA(\xi)}{d\xi} = \left\langle \frac{\partial \nu(x)}{\partial \xi} - \frac{1}{\beta} \frac{\partial \ln |J|}{\partial \xi} \right\rangle_{\xi} = - < F_{\xi} >_{\xi} \tag{3.7.5}$$

where the first part represents the Cartesian forces exerted on the system which is derived from the potential energy function $\nu(x)$. The second term expresses the geometric correc-

tion created from the change of generalized to Cartesian coordinates which implies for the difference in phase space availability as the reaction coordinate changes, where $|J|$ is the determinant of the Jacobian for the transformation. The $< F_\xi >_\xi$ term is the derivative of the instantaneous force component which is the average force acting along reaction coordinates. The details of this algorithm are explained in [39, 40] as it developed and implemented into the NAMD by Eric Darve, Andrew Pohorille, Jeffrey Comer and *et al.* The significance of this method is not crucial in the equal exact quantity of mean force and biasing force, but it is important that the biasing force develops sufficiently uniform sampling of the passage coordinate that the surviving barriers can be easily crossed in reaction to thermal fluctuations. Recently, this method has been used in many biomolecular system applications to obtain the free energy profile of a desired event. In this thesis we have been used this approach to calculate the free energy profile for the interaction between gold nanoparticle with POPC lipid bilayer in Chapter 6.

3.8 Steered Molecular Dynamics simulations

In molecular dynamics simulations time scales are important in the transitions from one equilibrium state to another. These can be tens of nanoseconds in biomolecular systems. In order to fix this issue, external force applications have been employed to guide the interest system to enhance sampling along the transition states. Steered molecular dynamics (SMD) techniques are one of the external forces which can be used either by applying a constant force to an atom (or a molecule) or by applying a constant velocity pulling via attached a harmonic restraint to a dummy atom. The idea behind this technique is similar to the method of umbrella sampling which is to look to improving the sampling at a particular states in a biomolecular system. The difference between these two algorithms is that while the umbrella sampling needs a series of equilibrium simulations, in the SMD approach a constant force is applied and results in important

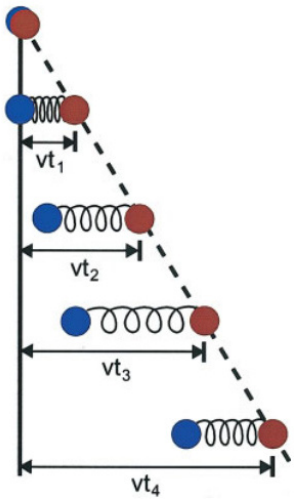

Figure 3.15: Pulling in a one-dimensional case. The dummy atom is colored red, and the SMD atom blue. As the dummy atom moves at constant velocity the SMD atom experiences a force that depends linearly on the distance between both atoms. This picture is taken from [30]

deviations from equilibrium which means that the system is a non equilibrium state. The advantage of this technique is that a relevant movement of the desired molecule can be obtained in a relatively short time and while all the atomistic details are available to be processed.

In constant force SMD, the force applied to the atom should be kept fixed by moving the constraint point to keep the force constant on a restraint which results a variable velocity. The range of the typical applied force to an subject depends on the system and is from tens to a few thousand picoNewtons (pN). This external force should stay limited over a translocation time and control the length of the simulations.

If this is not done, the constant force is not applicable in that stage which is a drawback of this method. In a constant velocity SMD one atom or a center of mass of molecule is harmonically restrained to a point in space and attached to a dummy atom through a virtual spring in a chosen direction by a force constant k with strength of the restraint as shown in the Figure 3.15.

The additional potential (U) is applied to measure the force between the atoms with a force constant k moving with a velocity $\mathbf{v}$ in the direction $\mathbf{n}$;

$$\mathbf{F} = -\nabla U \tag{3.8.1}$$

$$\nabla U = \frac{1}{2}[\mathbf{v}t - (\mathbf{r} - \mathbf{r}_0).\mathbf{n}]^2 \tag{3.8.2}$$

where t is the time, $\mathbf{r}$ is the actual position of the SMD atom, $\mathbf{r}_0$ is the initial position of the SMD atom and $\mathbf{n}$ is the direction of pulling. The NAMD package is implemented for using this technique.

Chapter 4

Elastic properties of POPC lipid bilayer

4.1 Introduction

Membrane cells are important and crucial in allowing nutrients and waste into and out of the cell. So, it is important to have a good understanding of the deformation properties of membranes, especially when they are in contact with other molecules and particles. This is because of the possible implications on the mechanical stability of cell tissues. The elastic properties of membrane cells makes them bendable and also allows them to undergo compression or tension. The elasticity of a membrane complex is, in general, anisotropic. However, the head and tail molecules of the lipid bilayer, though having different elastic moduli, are individually both homogeneous and isotropic.

From the theoretical aspect, the mechanical properties of lipid bilayer membranes have commonly been investigated using approaches based on the Helfrich Hamiltonian [41]. Different techniques have been used to calculate the elastic moduli of materials, including second derivative methods, molecular dynamics MD simulations, empirical force constant models, and finite elasticity theory based on deformation methods. The main physical

quantity determined from most studies is the bending rigidity. The elastic properties of lipid bilayer membranes have been measured experimentally and determined computationally using a number of biological processes such as membrane fusion [42] and the modulation of membrane channel activities [43]. Membrane deformations caused by proteins which result in small membrane curvatures have been studied by Aranda-Espinoza [44] who found that the absorption of an inclusion in the membrane results in the spontaneous curvature of each monolayer of the bilayer which in turn can be expressed in terms of the stretching and bending moduli.

Young's modulus of volume stretching-compression in the lateral and normal directions of the headgroup molecules of the bilayer was found by Campelo *et al* [45] to be 4×10^9 N/m^2 and for the tailgroup molecules was 1×10^9 N/m^2. Tajparast *et al* [46] using electrostatic/electrokinetic forces to deform the lipid bilayers found that the elastic moduli of the headgroups were much higher (by a factor of four) than that of the tail groups. Coarse grained Monte Carlo (MC) simulations have also been used to find Young's modulus and Poisson's ratio of lipid bilayers in different phases [47].

In this thesis we have used the finite theory of elasticity to calculate the second order elastic constants of POPC lipid bilayer membrane using MD simulations. This was done by applying a homogeneous strain deformation to a system in equilibrium and then determining the increase in elastic energy using constrained molecular dynamics. We have also investigated the elastic stability of a lipid bilayer with molecular defects. In particular, we have calculated the elastic constants of lipid bilayers with missing leaflets one and/or two leaflet molecules and compared these with that of the perfect bilayer membrane. The following sections explain the methods use for finding the anisotropic elastic constants of the POPC bilayer.

4.2 Calculations of the elastic constants of POPC lipid bilayers

The elastic constants of the lipid bilayer POPC membrane in solution were determined by calculating the energy of the three different configurations referred to above. From these elastic constants the bulk modulus, thickness compressibility modulus and mean curvature elastic modulus for the lipid bilayer can be found.

To determine the elastic constants from the elastic energy of a strained lipid bilayer, it is useful to formulate the deformation in terms of the strain tensor. This is called the homogeneous deformation method. A general strain tensor will result in a change to both the shape and size of a unit cell. A method to change both shape and size of a molecular dynamics cell has been explained by Parrinello and Rahman [48, 49]. In this formulation, the MD cell tensor **h** is defined as a 3 × 3 matrix which is used to represent the shape and size of the MD cell. The MD cell edge vectors are **a**, **b**, and **c**. Thus, the **h**-matrix is defined as

$$\mathbf{h} = \begin{bmatrix} a_1 & b_1 & c_1 \\ a_2 & b_2 & c_2 \\ a_3 & b_3 & c_3 \end{bmatrix} \tag{4.2.1}$$

In their method, Parrinello and Rahman combined MD simulations with the theory of finite elasticity [50, 51] by considering a EhN ensemble in which not only is the volume (V = det (h)) kept constant but also the shape of periodically repeating MD simulation cell containing the N particles.

The cell shape tensor **h** is a scaling matrix that transforms all points in the MD cell into a cubic unit cell. Before applying any deformation to the system, the matrix $\mathbf{h_o}$ is taken as the reference state which represents the cell size and shape at zero stress value.

From the finite theory of elasticity, the strain tensor ε is

$$\varepsilon = \frac{1}{2}(\tilde{\mathbf{h}}_o^{-1}\mathbf{G}\mathbf{h}_\mathbf{o}^{-\mathbf{1}} - \mathbf{I}) \tag{4.2.2}$$

where $\mathbf{G}$ is the metric tensor and defined as a matrix $\mathbf{G} = \tilde{\mathbf{h}}\mathbf{h}$, and the tilde indicates matrix transposition [52] and $\mathbf{I}$ represents the identity matrix. Then the metric tensor, $\mathbf{G}$, can be obtained from the inversion of the finite strain

$$\mathbf{G} = \tilde{\mathbf{h}}_\mathbf{o}(\mathbf{2}\varepsilon + \mathbf{I})\mathbf{h}_\mathbf{o} \tag{4.2.3}$$

Thus the cell parameters can be represented as a function of applied strain with the cell lengths given by $a = \sqrt{G_{11}}$, $b = \sqrt{G_{22}}$, and $c = \sqrt{G_{33}}$. Here G_{ij} are the matrix elements of the $\mathbf{G}$ matrix. The nonzero components of the cell edge vectors $\mathbf{a}$ and $\mathbf{b}$ are given by $a_3 = G_{13}/c_3$, $b_3 = G_{23}/c_3$, $a_2 = (G_{12} - a_3 b_3)/b_2$.

4.2.1 Voigt notation

The second derivative of the total energy of a system with respect to the small strain gives the elastic constants of the system. In order to simplify the notation, the strain tensors and the elastic constants are usually expressed in a contracted form. This is termed Voigt notation. Thus, for example, a 6-component vector notation is used for a system with rhombohedral symmetry.

In Voigt notation, the contracted strain tensor elements for our system [53, 54], are $\eta_1 = \varepsilon_{11}$, $\eta_2 = \varepsilon_{22}$, $\eta_3 = \varepsilon_{33}$, and the for $\eta_4 = \varepsilon_{23} + \varepsilon_{32}$, $\eta_5 = \varepsilon_{13} + \varepsilon_{31}$, and $\eta_6 = \varepsilon_{12} + \varepsilon_{21}$. There are only six independent elements.

The full strain tensor is therefore

$$\begin{bmatrix} \varepsilon_{11} & \varepsilon_{12} & \varepsilon_{13} \\ \varepsilon_{21} & \varepsilon_{22} & \varepsilon_{23} \\ \varepsilon_{31} & \varepsilon_{32} & \varepsilon_{33} \end{bmatrix} = \begin{bmatrix} \eta_1 & (1/2)\eta_6 & (1/2)\eta_5 \\ (1/2)\eta_6 & \eta_2 & (1/2)\eta_4 \\ (1/2)\eta_5 & (1/2)\eta_4 & \eta_3 \end{bmatrix} \tag{4.2.4}$$

Upon deformation, the strain energy, using a Taylor expansion to third order, is given by

$$E(V,\delta) = E(V_o,0) + \frac{V_o}{2!}\sum_{IJ} C_{IJ}\eta_I\eta_J + \frac{V_o}{3!}\sum_{IJK} C_{IJK}\eta_I\eta_J\eta_K \tag{4.2.5}$$

where once again, Voigt notation has been used to write the elastic energy in terms of the contracted elastic constants

$$C_{11} = C_{1111}; \quad C_{12} = C_{1122}, \quad \text{etc}$$

V is the volume of the system and the parameter δ, which is not shown explicitly in equation (4.2.5), is used to represent the magnitude of the strain.

4.2.2 Determination of the elastic constants

In order to determine all the elastic constants, the system is given a strain, with a particular value of the strain parameter δ, and the elastic energy calculated. The strain parameter was then gradually increased and the resulting elastic energy as a function of δ plotted. Then, by fitting the energy-strain curve with a polynomial, the second derivatives and hence the elastic constants may be determined. While it may be possible to determine the elastic constants directly from the stress tensor in the molecular dynamics simulation, the latter is not very reliable because of the relatively large pressure fluctuations during the simulations.

In practice, it may be noted that the elastic constants can be classified into two parts:

- Diagonal terms - C_{11}, C_{22}, etc;
- Off-diagonal terms - eg, C_{12}, etc.

It is straight forward to determine the diagonal terms as the strain is applied along just one direction. For example, to determine the C_{11} elastic constant, the MD cell is strained all the x-direction by increasing amounts, δ,

$$\epsilon_{11} = \begin{bmatrix} \delta & 0 & 0 \\ 0 & 0 & 0 \\ 0 & 0 & 0 \end{bmatrix} \tag{4.2.6}$$

which results in the strain energy for a volume, V, being given by

$$E(\delta) = E(0) + \frac{1}{2}\left(\frac{\partial^2 E}{\partial \delta^2}\right)_0 \delta^2 + ... \tag{4.2.7}$$

$$= E(V_0, 0) + \frac{V}{2} C_{11}\delta^2 + ... \tag{4.2.8}$$

This can then be fitted by a polynomial of form

$$E(\delta) = a + b\delta^2 + ... \tag{4.2.9}$$

giving

$$C_{11} = \frac{1}{V}\left(\frac{\partial^2 E}{\partial \delta^2}\right)_o = \frac{2b}{V} \tag{4.2.10}$$

The C_{22} and C_{33} elastic constants can be found in the same way but with strains, ϵ_{22} and ϵ_{33} respectively.

In order to determine the off-diagonal elastic constants, the system must be subject to deformations along at least two different directions because these elastic constants are related to a combination of second derivatives of the elastic energy. For example, to

determine C_{12}, the strain tensor is defined as

$$\epsilon = \begin{bmatrix} \delta & 0 & 0 \\ 0 & \delta & 0 \\ 0 & 0 & 0 \end{bmatrix} \tag{4.2.11}$$

which in turn, results in the elastic energy, to second order, being expressed as

$$E(\delta) = E(0) + \frac{V}{2}(C_{11} + C_{22} + C_{12} + C_{21})\delta^2 + ... \tag{4.2.12}$$

The symmetry of elastic constant tensor means that $C_{11} = C_{22}$ and $C_{12} = C_{21}$. Hence,

$$E(\delta) = E(0) + V(C_{11} + C_{12})\delta^2 + ... \tag{4.2.13}$$

If this can also be fitted by a quadratic form

$$E(\delta) = a + b\delta^2 \tag{4.2.14}$$

it follows then that

$$(C_{11} + C_{12}) = \frac{b}{V} \tag{4.2.15}$$

So, once C_{11} has already been determined, equation (4.2.15) can be used to find C_{12}.

A similar procedure is applied to determine C_{13}. In this case the strain tensor is

$$\epsilon = \begin{bmatrix} \delta & 0 & 0 \\ 0 & 0 & 0 \\ 0 & 0 & \delta \end{bmatrix} \tag{4.2.16}$$

A quadratic form fit to the elastic energy leads to

$$(\frac{1}{2}C_{11} + \frac{1}{2}C_{33} + C_{13}) = \frac{b}{V} \tag{4.2.17}$$

where b is the coefficient of the quadratic term, from which C_{13} can be determined.

To determine C_{23}, the relevant strain tensor is

$$\epsilon = \begin{bmatrix} 0 & 0 & 0 \\ 0 & \delta & 0 \\ 0 & 0 & \delta \end{bmatrix} \tag{4.2.18}$$

Again, fitting a quadratic form to the strain energy leads to

$$(\frac{1}{2}C_{22} + \frac{1}{2}C_{33} + C_{23}) = \frac{b}{V} \tag{4.2.19}$$

4.2.3 Modelling the system

The system of interest in our investigations is a POPC lipid bilayer. We have considered three systems of POPC bilayers which were built using the VMD package [34]. The first one (System 1) had a surface area of 50 × 50 Å^2 with a total of 7906 lipid atoms in the MD cell. In the second system (System 2), one upper leaflet at the center of the system was removed leaving the MD cell with 7772 lipid atoms. In the final system (System 3), one whole lipid (upper and lower leaflets) was removed leaving just 7638 lipid atoms in the cell. All three systems were solvated in a box of water with 6388 water molecules as shown in the Figures 4.1, 4.2, and 4.3. The CHARMM36 [55] force fields were used to calculate the energies of the system.

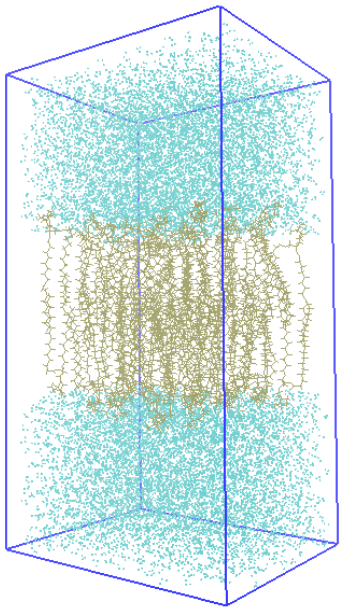

Figure 4.1: The lipids bilayer POPC in water.

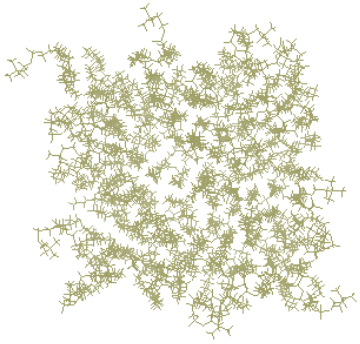

Figure 4.2: The lipid bilayer POPC with one upper leaflet removed. The water molecules have not been shown to give a better view of the lipid bilayer.

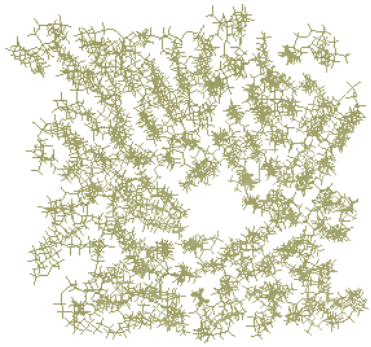

Figure 4.3: The lipids bilayer POPC after removing one whole leaflet (upper and lower). The water molecules have not been shown to give a better view of the lipid bilayer.

4.2.4 Computational Methods

MD simulations using NAMD [30] were performed using three-dimensional periodic boundary conditions. The systems were first minimized in energy for 5000 steps to avoid clashes between atoms. This energy minimized configuration was then used as the initial configuration in the subsequent simulations. The energy of this cell was taken to be the unstrained energy of the system. After that, the systems were equilibrated at 300 K, using Langevin dynamics to control the temperature. The Langevin damping coefficient was taken to be 1 ps^{-1}, and the simulations were run for 50 ns with a 2 fs time step. The system was treated as an isothermal-isobaric (NPT) ensemble at a pressure of 1 bar using the modified Nose-Hoover method. The van der Waals and Coulomb interactions were cut-off at 12 Å and the Particle Mesh Ewald (PME) method with a grid point density of $1.2/Å^3$ was used for counting the long-range Coulomb interactions [56].

After equilibration of 50 ns, the energy was minimized again following which the MD cell was subject to deformations with different strains. The systems were re-scaled along the different lateral (x,y) and normal (z) directions using the Lagrangian strain tensors. Subsequent changes in the box sizes were monitored. With the temperature fixed at 300 K, the energy was calculated after just 1 MD step to ensure that the system was still under the original strain. From this, the energy of the lipid assembly was determined.

Once the calculations had been carried out for different strains and for varying strain magnitudes, the results were plotted to give the final energy-strain relations. From these, the elastic constants (second-order derivatives) were calculated from a polynomial fit for the elastic energy at constant temperature. In general, the lipid bilayer has anisotropic elastic behavior due to different nature of interactions which appear along the different axes. However, elastically, it is expected to be laterally isotropic.

4.3 Results and discussion

After the systems were minimized in energy, the systems were deformed by applying different strains to the unit cells and coordinates to obtain second order elastic constants in the manner described above.

The effect of applying a strain on the bilayer is best seen by examining the structural changes to just one of the molecules making up the bilyer. Figure 4.4 shows how the partial stretching of a molecular chain under a strain applied along the z-axis (ie in the normal direction). These structural changes result in the elastic strain energy.

The variation of the elastic energy with strain parameter δ for the strain tensor

$$\begin{bmatrix} \varepsilon_{11} & \varepsilon_{12} & \varepsilon_{13} \\ \varepsilon_{21} & \varepsilon_{22} & \varepsilon_{23} \\ \varepsilon_{31} & \varepsilon_{32} & \varepsilon_{33} \end{bmatrix} = \begin{bmatrix} \delta & 0 & 0 \\ 0 & 0 & 0 \\ 0 & 0 & 0 \end{bmatrix} \tag{4.3.1}$$

is shown in Figures 4.5 (a). In this case, the only non-zero strain element was the ε_{11} term. These calculations were repeated for ε_{ij} for $i, j = 1,\ 2,\ 3$ and the ensuing results are shown in Table 4.1. As can be seen from these figures, the variation of the elastic energy appears to be quadratic in form and so may be fitted accordingly. The coefficient of the quadratic term is then used to calculate the elastic constants of the lipid bilayer membrane POPC.

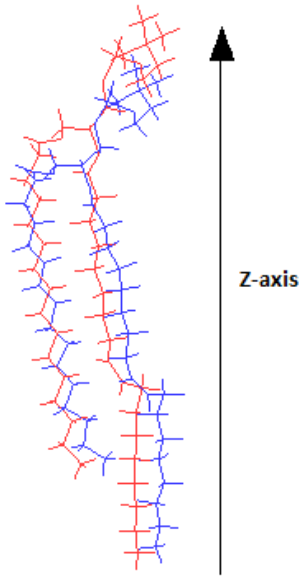

Figure 4.4: An example of the POPC leaflet without (blue) and with (red) applying strain to the z-axis.

Table 4.1: Anisotropic elastic constants of POPC lipid bilayer membrane in units of GPa.

Elastic constants C_{ij}	System 1	System 2	System 3
C_{11}	6.80	8.01	7.82
C_{12}	1.50	0.75	1.33
C_{13}	2.03	1.56	1.53
C_{22}	7.13	8.34	8.11
C_{23}	1.70	1.80	1.81
C_{33}	13.2	13.83	13.67

The final results for the elastic constants are given in Table 4.1 for the three systems considered. We note first that although C_{11} and C_{22} ought to be the same, due to symmetry, C_{22} is consistently larger than C_{11} by about 4%. This slight difference is a consequence of the way in which the molecule was set up. We also note that C_{33} is almost twice as large as C_{11}. C_{33} is a measure of the stiffness in the vertical direction and points to the resistance of the head and tail molecules to compressive stress. So, it is easier to squash the molecules making up the bilayer membrane in the lateral direction than in the vertical direction. Interestingly, when a molecule or a pair of molecules is removed (creating a defect), the lateral elastic constant is actually increased. A detailed examination of the energy contributions suggest that this is due to the electrostatic interactions between molecules.

The bulk modulus, K of a system with tetragonal symmetry can be expressed in terms of the elastic constants as

$$K = \frac{C_{33}(C_{11} + C_{12}) - 2C_{13}^2}{C_{11} + C_{12} + 2C_{33} - 4C_{13}} \tag{4.3.2}$$

Substituting the values for the elastic constants gives $K = 3.3$ GPa. The volume compressbility of lipid material as measured by Halstenberg *et al* [57] was found to be $\approx 5 \times 10^{-11}$ cm^2/dyne which corresponds to the volume stretching-compression elastic modulus of 2 GPa. The positional average of the bulk stretching-compression modulus was also investigated by Campelo *et al* [45] and found to be 4 GPa. All of these results suggest that our value of the bulk modulus is of the right order. In addition, these results are consistent with the values of bulk moduli for the lipids in general which Liu *et al* [58] found to be in the range of 10^9 Pa experimentally found for different temperatures. According to Pieffet *et al* [59] the higher values of the bulk modulus in computer simulations is consistent with the fact that these are performed with a more polar solvent than is done in experiments.

Table 4.2: A comparison of the calculated and experimentally determined bulk and shear moduli of a POPC lipid bilayer membrane in units of GPa.

	Bulk modulus K	Shear Modulus μ
This work	3.30	2.6
Pontes2013	2.6 - 4.1	
Halstenberg1998	2.03	
Campelo2008	4.0	

The tetragonal shear modulus can be represented by C_t which is equal to $(C_{11} - C_{12})/2$ and gives us 2.65, 3.63, and 3.245 GPa for the three systems respectively. However, these values are very high which suggest that lipid bilayer is much more rigid than expected. The results in general are consistent with experimental data. For example, Pontes *et al* [60] found that the bending modulus K for all major cell types was in the range 2.6 to 4.1 GPa.

4.4 Conclusion

There has been some interest in incorporating lipid bilayers in device applications like nano-sensors. In these scenarios, it is important to have a knowledge of the dynamic ability of cells to change their shape. This is in turn influenced by the elastic properties of these bilayers. In order to fully describe the diffusion processes detailed in the next two chapters, it is important that the elastic properties of lipid bilayer membranes are well reproduced.

Molecular dynamics simulations have been performed in order to find the elastic constants for the POPC lipid bilayer. The homogenous deformation method has been applied to a model bilayer system in order to understand the mechanical stability of the POPC lipid bilayer membrane. CHARMM36 force fields have been used to calculate the energies. The results reported here for bulk moduli of lipid bilayers are very similar to those reported by other workers. Further investigations need to carried out to understand how

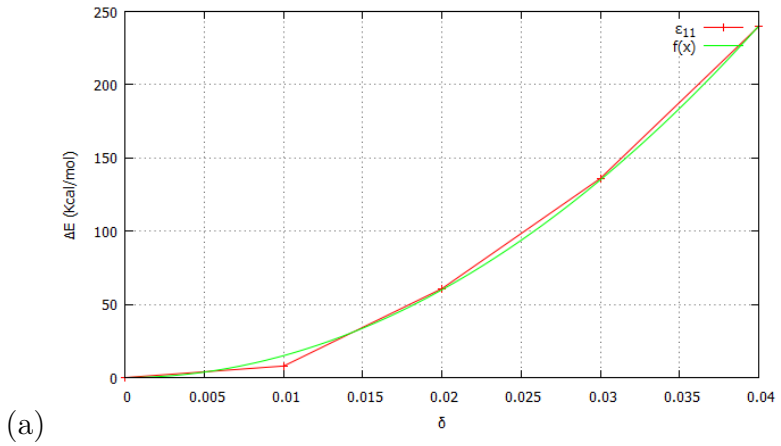

(a)

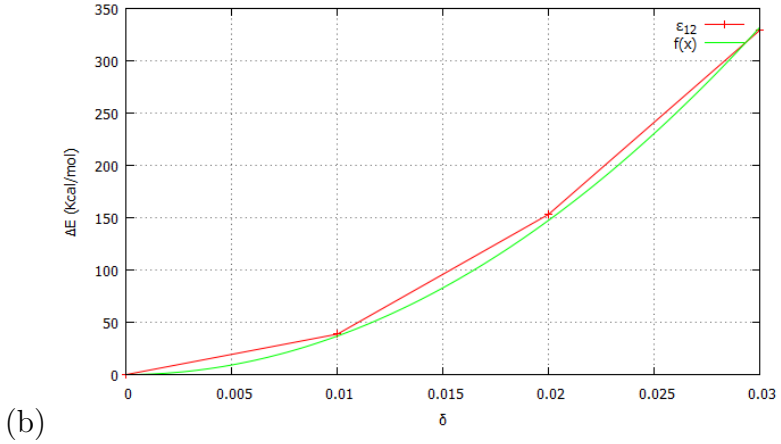

(b)

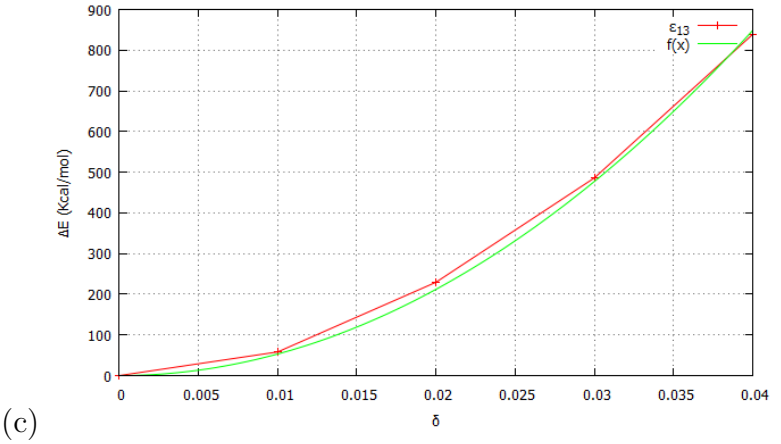

(c)

Figure 4.5: The strain-energy ($\Delta E = E - E_o$) as a function of applied strain at 300 K for system 1. The red dots are the data and the green line is a fitting parameter.

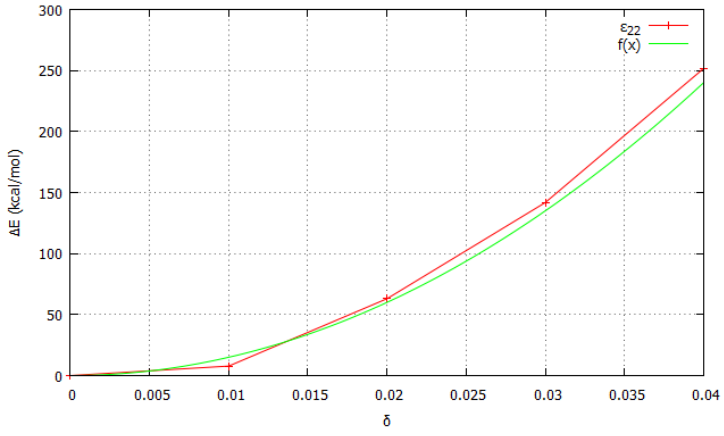

(e)

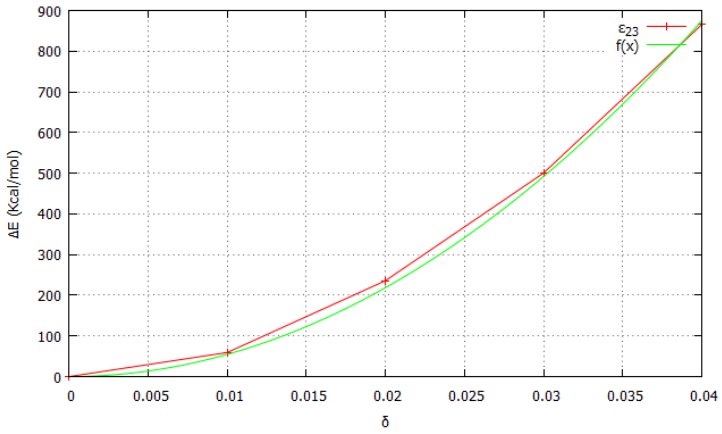

(f)

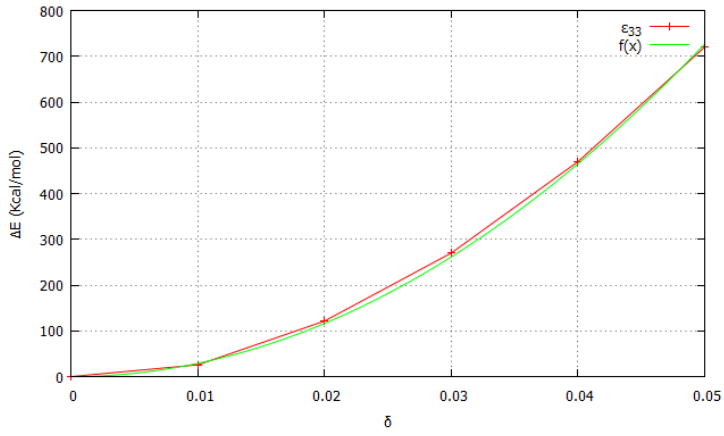

(g)

Figure 4.6: The strain-energy ($\Delta E = E - E_o$) as a function of applied strain at 300 K for system 1. The red dots are the data and the green line is the fitting parameter.

the elastic properties change on increasing the temperature of the system. Defects, in the form of missing upper and/or lower leaflet molecules appear to affect the elastic properties greatly.

Chapter 5

Computer simulations of the diffusion of water molecules and ions across POPC lipid bilayer membranes

5.1 Introduction

Cellular membranes form a separation between the extracellular space and the intracellular fluid that is mostly impermeable. Lipid bilayers, which represent the core of all biological membranes, are self-assembled structures composed of amphiphilic lipids and water. Lipid bilayer membranes form a barrier to proteins, molecules and many ions dissolved on either side of the membrane. In previous studies, Matthai *et al* investigated the transportation of biopolymers through channels, made up of hemolysin pores embedded in a lipid bilayer membrane [10, 11].

It is well known that ions like K^+, Cl^-, and Na^+ can and do permeate across the membrane. Although this selectivity in permeability is primarily based on size, other

factors can influence the diffusion of ions across a membrane.

In any computer simulation study, the choice of interatomic force fields is of paramount importance. Over the years, there have been many attempts at deriving force fields that reproduce the structure and charge distributions of small molecules as calculated using *ab initio* quantum mechanical techniques. While none of these can hope to describe all the chemical processes accurately, the goal has been for force fields that are accurate enough but which can also be used for large scale simulations, both from the point of size and time [61, 62]. In modelling the diffusion of atoms, ions or molecules across biological membranes it is therefore important to utilise force fields that reproduce the experimentally determined diffusion coefficients.

There have been numerous studies aimed at estimating the value of the self-diffusion coefficient, $D_S(H_20)$, of water [63–66]. For example, Mills [67] using a tracer method and Holz *et al* [67, 68], using the pulsed magnetic field gradient (PFG) NMR both found an average value of $D_S(H_20)$ to be about 2.2×10^{-5} cm^2/s. Computational studies, involving methods such as MD simulations, have also been carried out by numerous workers. Mark and Nilsson [69] used the TIP3P force field model to carry out simulations on water at 298 K for 100 ps. Then, using different time trajectories they found the average value of the diffusion coefficient to be $D_{SD}(H_20) = 5.60 \pm 0.08 \times 10^{-5}$ cm^2/s. While this is larger than that found experimentally, it is in agreement with the results obtained from other computer simulation studies. Yeh and Hummer [70] also carried out computational investigations of the diffusion coefficient of water using the TIP3P model and found this to be 6.05×10^{-5} cm^2/s. Other force field models have also been used in this context. The SPC model was used by Postma [71] who determined the value of $D_S(H_20)$ to be 7.5×10^{-5}cm^2/s at 350 K.

The diffusion coefficient of water is greatly affected by the surrounding medium and in particular, when water is in the neighbourhood of a membrane or other large molecular systems. So, for example, López Cascales *et al.* [72] ran MD simulations on a charged

biological membrane surrounded by water and measured the translational diffusion coefficient of water molecules in the bulk water region, but parallel to the membrane. They found $D_S(H_20)$ to be greater than 8×10^{-5} cm^2/s. This is similar to the values obtained by Postma [71] using the SPC model.

It must be stressed that the values obtained for the self diffusion coefficient of water in computer simulations are very much dependent on the force field model used to describe the water-water interactions and it is now recognised that the TIP3P model generally gives larger values for $D_S(H_20)$ than is found experimentally. However, in spite of these inconsistencies, the TIP3P model is agreed to give a good description of the interaction of water with lipid membranes and so, in simulations involving water and biological membranes, it is often taken to be the force field model of choice.

There have also been many studies aimed at understanding the processes involving the diffusion of ions across lipid bilayer membranes. Hardy *et al* [73] carried out MD simulations of the diffusion of ions across a POPC lipid membrane POPC immersed in a NaCl solution. Gurtovenko and Vattulainen [74] demonstrated the importance of asymmetry by performing MD simulations of asymmetric lipid membranes comprised of zwitterionic (phosphatidylcholine (PC) or phosphatidylethanolamine (PE)) and anionic (phosphatidylserine (PS)) leaflets. They showed that the asymmetry in trans-membrane distribution of anionic lipids gave rise to a non-zero potential difference between the two sides of the membrane. This was a consequence of the difference in charges on the two leaflets.

It has also been suggested [75] that an imbalance of ions on either side of a lipid bilayer system could result in the creation of a water pore which in turn allowed for the passage of ions across the membrane until the charge equilibrium was established. In their investigations, Gurtovenko and Vattulainen [75] constructed a system which consisted of two DMPC lipid bilayers in a simulation box, with periodic boundary conditions and separated by water molecules. NaCl was then added to the two water phases by fixing

the number of 20 Cl ions in both water reservoirs but added extra Na between two bilayers with respect to the reservoirs. This meant the water reservoirs (between two bilayers) had a higher concentration of cations than the outer regions of the bilayers.

Other researchers have also shown that the imbalance of ions in the lipid bilayer system could result in the creation of a water pore which then allowed for the passage of ions through that pore. The ions move across to neutralize and reduce the electrostatic potential. In their MD simulations on a POPC lipid membrane surrounded by NaCl in water, Hardy *et al* [73] introduced different ions on either side of the membrane and used semi-periodic boundary conditions. This resulted in an electric field of 0.7 V/nm being produced across the membrane which then allowed ions to diffuse through the pore and across the membrane.

In this thesis, we report on investigations carried out to further our understanding of how the ion imbalance and the resulting electrochemical gradient across the bilayer affects the diffusion of water molecules and Na^+ and Cl^- ions. To this end we have concentrated on using well tried and tested force fields which can be used reliably in simulating biological molecules in aqueous solution. We have determined the diffusion coefficients of the different particles inside and around the membrane both with and without the presence of an electrochemical gradient.

In the next section we describe the systems constructed to model the diffusion of ions and water molecules across the POPC membranes. In Section 5.2, we give a description of the computational methodology and the methods employed in the analysis of the data resulting from the simulations. In the two sections following, we report on the results of simulations on lipid bilayer membranes between aqueous solutions which are either the same or different on each side of the membrane. Finally, we conclude by comparing our results with those of other investigators and highlight the significant results of this study.

5.2 Modelling the diffusion across the lipid bilayer membrane

The lipid bilayer considered in this chapter again was the POPC bilayer (see chapter 2 section 2.2.1). Like all lipid bilayers, the POPC bilayer comprises 2 leaflets, each in turn made up of a number of phospholipid molecules. The phospholipid molecule has a hydrophillic headgroup and a hydophobic tailgroup. Because of this, the heads of the molecule prefers to be in an aqueous environment while the tails are more stable in a lipid environment. This then leads to the natural formation of bilayers in which the headgroups point outwards into the water while the tailgroups point towards each other. When placed in water these bilayers tend to form spherical shapes with water inside and outside (Figure 5.1).

5.2.1 Systems

In order to simulate the flow of ions and water molecules across the membrane from the cytoplasm to the extracellular fluid, we modelled the system to be a lipid bilayer between two fluids, as shown in Figure 5.1.

In carrying out molecular dynamics simulations, it is efficacious to employ periodic boundary conditions, especially when performing the analysis of the electrostatic potential in the simulation cell. With such periodic boundary conditions, two different types of arrangements of the cell membrane between the cytoplasm and the extracellular fluid were configured. In the first arrangement, it is assumed that both fluids have the same constituents. In such a scenario, it is sufficient to model the system according to the simulation cell (labeled configuration I) as shown in Figure 5.2a with one bilayer surrounded by water molecules. When considering different fluids across the membrane boundary, and still maintaining periodic boundary conditions, a two boundary arrangement (labeled configuration II) as shown in Figure 5.2b is necessary.

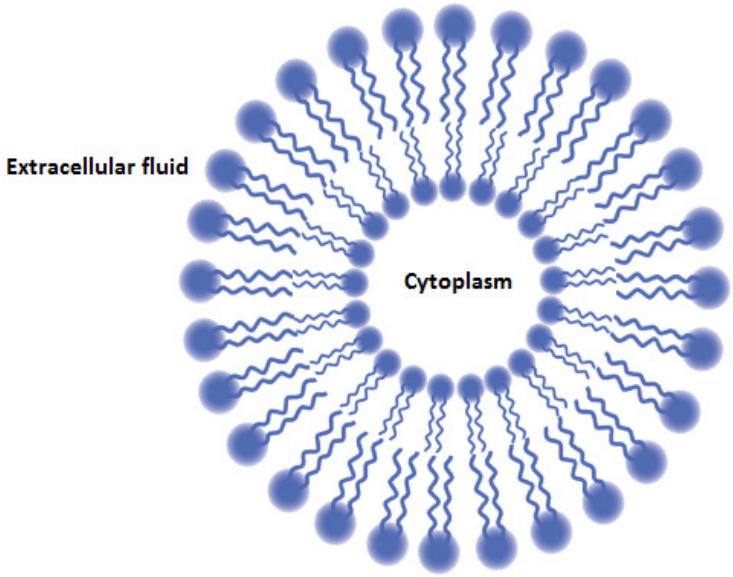

Figure 5.1: Cell structure showing the cellular membrane enclosing the cytoplasm. The extracellular fluid is on the outside of the membrane.

In each of these configurations, variations of the fluid constituents were considered. In all, five different systems were investigated. System A was configured with the intention of investigating the diffusion of single Na and Cl ions across a membrane surrounded by water. So for this system, the fluids on either side of the membrane were taken to be just water. System B was evolved from System A by adding NaCl to the water, making a weak saline solution, ie water with an equal number of Na and Cl ions. System C was configured to examine the effect of having unequal numbers of sodium and chlorine ions, thus making it a charged fluid. The final two systems (System D and System E) were constructed to order to investigate the scenario where there are different fluids on either side of the membrane. The details of these systems are given in Table 5.1.

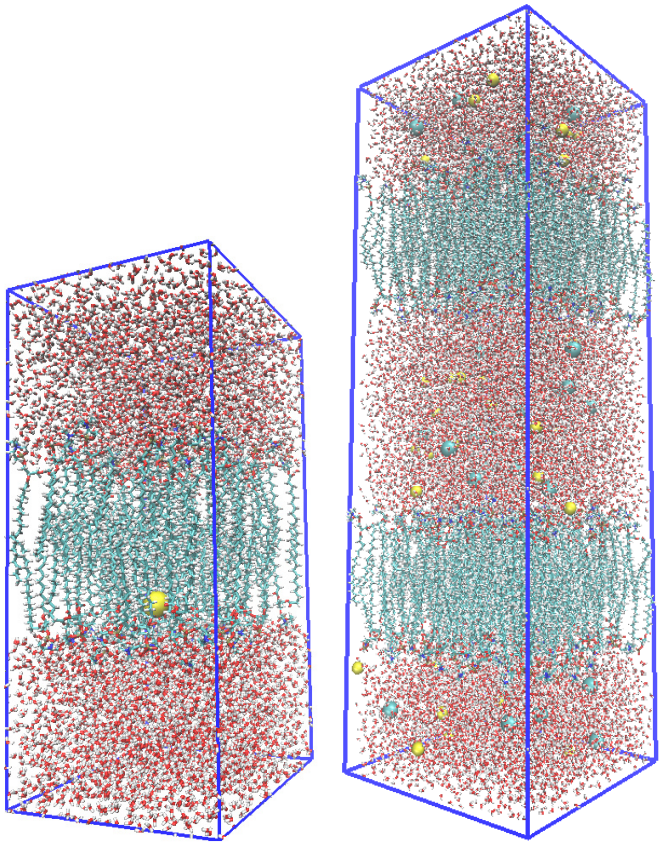

(a) Configuration I (b) Configuration II

Figure 5.2: Configurations used to model a lipid bilayer membrane between two fluids. The lipids forming the membrane, shown as chain molecules, are surrounded by water molecules (red), Na ions (yellow) and Cl ions (cyan).

5.3 Computational methodology and analysis

5.3.1 Molecular dynamics simulations

In order to determine the diffusion coefficients of the ions and the water molecules across the lipid bilayer, systems comprising either a lipid single bilayer membrane or a double bilayer as shown in Fig 5.2 surrounded by water molecules and including a few of the relevant ions of interest were set up. All the atoms and molecules were confined to a three-dimensional periodically repeating molecular dynamics simulation box as shown in

Table 5.1: Details of systems investigated by molecular dynamics

System label	Configuration type	Size Å^3	Number of molecules	Fluid 1	Fluid 2
A	I	$50 \times 50 \times 110$	59 lipids + 6388 H_2O	H_2O + Na^+ (or Cl^-) ion	
B	I	$72 \times 72 \times 120$	136 lipids + 10836 H_2O	H_2O + 20 Na^+ + 20 Cl^-	
C	I	$72 \times 72 \times 120$	136 lipids + 10836 H_2O	H_2O + 15 Na^+ + 25 Cl^-	
D	II	$72 \times 72 \times 200$	272 lipids + 18211 H_2O	H_2O + 19 Na^+ + 21 Cl^-	H_2O + 18 Na^+ + 17 Cl^-
E	II	$72 \times 72 \times 200$	272 lipids + 18211 H_2O	H_2O + 50 Na^+	H_2O + 50 Cl^-

Figure 5.2. The simulation box was taken to have tetragonal symmetry with dimensions as given in Table 5.1.

The lipid bilayers and the surrounding water molecules were built by using the Visual Molecular Dynamics (VMD) package [34]. All the molecular dynamics simulations were carried out using the NAMD 2.10 package [30].

The systems were kept in an isothermal-isobaric (NPT) ensemble at a pressure of 1 bar using a modified Nose-Hoover method. The van der Waals and Coulomb interactions were cut-off at 12 Å and the Particle Mesh Ewald (PME) method was used to carry out the calculations of the long-range Coulomb interactions with a grid point density of 1.2/Å^3. The interatomic forces between the atoms in the lipids and the water molecules were taken to be that described by the CHARMM36 [55] force fields and the water TIP3P force field model [69]. In the case of the latter, partial negative charges were placed on the oxygen atoms and positive charges on the hydrogen atoms. For the interactions of the sodium and chlorine ions with water and with the lipid atoms, the Lennard-Jones parameters, where the symbols have their usual meaning, used in the CHARMM36 force fields are given in Table 5.2.

Table 5.2: Lennard Jones parameters for the ions in CHARMM36 and used in this study.

Ions	ϵ (kcal/mol)	$R_{min}/2$ (Å)
Na^+	0.0469	1.36375
Cl^-	0.150	2.27

In each simulation study, the systems considered were first allowed to reach their minimum energy configuration. This was done by carrying out a MD run for at least 5000 time steps, each of 2 fs. Subsequently, using Langevin dynamics, the systems were allowed to reach a dynamical equilibrium configuration at 300 K. A Langevin damping coefficient of 1 ps^{-1} was used to control the temperature. This part of the simulation was allowed to run for between 50 to 65 ns and the resulting time averaged configurations were subject to analysis.

5.3.2 Area per lipid and bilayer thickness

Because of its high sensitivity to the hydrophilic attraction between headgroups and the hydrophobic repulsion between non-polar hydrocarbon tails, the area per lipid (APL) of a bilayer provides much important information about a bilayer or a membrane. In addition, the interaction of the headgroups molecules with the surrounding water or aqueous solution has an effect on the APL. An accurate determination of the APL is desirable as this implies that the 2-D density in the bilayer plane is correctly described. This is essential in having confidence that the simulation correctly predicts other structural properties, such as the lipid tail order parameters, the bilayer thickness (BLT), the electron density profiles, as well as the overall phase behavior of the membrane. In addition to the APL, the bilayer thickness is another important quantity which points to the robustness of the simulations.

Both these quantities have been measured both experimentally and determined by computational methods for different types of lipid bilayer membranes. X-ray measurements of the thickness of the POPC membrane has been reported to be approximately

37.0 Å. The experimental values of the area per lipid have been found to vary quite considerably. For POPC, values between 54 Å to 68 Å^2 have been reported [76]. The computationally determined values are, of course dependent on the choice of force fields. Klauda *et al* [32] has reported the area per lipid of the POPC using CHARMM36 to be 64.7 Å^2. In all our simulations, the BLT values for the POPC bilayers were found to be approximately 38.5 Å. This is in general agreement with the experimental values.

It is important to note that these quantities are also dependent on the fluids surrounding the membrane. Thus, increasing the NaCl concentration in the fluids results in an increase in the bilayer thickness. Correspondingly, the area per lipid decreases. These variations may be attributed to charge transfer effects and to atomic displacements in the bilayer.

In the event of pore formation in the membrane, the APL has been reported to show a sharp increase in its value and there is a corresponding decrease in the lipid thickness in the region of the pore. This comes about as a consequence of the redistribution of the headgroup molecules towards the pore interior. By comparing the computational values with experimental results, it is therefore possible to confirm the reliability of the results of simulations.

5.3.3 Calculation of the diffusion coefficients

The diffusion coefficient, D, is a measure of the speed of the translational motion of particles through a particular medium and is one of the many dynamic properties of a molecule in solution. It depends not only on the size and shape of the molecule and its interaction with the surrounding medium, but also on the temperature of the system. The diffusion coefficient can be determined from molecular dynamics simulations by analysing the molecular (or atomic) trajectories as a function of time. It is assumed that these particles undergo Brownian motion which is a stochastic process reflecting the motion of particles due to thermal collisions with the solvent molecules [77]. The diffusion

coefficient is related to the time averaged mean square displacement of a particle moving in d dimensions through the equation

$$D = \lim_{t\to\infty} \frac{1}{2dt} \left\langle (\mathbf{r}(0) - \mathbf{r}(t))^2 \right\rangle \tag{5.3.1}$$

where $\mathbf{r}(t)$ is the position of the molecule at time t. The term in the angular brackets in the above equation is often referred to as the mean square displacement (MSD). Although for very short times the MSD fluctuates with time in a non-linear fashion, over longer times there is a linear relationship from which D can be determined. Hence, D is given by the slope of a plot of the MSD against time divided by twice the system dimension (e.g 2 for linear, 4 for lateral and 6 for bulk diffusion). In our calculations of the MSD of the ions and water molecules, we have used a 1 ns time-window with positions tabulated every 0.004 ns.

5.3.4 The electrostatic potential across the membrane

An important quantity that determines the viability of molecular diffusion across a membrane is the electrostatic potential, $\phi(z)$ across the lipid bilayer, where z is the coordinate perpendicular to the membrane surface. The electrostatic potential is obtained by numerically solving Poisson's equation,

$$\nabla^2\phi(\mathbf{r}) = -\frac{1}{\varepsilon}\sum_i \rho_i(\mathbf{r}) \tag{5.3.2}$$

where the charge density around every ion in the system is approximated by a spherical Gaussian charge distribution as

$$\rho_i(\mathbf{r}) = q_i \left(\frac{\beta}{\sqrt{\pi}}\right)^3 e^{-\beta^2|\mathbf{r}-\mathbf{r}_i|^2} \tag{5.3.3}$$

These charges are obtained directly from NAMD simulations.

In our simulations studies, VMD was used to calculate the mean electrostatic potential from the grid points. This approach requires the use of a periodic cell and the reciprocal sum of the smooth particle mesh Ewald method (PME) generating a smoothed electrostatic potential grid controlled by the Ewald factor is evaluated. From the above equations, the mean electrostatic potential is found by averaging the instantaneous electrostatic potential $\phi(r)$ over the entire trajectory of the MD simulations. The potential across the membrane is then obtained by taking an average over the membrane surface $(x - y)$ plane.

5.4 Simulations of single Na^+ and Cl^- ion interactions with a membrane surrounded by water

In order to investigate the interaction of single ions with the membrane and the possible diffusion of Na^+ and Cl^- ions across a lipid bilayer membrane, a POPC membrane comprising 59 lipid molecules, with 29 in the upper leaflet and 30 in the lower leaflet, was constructed and placed in the middle of the simulation box. Above and below the membrane, 19161 water molecules were randomly sited, as shown in Figure 5.2a. Then, a single Na^+ (or Cl^-) ion was positioned at different sites inside and just outside the membrane layer (Figure 5.2a). For each of these ion starting positions, the simulation was allowed to run at 300 K and the trajectory of the ion monitored.

When a Na^+ ion was placed in the hydrophobic region (just below the headgroups) of the lipid bilayer POPC membrane, it took just under 4 ns before it moved out of the membrane and a further 4 ns before it moved into the bulk water region of the assembly. The diffusion coefficient of the ion in the three regions; inside the membrane, at the membrane surface and in the bulk water, was determined from the MSD plots (for example Figure 5.3) and the results are shown in Table 5.3. The low diffusion coefficient of the ion whilst inside the membrane is indicative of the weak local binding of the ion

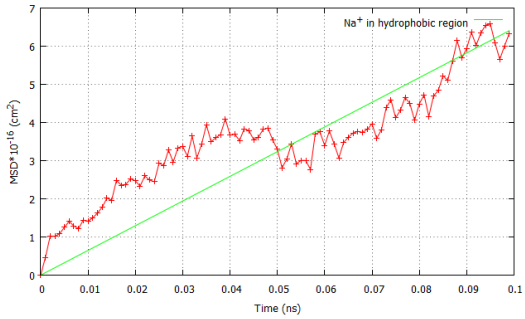

(a) In hydrophobic region

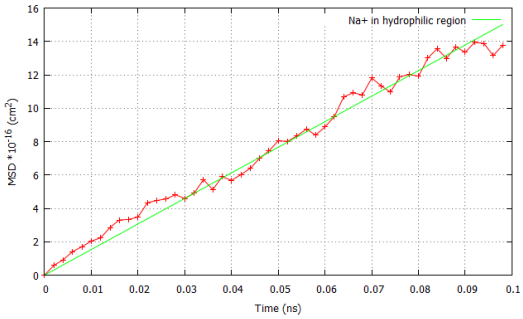

(b) In hydrophilic region

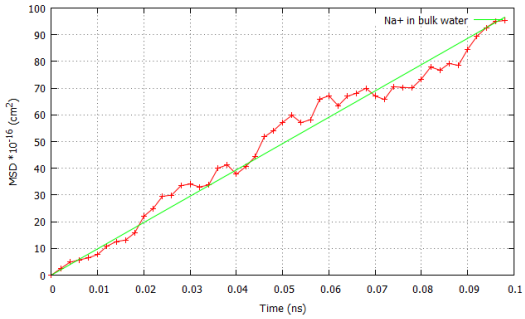

(c) In bulk water region

Figure 5.3: Representation of MSD for Na ion in System A at different regions in the simulation box.

with the surrounding atoms of the lipid molecules. As the simulation proceeds, entropy effects soon overcome this weak binding and the ion is released and diffuses out of the membrane surface into the surrounding water.

When the ion is in the surface region of the bilayer membrane, it diffuses much more rapidly which is consistent with a smaller interaction energy between the ion and the bilayer surface. When the ion finally moves into the bulk region of the water, the diffusion coefficient of the Na^+ ion is similar to its value in water with no membrane present. This value of the diffusion coefficient is in reasonably good agreement with experimental finding of 1.33 $\times 10^{-5}$ cm^2/s [78].

As mentioned above, the equilibrium values of the APL and membrane thickness give a measure of the confidence in the simulations. In the simulations with a single

Table 5.3: Diffusion coefficients, D ($\times 10^{-5}$ cm^2/s), of Na^+ and Cl^- ions at different positions in the simulation box for System A. Also shown is the diffusion coefficient for a water molecule.

position in simulation box	$D(Na^+)$	$D(Cl^-)$	$D(H_2O)$
in lipid hydrophobic region	0.1	1.4	2.9
on top of lipid hydrophilic region	0.3	1.8	4.9
in bulk water region	1.6	2.2	5.3

Na^+ added to the system, the APL was found to be 79 ± 3 Å^2 which is larger than the experimentally observed value for this system. The BLT was found to be 32Å which in turn is slightly smaller than the experimental value for the POPC bilayer. These deviations from experimental values suggest that the system may not have become fully equilibrated or that the system was not large enough.

When a Cl^- ion was similarly placed at specific positions in the hydrophobic region (just below the headgroups) in the lipid bilayer POPC membrane, the ion immediately moves out of the lipid, carrying out a random walk around the lipid membrane surface before moving into the bulk water region. The diffusion coefficient from MSD plots (for example Figure 5.4), both at the surface of the lipid bilayer and in the bulk water region are close the the experimentally observed value of 2.03 $\times 10^{-5}$ cm^2/s [79].

For completeness, a set of simulations were carried out with a single water molecule placed inside the membrane instead of an ion. Interestingly, the diffusion characteristics of the water molecule including the diffusion trajectories and the diffusion coefficients were found to be very similar to that found for the Na^+ ion.

From these simulations, it is clear that while there is a tendency for a Na ion to be partially bound inside but near to the bilayer surface, it is easily displaced out of its binding site. On the other hand the Cl ion is not bound to any of the sites, at or below the bilayer surface Figure 5.5. This is consistent with calculated charge distributions on the bilayer surface atoms.

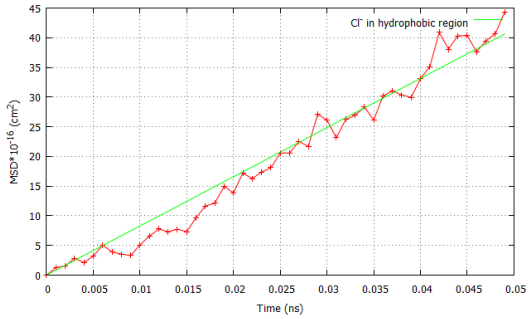

(a) In hydrophobic region

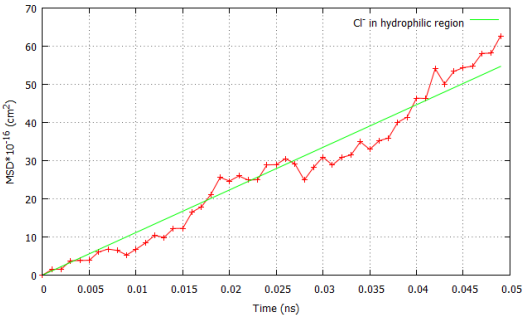

(b) In hydrophilic region

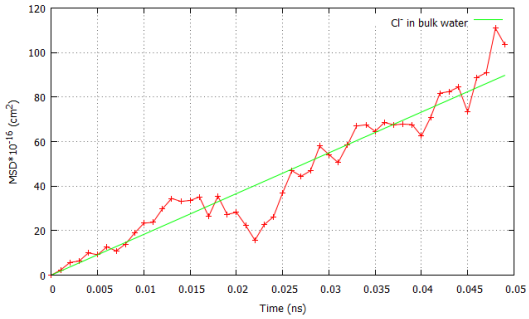

(c) In bulk water region

Figure 5.4: Figure showing the MSD for Cl ion in System A at different regions in the simulation box.

5.5 Simulations of single Na^+ and Cl^- ion interactions with a membrane immersed in an ionic solution

In order to investigate the effect of changing the fluid constitution surrounding the lipid bilayer membrane, the systems were modified by adding Na^+ and Cl^- ions to the water surrounds. Two sets of such simulations were carried out. In the first (System B), equal numbers (20) of Na^+ and Cl^- ions were introduced, while in the second set (System C), an imbalance in the ions (with 15 Na^+ and 25 Cl^- ions) was created to see how the non-neutrality of the fluid affected the ion-membrane interactions.

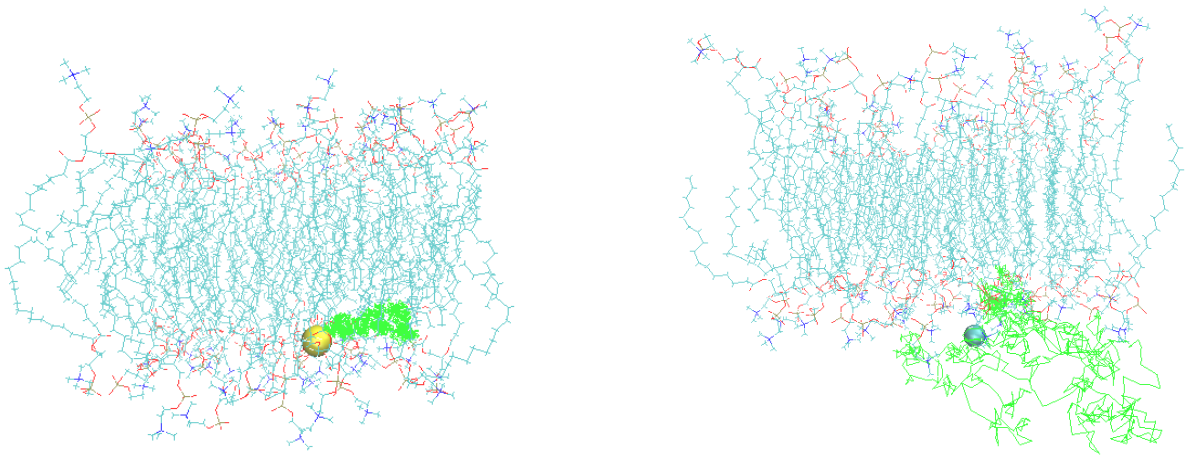

(a) left (b) right

Figure 5.5: Typical trajectories (in green) over 2 ns of Na (left) and Cl (right) ions in simulation System A.

The simulation details for these systems are given in Table 5.1. The size of the system (POPC lipids in a box of TIP3P water) was increased slightly so that the number of lipids in each of the upper and lower leaflets was increased to 36. This was to ensure that the APL and BLT of the membrane were in better agreement with the experimental values. This meant that there were a total of 18224 atoms in the membrane and 32508 atoms in the water in addition to the 40 ions randomly distributed in the water. The initial molecular configuration for System B is shown in Figure 5.6. Once again, the simulations were run for 50 ns over which the APL, the BLT and the diffusion coefficients of the specific ions were calculated.

5.5.1 APL and BLT

The BLT after equilibration for both systems were found to be just under 38 Å. This is good agreement with the experimental measurement of 37.0 Å found for POPC using X-ray scattering [76]. These researchers also found that the APL varied between 54 and 68.3 Å^2. The APL has also been determined computationally by many other researchers.

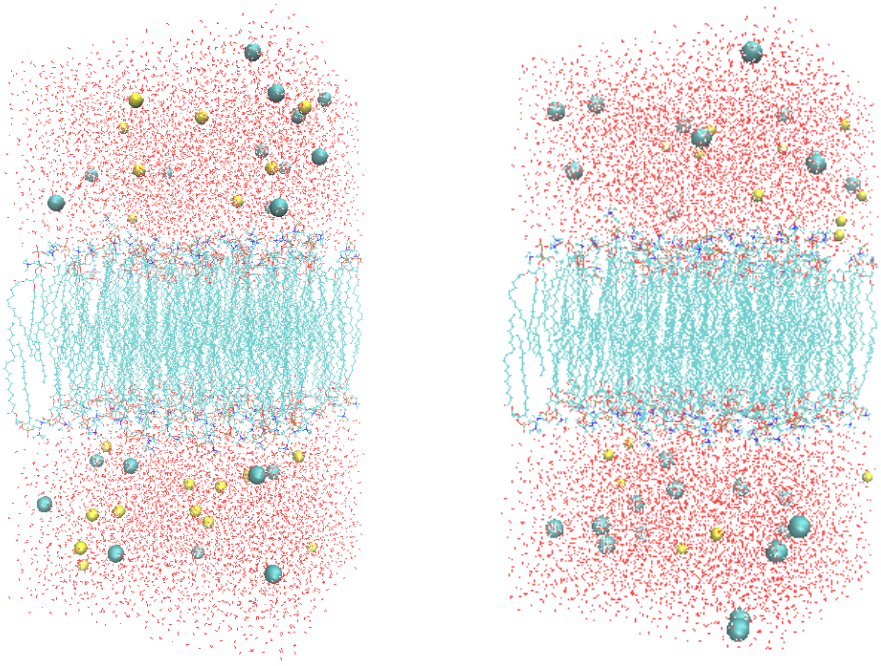

(a) Equal concentration (b) Different concentration

Figure 5.6: The simulation cell with a single POPC lipid bilayer surrounded by water containing Na^+ and Cl^- ions with (left) equal concentration and with (right) different concentration.

For example, MD simulations on POPC using CHARMM force fields was found to give an APL of 64.7 $Å^2$ [32]. Comer *et el* [80] investigated how the APL was affected by using different van der Waals cutoffs. They found that for cutoffs between 1 and 1.2 nm the APL was about 65 $Å^2$. It has also been observed that the APL depends on the number of Na and Cl ions in the simulation cell [81]. Interestingly, it was found that an increase in the NaCl concentration led to a decrease in the APL. In our simulations with a total of 40 Na and Cl ions, the APL was found to be $67.3 \pm 1.5 Å^2$. This value together with our results for the BLT indicates that both systems were of optimum size and had reached a full thermal equilibrium configuation after 50 ns.

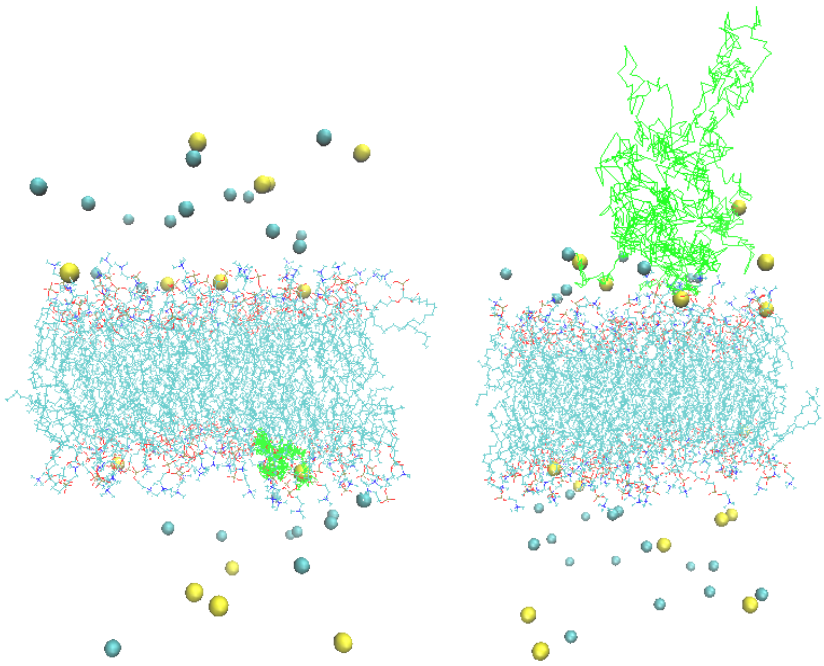

(a) Na ion (b) Cl ion

Figure 5.7: Typical trajectories (in green) over 10 ns of Na (a) and Cl (b) ions in simulation System B.

5.5.2 Ion diffusion coefficients and their spatial distribution

While all the ion trajectories show the particles undergoing Browninan motion in the bulk water region, a substantial fraction of Na ions get close to the lipid surface and tend to remain there for a periods of up to 10 ns. By contrast, the Cl ions tend not to adhere to the membrane surface and in general do not spend any substantial time close to the surface. These observations are similar to that reported by Miettinen *et al* [82], and Sachs *et al* [83]. Examples of typical trajectories for both Na and Cl ions in the simulation system B are shown in Figure 5.7.

The diffusion coefficients of the Na and Cl ions for both systems were computed from the MSD of the ion trajectories. While the ions in the bulk water region had similar diffusion coefficients to that given in Table 5.3, the Na ions at the surface region or inside

the membrane bilayer have much reduced values. In determining this, all the Na ions near or below the surface were sampled at different time intervals. All of these samplings gave results of $D(Na^+) \approx 0.1 \times 10^{-5}$ cm^2/s, for ions at or below the bilayer surface as shown in Table 5.4. Thus, it may be concluded that the NaCl aqueous solution has the effect of allowing the Na ions to penetrate more deeply and for longer periods inside the membrane. We have also monitored the ion density distribution across the simulation cell over the simulation period and the results for both System B and System C are shown in Figure 5.8. The shaded region in the figures depict the membrane bilayer with its edges at approximately -18 Å and 20 Å. This corresponds to a bilayer thickness of approximately 38 Å. It is interesting to note that for both systems, some Na ions are to be found inside the membrane while there is an absence Cl ions in this region. On integrating out the area under the curves, we find that for System B on average, 4 to 5 Na ions out of the total of 20 Na ions are to be found near or below the membrane surface. Similarly for System C, about 3 Na ions out of the 15 spend considerable time at or below the bilayer surface. So, for both systems, more than 20% of the Na ions are to be found near the bilayer surface. In contrast, for System B, there are no Cl ions at or below the membrane surface. For System C, which had a higher concentration of Cl ions, on average just one of these ions is found near the surface.

In order to explain this observation, we calculated the net charge distribution on the lipid bilayer membrane surface surrounded by water, but without the presence of any ions. The net surface charge distribution is shown in Figure 5.9. It is clear then, that the large areas of negative charge act as attractors for the Na ion while repelling the Cl ion. These have been identified as the carbonyl groups in the membrane. The binding of the Na ions to these carbonyl groups manifests itself in the very small diffusion coefficients for the Na ion.

Based on the diffusion coefficients, the ion trajectories and binding sites, it is clear that the introduction of ions into the aqueous surrounds has the effect of allowing the Na

Table 5.4: Diffusion coefficients, D ($\times 10^{-5}$ cm^2/s), of Na^+ and Cl^- ions at different times for system B and C.

Time (ns)	System	$D(Na^+)$	$D(Cl^-)$
10	B	(1) 0.089	-
	B	(2) 0.096	-
	B	(3) 0.0711	-
	B	(4) 0.100	-
	B	(5) 0.109	-
	C	(1) 0.098	-
	C	(2) 0.105	-
	C	(3) 0.359	-
20	B	(1)0.117	-
	B	(2)0.085	-
	B	(3)0.076	-
	C	(1)0.215	-
	C	(2)0.220	-
	C	(3)0.063	-
30	B	(1) 0.096	-
	B	(2) 0.105	-
	B	(3) 0.141	-
	B	(4) 0.098	-
	B	(5) 0.068	-
	C	(1) 0.172	(1) 1.86
	C	(2) 0.080	-
	C	(3) 0.093	-
40	B	(1) 0.108	-
	B	(2) 0.138	-
	B	(3) 0.072	-
	C	(1) 0.167	-
	C	(2) 0.434	-
50	B	(1) 0.1416	-
	B	(2) 0.177	-
	B	(3) 0.199	-
	C	(1) 0.123	-
	C	(2) 0.108	-
	C	(3) 0.151	-

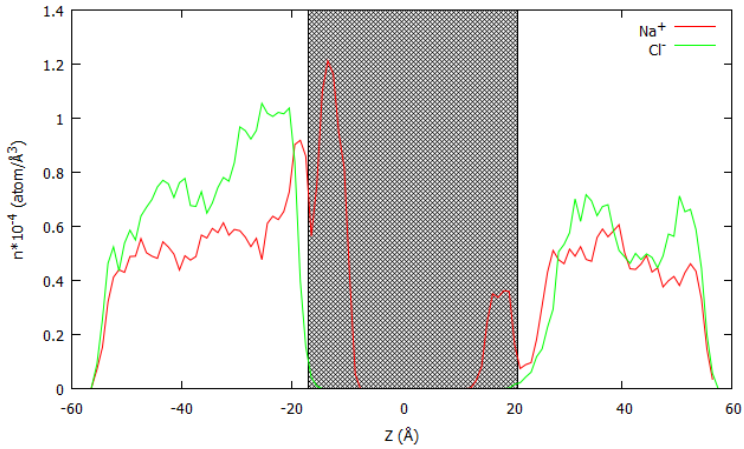

(a) System B

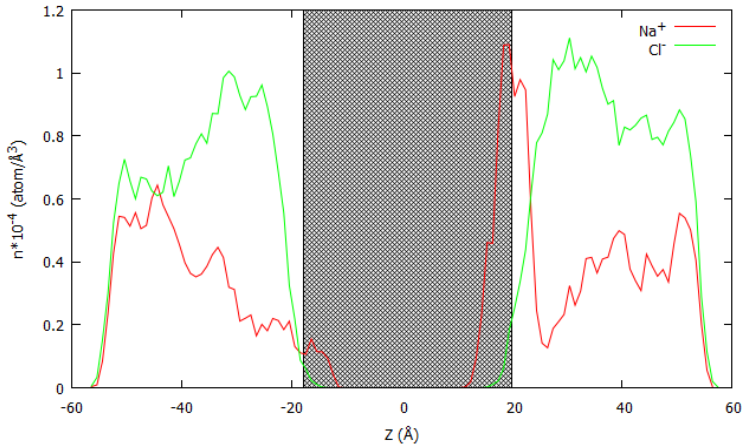

(b) System C

Figure 5.8: Time averaged over 50 ns density distribution of Na (red lines) and Cl (green lines) ions in simulation systems B (top) and C (bottom). The bilayer regions are indicated by the shaded areas.

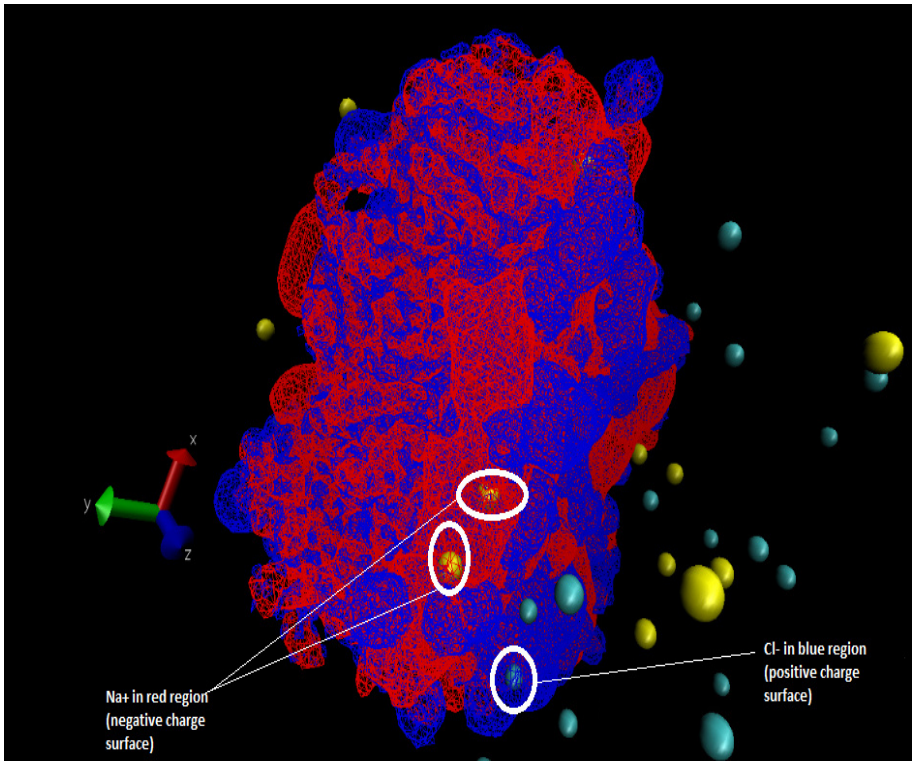

Figure 5.9: The net charge distribution on the lipid bilayer. The red areas are regions of negative net charge while blue is of net positive charge. Also shown are the positions of the Na and Cl ions.

ions to penetrate more deeply and remain inside the membrane for longer periods of time.

5.6 Diffusion of ions across a POPC lipid bilayer membrane with different fluids on either side

Having established that there is little or no likelihood of ion diffusion across a membrane when the fluids on either side of the membrane have the same constituents, following the work of Hardy *et al* [73] and Gurtovenko and Vattulainen [75], we then focused on investigating the effects of introducing an ion imbalance across the bilayer. This is, of course, akin to introducing an electrochemical gradient across the membrane.

In order to model a membrane with different fluids on either side while keeping periodic boundary conditions, it is necessary to introduce two bilayers in the simulation cell. Then, the region between the two bilayers corresponds to the cytoplasm inside the cell (Figure 5.1) while the fluid outside the two bilayers models the extracellular fluid. Each of the two POPC lipids bilayers, comprising 68 upper and 68 lower leaflets, making a total of 272 lipid molecules, were constructed and placed in the simulation cell (see Figure 5.2b). The bilayers were separated by 60 Å of water molecules and corresponds to Fluid 1 in Table 5.1. The thickness of the Fluid 2 region was taken to be same as that of Fluid 1 region. Na^+ and Cl^- ions were then introduced into both of the fluid regions.

It has been reported [73, 75] that the strength of the electrochemical gradient is a crucial parameter in allowing for ion diffusion across a bilayer. We have considered two extremes of this scenario. In the first, the charge imbalance was made to be small, with 19 Na^+ and 21 Cl^- ions in the inner region while having 18 Na^+ and 17 Cl^- in the outer fluid region. The net charge imbalance is therefore just a single electron charge. In the other scenario, in one fluid only Na^+ ions were introduced while in the other only Cl^- ions were positioned. We have labelled these two scenarios as System D and System E with the details of the computational cell given in Table 5.1.

MD simulations were then carried out on both systems with a view to investigating the circumstances under which ion diffusion takes place, particularly to determine the electrochemical field gradient required for ion diffusion leading to the neutralising of the inner and outer fluids.

5.6.1 Results of simulations of System D

As before, after the initial equilibration of the system, the simulations were run for a total of 50 ns. After 10 ns, a substantial fraction of the sodium ions were found to move close to the membrane surfaces from both sides of the membrane. However, no ion appears able to overcome the barrier to diffuse through the membrane. The MSD

Table 5.5: Diffusion coefficients, D ($\times 10^{-5}$ cm^2/s), of Na^+ and Cl^- ions averaged for System D.

	$D(Na^+)$	$D(Cl^-)$
1	0.101	1.8821
2	0.082	-
3	0.115	-
4	0.105	-
5	0.107	-
6	0.116	-

data was used to determine the ion diffusion coefficients at different times during the simulation. Whilst in the hydophillic headgroup region of the lipid bilayers, the diffusion coefficient of the Na ion, as determined from its trajectories, indicate that it is roughly the same as it was in the simulations of System B, viz around 0.1 $\times 10^{-5}$ cm^2/s as shown in Table 5.5. This again points to the field gradient not being strong enough to allow for easy diffusion across the bilayer. Typical MSD plot has been shown in the Figure 5.11

However, it is clear that the effect of the potential gradient on the sodium ions is stronger than that on the Cl ions and after 40 ns of the simulation, there is the first indication of a Na^+ ion beginning to move across the bilayer. In Figure 5.10, which shows the instantaneous position of the ions after 50 ns of the simulation, the presence of a single sodium ion deep inside the membrane surface 50 ns is clear. By contrast, none of the chlorine ions are able to overcome the barrier at the surface of the membrane. It is also clear that the Na and Cl ions are distributed randomly over both fluid regions. Typical trajectory for both ions shown in Figure 5.12

In Figure 5.13, we show the time averaged number density for both sets of ions across whole of the simulation box. As was found for the simulations with just one type of fluid, we note that there is a high incidence of sodium ions near to the lipid surfaces while the chlorine ions prefer to move in the water region and away from the membrane. Again, integrating out the areas under the curves, we found that roughly 20% of the Na ions

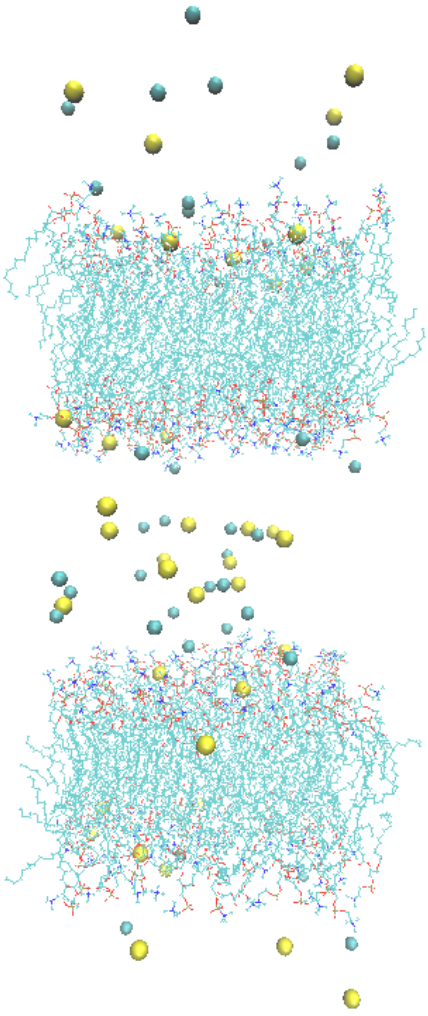

Figure 5.10: Figure showing the ion distribution in System D after 50 ns together with the two POPC lipid bilayers. The water molecules are not shown in order to highlight the positions of the Na (yellow) and Cl (blue) ions.

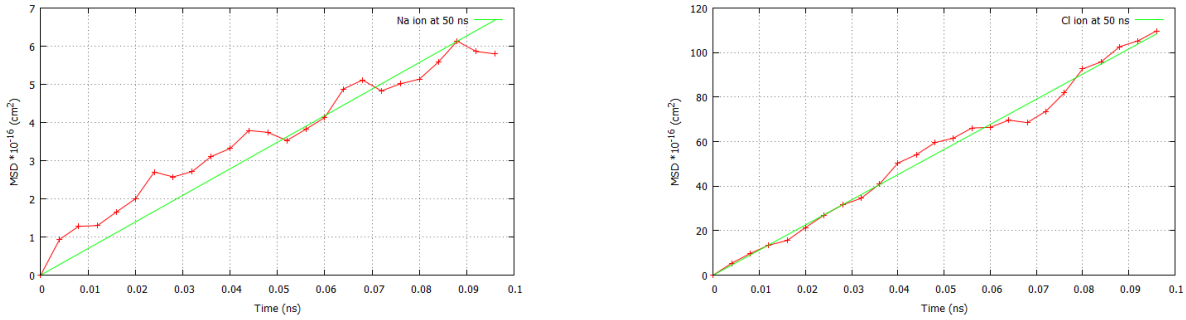

(a) Na ion

(b) Cl ion

Figure 5.11: Typical MSD plots over the last 10 ns of the simulation Na (a) and for Cl (b) ions in System D

are at or below the surfaces of the double bilayers. So, even though an electrochemical gradient has been established, it is not strong enough for the ions to overcome the barrier for diffusion across the bilayers.

5.6.2 Results of simulations of System E

It has been suggested that [84] that the permeation barrier for both Na and CL ions in simulations of this size is too large for the observation of ion diffusion events. It has been estimated that more than 100 hours of CPU time might be required to observe such events. It is also clear that the lack of diffusion across the bilayer in System D over time scales that are computationally feasible is a consequence of the weak electrochemical gradient. So, in order to speed up the diffusion process, it was decided to construct a system (System E) with a much stronger electrochemical potential gradient. This was generated by placing 50 Na^+ ions in the inner fluid region and 50 Cl^- in the outer fluid region.

The molecular dynamics simulations were then carried out as described above for the other systems. In a very short time, less than 0.004 ns of starting the simulation, water molecules break through the membrane and create what is referred to as a water pore.

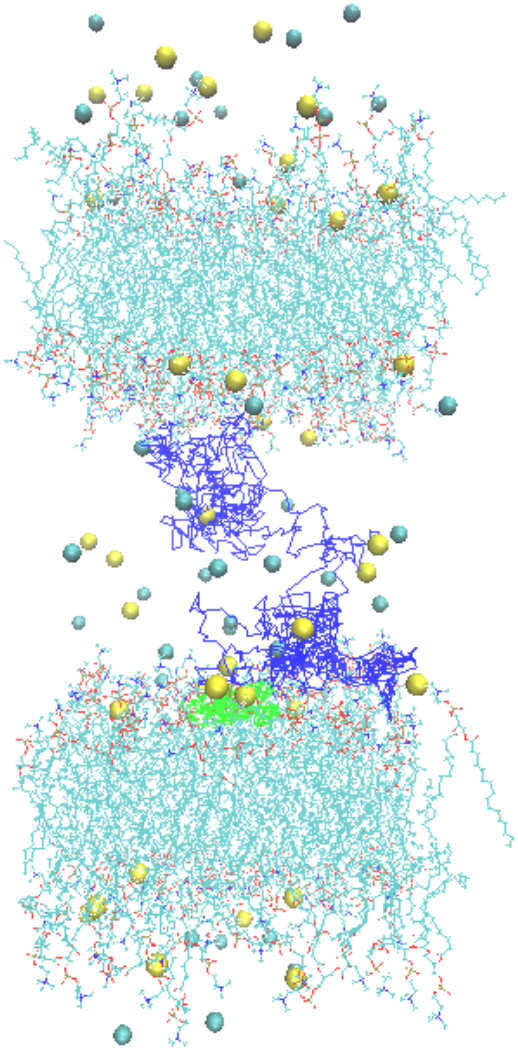

Figure 5.12: Typical trajectories (in green) for Na and (in blue) for Cl over last 10 ns in simulation System D.

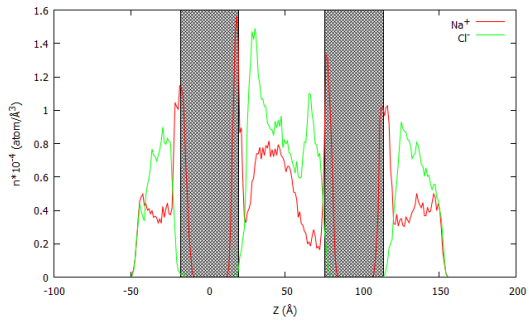

Figure 5.13: The time averaged over 50 ns number density of both ions as a function of z-axis for System D. The bilayer regions are indicated by the shaded areas.

The evolution of the pore and the transference of ions from one fluid the other, across the membrane, can be seen in the snapshots at particular times of the simulation (see Figures 5.14 and 5.15). At the end of the simulation run of 65 ns, final distribution of the ions, shown in Figure 5.16, suggest that near charge equilibrium has been re-established.

The electrostatic potential energy over a three dimensional grid of the simulation box was also calculated. In Figure 5.17 is shown the potential profile across the two bilayers averaged over the lateral positions at the time steps corresponding to the simulation times in Figure 5.14. It is interesting to note from these plots that there is a dramatic reduction in the strong electric field gradient within the first 2.1 ns after which the changes are relatively minimal. However, after 65 ns, there is still a small field gradient between the two bilayers.

To analyze this further, we have also plotted the electrostatic potential map in the cross-section of cell (Figure 5.18) at these different time steps. These confirm the changes in the electrostatic potential spread right across the membrane and is not just confined to the pore region.

Interestingly, the potential profiles across the membrane at different $(x,\ y)$ positions looks remarkably similar (Figure 5.19). This is rather surprising as the electrostatic map in Figure 5.18 suggests that there are quite important differences at different lateral positions. At the start of the simulation, they are virtually identical. However, once a

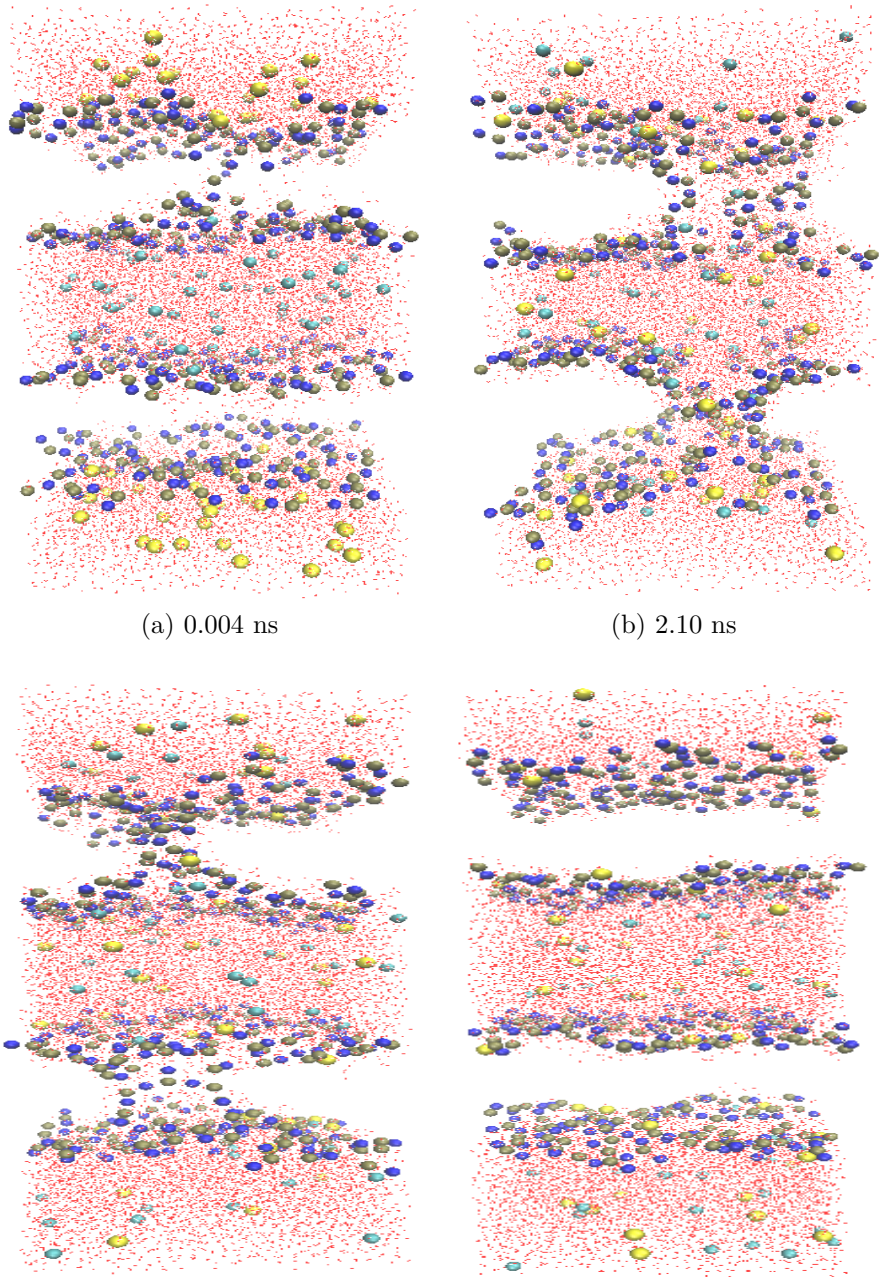

(a) 0.004 ns

(b) 2.10 ns

(c) 10 ns

(d) 65 ns

Figure 5.14: Figure showing the water molecules and ion distribution in System E at different times of the diffusion process. Here, the Na ions are coloured yellow and the Cl ions cyan. The atoms comprising the two POPC lipid bilayers are not shown in order to highlight the opening up of the pore.

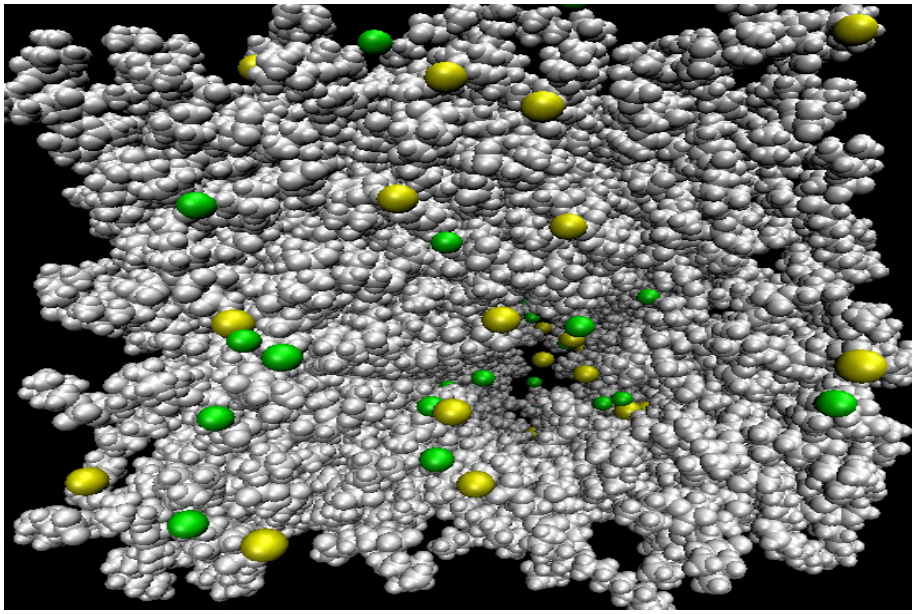

Figure 5.15: Top view of the membrane showing the pore that allows for the passage of ions through the membrane.

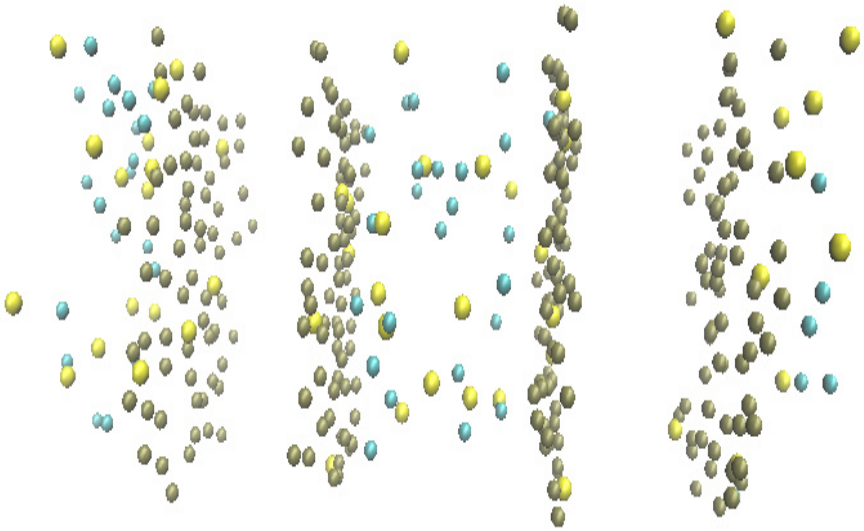

Figure 5.16: The ion distribution for System E at the end of the simulation run. The Na ions are coloured yellow, the Cl ions are cyan while the phosphorous atoms which mark the lipid bilayer surface edges are colored tan. The approximately equal numbers of Na and Cl ions in both fluid regions show that near equilibrium has been established.

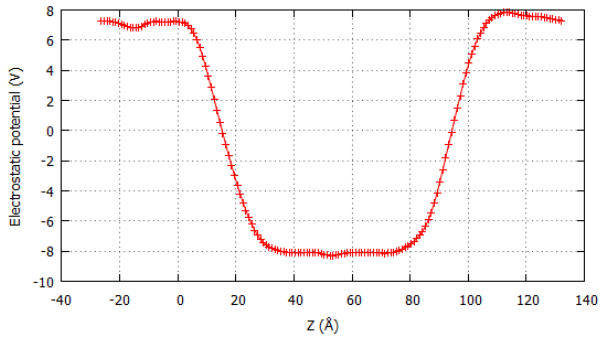

(a) t = 0.004 ns

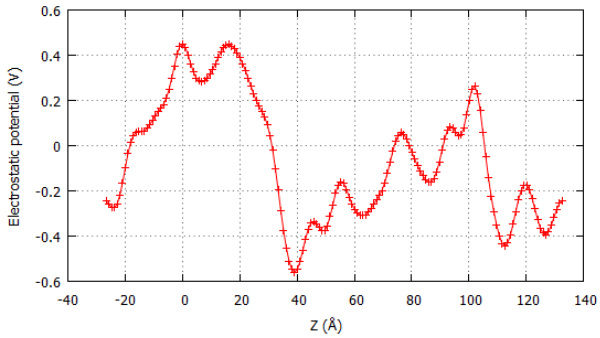

(b) t = 2.10 ns

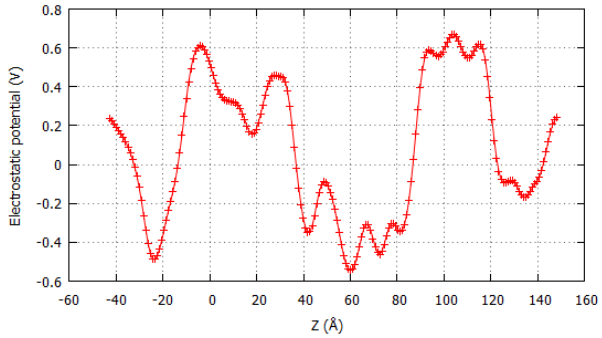

(c) t = 10 ns

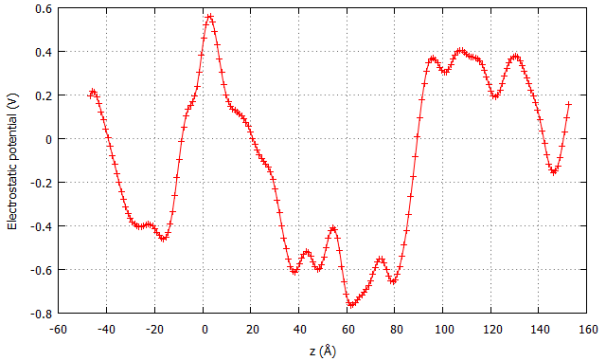

(d) t = 65 ns

Figure 5.17: The electrostatic potential plotted across the simulation cell at different times, t for System E. Note that soon after diffusion commences, there is a sharp drop in the electrochemical potential. This is reflected in the voltage scales on the vertical axis

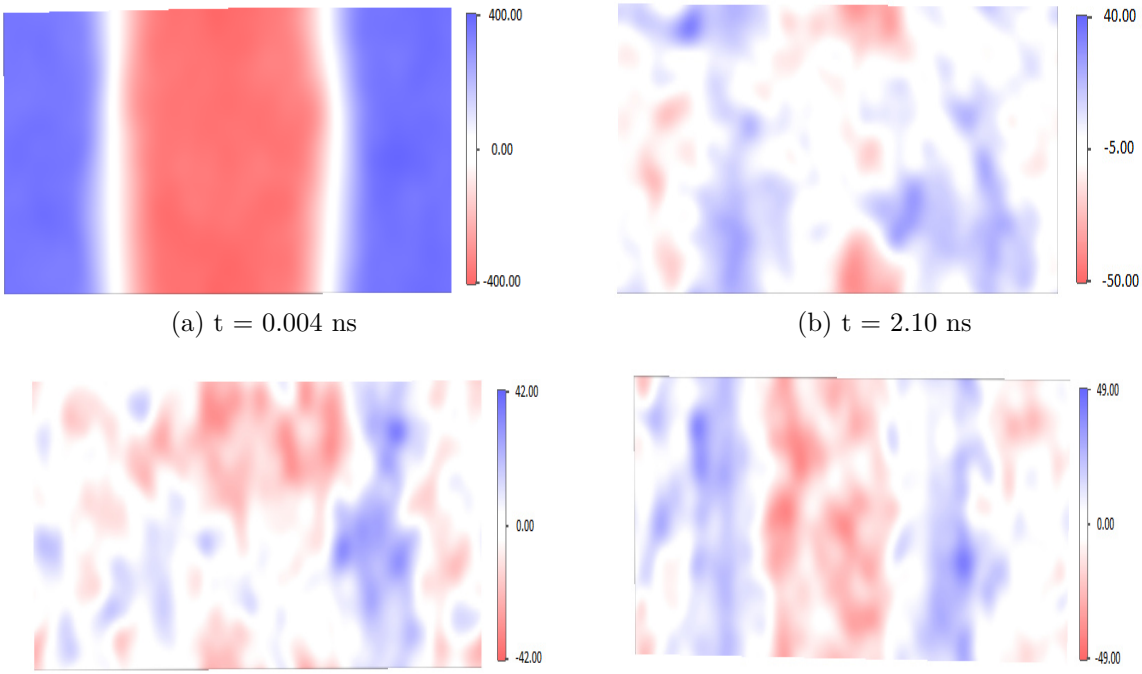

(a) t = 0.004 ns

(b) t = 2.10 ns

(c) t = 10 ns

(d) t = 65 ns

Figure 5.18: Electrostatic potential map ($x - z$ plot) across the two lipid bilayers at different times, t for System E.

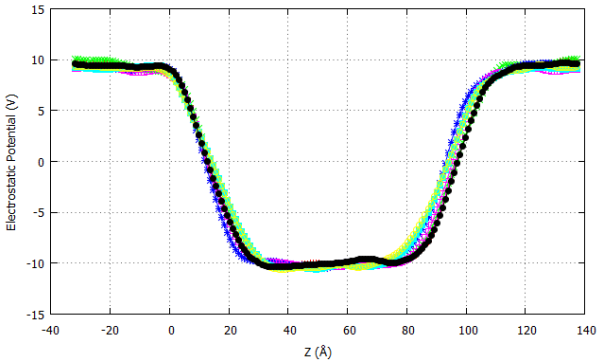

(a) t = 0.002 ns

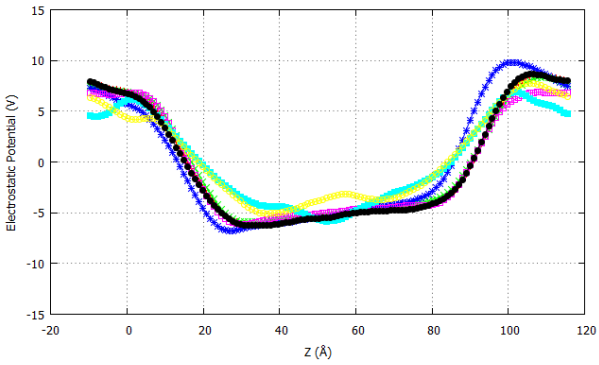

(b) t = 0.02 ns

Figure 5.19: Electrostatic potential profiles at different times, t, as a function of distance across the two bilayers for System E. The bilayer edges are at approximately -7 Å, 30 Å, 88 Å and 126 Å. The different colors denote different coordinates (x,y) on the bilayer surface.

pore is formed, deviations in the profile tend to reflect the atomic displacements of the lipid molecules and the consequential charge density changes.

In order to examine the flow of ions across the membrane in a more detailed manner, we have plotted the number density of both Na and Cl ions across the simulation cell at different times (Figure 5.20). It is clear from these that the Na ions are the first to penetrate into the membrane. This happens to a substantial degree within the first 0.02 ns. However, it does not take much longer for the Cl ions to also move through the membrane so that within 5 ns of the start of the simulation, most of the ions (Cl and

Table 5.6: Diffusion coefficients, D ($\times 10^{-5}$ cm^2/s), of H_2O molecules, Na^+ and Cl^- ions at different times during their passage through the pore.

	$D(Na^+)$	$D(Cl^-)$	$D(H_2O)$
0.022 ns (in pore)	42.2	76.2	22.9
10 ns (in pore)	1.3	1.9	2.5
10 ns (in bulk water region)	1.7	2.6	5.0

Na) have already moved onto the other side of the membrane to establish near charge neutrality.

Gurtovenko and Vattulainen [75] found the rather surprising result that both positive and negative ions leaked across membrane in approximately the same ratio despite the fact that Na ions have a lower potential barrier for permeation through the pore. Our results suggest that this lower potential barrier is responsible for the Na ions being the first to penetrate, but following this, the Cl ions move through the membrane much more rapidly. We have calculated the diffusion coefficients from the MSD data (Figure 5.22) obtained from the ion trajectories and these are given in Table 5.6. The values of D for both ions in the bulk region are similar to that tabulated in Table 5.3. However, as the ions move through the pore, these values are greatly enhanced to more than 10 times as fast as in water. It is clear from this that the ions have very little interaction with any atoms or ions whilst in the pore. Interestingly, the Cl ions have a higher diffusion coefficient than the Na ions. Examples of typical trajectories for both Na and Cl ions and water molecules through the pore in the simulation system E are shown in Figure 5.21.

A confirmation of this result can be seen in the plot of number of ions in each of the fluid regions (Figure 5.23). While from the results in Figure 5.20, it is clear that although the Na ions are the first to permeate the membrane, once the Cl ions start to move, they diffuse faster and to such an extent that they reach equilibrium more quickly than do the Na ions.

From the results of these simulations, we have found that if a large enough electro-

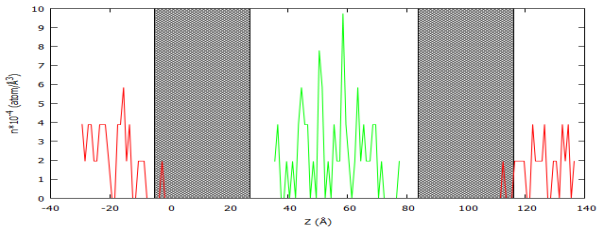

(a) 0.004 ns

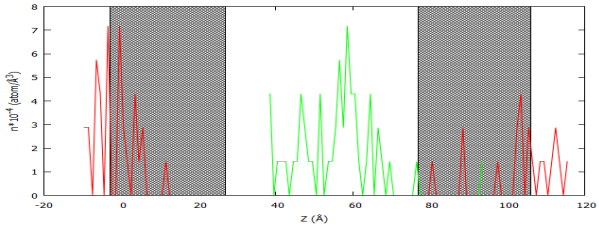

(b) 0.02 ns

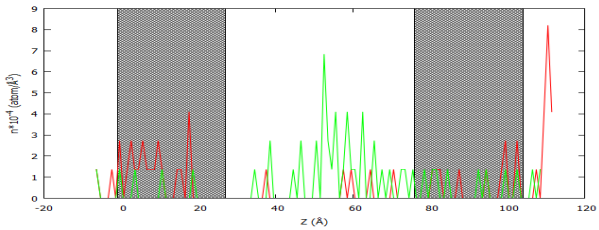

(c) 0.2 ns

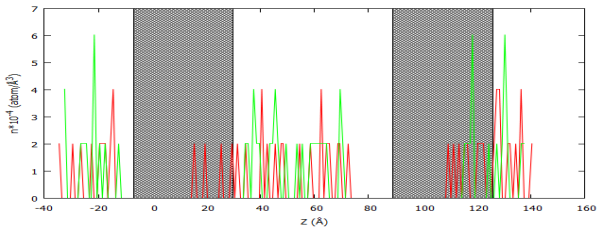

(d) 5 ns

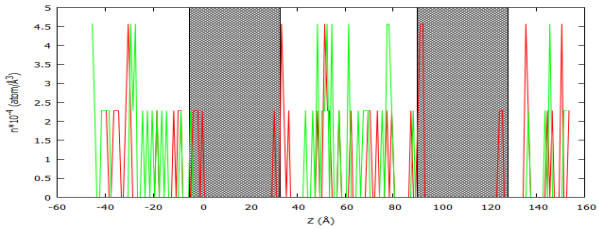

(e) 65 ns

Figure 5.20: Figure showing density distribution of Na (red) and Cl (green) ions in System E at different times of the diffusion process. The bilayer regions are indicated by the shaded areas.

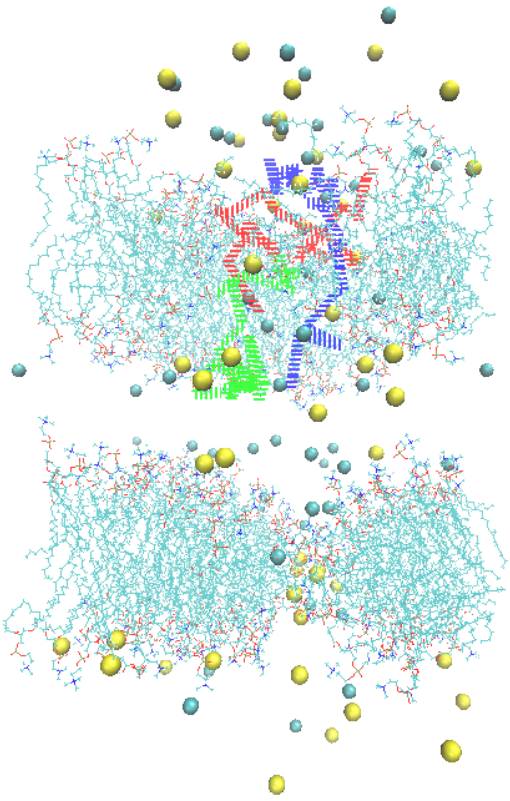

Figure 5.21: Typical trajectories (in green) for Na ions, (in blue) for Cl ions, and (in red) for water molecules over 0.62 ns in simulation System E.

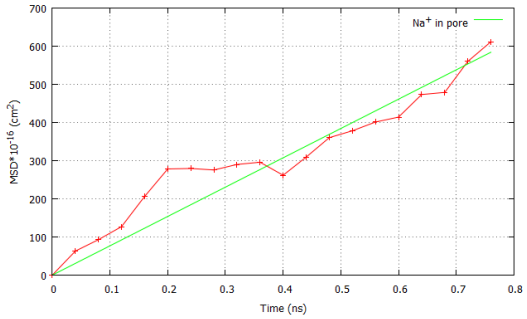

(a) Na (at 10 ns)

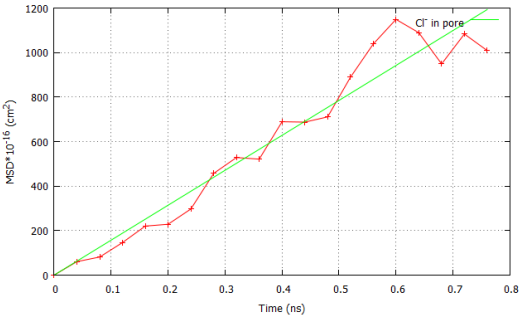

(b) Cl (at 10 ns)

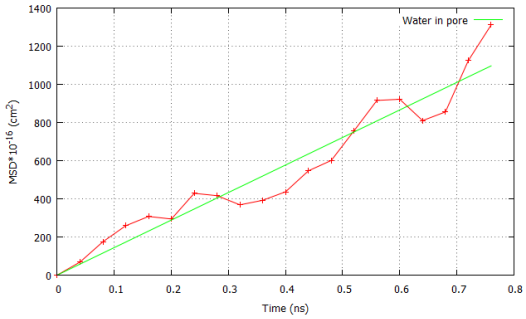

(c) H_2O (at 10 ns)

Figure 5.22: Showing the MSD for ions and water molecules in System E of the diffusion process inside the pore.

chemical potential gradient is established across the lipid bilayer membrane, both Na and Cl ions are able to permeate across the membrane. The relatively lower potential barrier experienced by the Na ions means that these are the first to start the diffusion process. However, once the pore has opened, the Cl ions move very fast through the membrane so as to establish near charge equilibrium. Full charge equilibrium is never established because once the electrochemical gradient has decreased sufficiently, diffusion events become extremely rare.

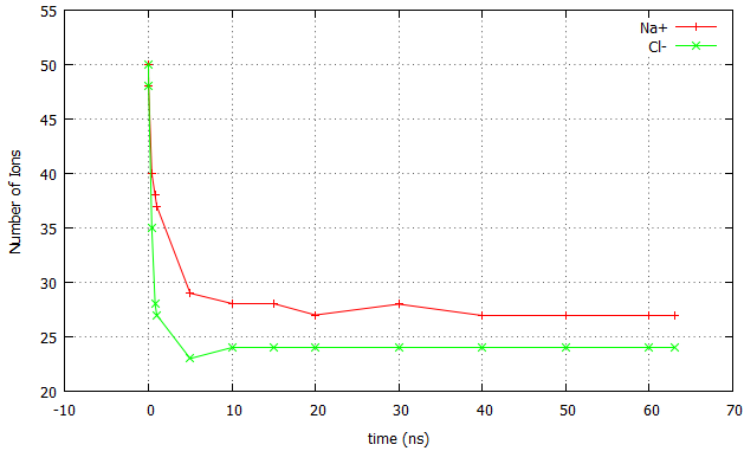

Figure 5.23: Showing the reduction in the ion numbers for both Na and Cl in each of the fluid regions I and II respectively, as a function of time. The difference between the two at the end of the simulation points to the cessation of ion diffusion when the electrochemical potential is small.

5.7 Conclusion

MD simulations using NAMD were used to investigate the permeability of ions through the POPC lipid bilayer membrane. A number of different configurations were considered. It was found that when a membrane is surrounded on both sides by water molecules, there is a tendency for a single Na ion to be partially bound inside but near to the bilayer surface. It is, however, easily displaced out of its binding site. By contrast, Cl ions tend not to bind to sites, at or below the bilayer surface. When the water surrounds are replaced by a NaCl aqueous solution, the only observable change is that it has the effect of allowing the Na ions to penetrate more deeply and reside for longer periods inside the membrane. However, no permeation of either ion takes place. This turns out to be the case even when the NaCl aqueous solution has a net charge.

In order to force diffusion across the membrane, without the application of external electric fields, we constructed systems that had an imbalance of positively and negatively charged ions on either side of the membrane. We considered the cases of weak and very strong charge imbalance. In the latter case, we found that diffusion does take place

through the creation of a pore in the membrane. This is in general agreement with the findings of other workers.

By monitoring the ion trajectories, we have been able to show that both Na and Cl ions diffuse rapidly through the pore with diffusion coefficients up to forty times larger than in water. Thus, although the Na ions are the first to begin the permeation process due to the lower potential barrier it experiences, the Cl ions complete the permeation more quickly due to their faster diffusion rates. Rather surprisingly, while the water molecules also diffuse faster through the pore than in water, the diffusion coefficient only increases by a factor of five.

Chapter 6

Interaction of gold nanoparticles with POPC lipid bilayer membranes

6.1 Introduction

The interactions between gold nanoparticles (AuNP) and biological fluids have been long recognized as important in medical and technological applications. Gold nanoparticles are novel particles that are being designed to be used as agents to aid in the delivery of drugs into cells. This has useful implications in cancer therapy, medical diagnostics, cell imaging tools, therapeutic agent, spectroscopic detection and photothermal therapies [85–89]. For example, Wilczewska and *et al* [90] analyzed the aforementioned nanoparticles and their connection with drugs to design nanoparticles to act as drug delivery agents.

The importance of understanding the interaction between nanoparticles and biological systems is important not only in the design of medical therapeutics and also for estimating the effects from environmental exposure. The growing commercial use of nanoparticles has led to research aimed at understanding how nanoparticles might induce adverse effects from environmental and human exposure such as cytotoxicity [91–93]. Additionally,

in order to achieve efficient drug delivery into intracellular target compartments using nanoparticles much research needs to be carried out [94, 95]. For instance, a functionalized gold nanoparticle with cationic ligands can be used to penetrate a lipid bilayer, but this could lead to the creation of a hole or cause a disruption to the cell structure [94, 96].

The electrostatic interactions between nanoparticles and cellular membranes play a significant role in determining how a nanoparticle binds to a membrane or in causing membrane disruption [97]. Membrane disruption by nanoparticles is influenced by a number of factors, including the net charge on the nanoparticle, the surface area, and the nanoparticle size [94, 98]. Phospholipid model membranes have been shown to display ion leakage, pore formation, membrane deformation, and membrane binding induced by nanoparticles [89, 94, 99–101]. Tatur and *et al* used neutron reflectometry experiments [102] to investigate how functionalized gold nanoparticles interact with bilayer surfaces. A better understanding of nanoparticle properties might prove useful in novel biomedical applications.

In addition to all the experimental investigations, there have been numerous studies aimed at investigating the interaction of nanoparticles with biological membranes using computer simulation methods. Molecular dynamics simulations, including both all-atom (AA) and coarse grained (CG) models, of nanoparticles interacting with membranes have been carried out. For example, molecular dynamics simulations have been performed to study the translocation of nanoparticles through living cells. Because of their crucial role in the possible delivery of drugs and gene therapy, different shapes and sizes of the nanocarriers have been investigated [103, 104]. More recently, there have also been free energy calculations which measure the total change in energy on moving a monolayer-protected AuNP from an initial position in a solvent to the center of the bilayer [105]. The results of these free energy calculations appear to support the hypothesis that monolayer-protected AuNPs can be inserted in a stable way into lipid bilayers.

Despite much work being carried out on AuNP-membrane interactions, there are still

unanswered questions relating to the details at the molecular-scale of both nanoparticles and membranes. Thus, it is not clear whether the lipid structure is altered in any way during the interactions with the AuNP. Also, the microscopic structural details associated with the passage of nanoparticles across membranes in not fully understood.

6.1.1 Aim of the study

It is unlikely for gold nanoparticles beyond a certain size to passively permeate through a membrane as they are taken up by an endocytosis pathway, which involves receptor proteins and other proteins, such as clathrin. However, a plausible pathway for uptake of gold nanoparticles is a 3-stage process. First, the gold nanoparticle binds to the headgroups of the bilayer. Then the nanoparticle diffuses in 2D on the surface of the bilayer. Finally, the nanoparticle makes contact with a membrane protein that acts as a receptor, beginning the endocytosis process [106].

The aim of this study was to investigate the adsorption of gold nanoparticles on a membrane surface in order to gain an understanding of the first step in the translocation process. This has been done by carrying out several simulations with different initial conditions using the NAMD package. In order to be sure that the results are valid and reproducible, the nanoparticle was placed at different random positions on the bilayer surface and the simulations were repeated several times. Free energy calculations were also carried out as these take into account entropy effects which could play a crucial role in adsorption.

Then, we carried out the simulations with free energy calculations using adaptive bias force (ABF) to better understand the interaction between AuNP and the membrane by calculating the potential mean force.

Furthermore, as a means of determining the potential energy barriers to AuNP translocation across a membrane, the nanoparticles on the membrane surface were given different

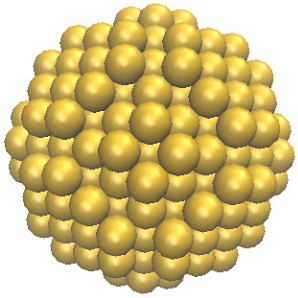

Figure 6.1: The structure of a neutral gold nanoparticle with a diameter of 2.2 nm.

velocities perpendicular to the surface to determine the minimum force required for AuNP translocation. This was done by carrying out steered molecular dynamics simulations on neutral gold nanoparticles using the constant velocity pulling method.

6.1.2 Layout of this chapter

In the next section (Section 6.2), we give a give a brief overview of gold nanoparticles including a description of how they are constructed and charged. In Section 6.3, we report on the results of molecular dynamics simulations undertaken to determine the adsorption sites and energies of the neutral and charge gold nanoparticles. This followed in Section 6.4 with the results of free energy calculations of the gold nanoparticles on the membrane surface. The constant velocity pulling method using Steered Molecular Dynamics was then used to investigate the possible translocation of the gold nanoparticles across the membrane in Section 6.5. Finally the results of this chapter are brought together in the conclusion.

6.2 Gold nanoparticle structure

Gold (Au) has atomic number 79 and is a good heat and electrical conductor. It can be rolled to form thin sheets or made into different shapes as it is malleable and soft. It is also quite inert and does not easily react, hence it is called a noble metal. For this reason

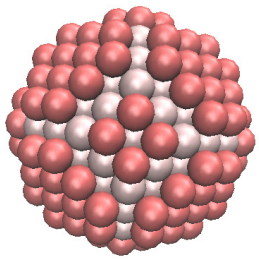

Figure 6.2: The structure of charged a gold nanoparticle with diameter of 2.2 nm. The red gold atoms on the surface of the nanoparticle are charged, while the atoms inside the nanoparticle are neutral.

and due to its weight (density) it is used in jewellery products, electronics, dentistry, and for medals in rewarding achievement. More recently, it has become important in medical applications.

Crystalline gold has a cubic close packed or face-centered-cubic (FCC) structure with the edge of each cube 4.07 Å long. In this cubic structure, eight atoms are to be found at each corner of the cube and six atoms are in the middle of each cube face. Gold nanoparticles are stable particles which also have a nearly face-centered-cubic structure but is also nearly spherical in shape. To construct the spherical gold nanoparticles used in this study, VMD was used to first build a block of bulk gold with a FCC lattice structure after which it was cut to form a nearly spherical shape of diameter approximately 2.2 nm. The resulting gold nanoparticle is shown in the Figure 6.1. The gold nanoparticles can be negatively or positively charged, or it can be left in a neutral state. For our purposes, the differently charged gold nanoparticles were constructed by adding a charge to only the surface atoms of the nanoparticles as shown in the Figure 6.2. More information about gold crystal structure can be found in [107–109].

6.3 Adsorption of gold nanoparticles on the membrane surface

6.3.1 Systems and simulation method

The system under investigation in this project consisted of a gold nanoparticle in or on the surface of a POPC lipid bilayer membrane surrounded by water molecules. The near spherical gold nanoparticle of diameter 2.2 nm comprised 321 atoms. The lipid bilayer (POPC) membrane was made of 21842 atoms and solvated in a box containing 14797 molecules of water as shown in Figure 6.3. This was done for for three types of AuNP.

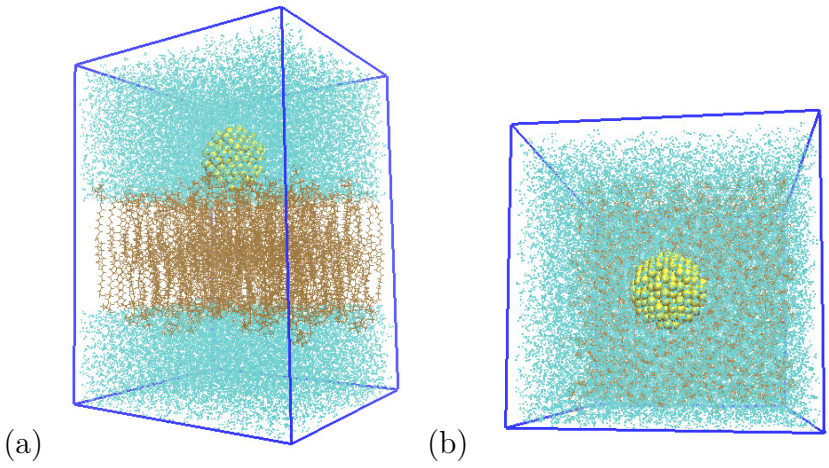

Figure 6.3: A lipid bilayer membrane with a gold nanoparticle all solvated in a box of water: (a) Side view; (b) Top view.

We have performed molecular dynamics simulations (MD) using the NAMD (2.10) package with periodic boundary conditions. The dimensions of the simulation box were $80 \times 80 \times 110$ Å^3. For simulating the interaction of charged AuNPs with the membrane, a charge of ± 1 e was equally distributed over the 120 atoms on the surface of the AuNP.

In all the simulations, the system was kept at a constant temperature of 300 K and Langevin dynamics was applied with a Langevin damping coefficient of 1 ps^{-1}. An

isothermal-isobaric ensemble (NPT) was used with an isotropic pressure of 1 bar applied using a modified Nose-Hoover method. The CHARMM36 force field parameters were used for both the water and the lipid interactions. For the Au-Au interactions and for the interactions between the Au and the lipid and water atoms, LJ force fields were assumed with the values of the parameters taken from Vila Verde *et al* and Wright *et al* [110, 111]. The MD integration time step was taken to be 2 fs.

The calculation of non-bonded interactions is the most time consuming part in MD simulations. We therefore used a 12 Å cutoff for both van der Waals and short-range interactions. A switching-on function starting at 10 Å for van der Waals interactions ensured that the cutoff was smoothly achieved. The long-range electrostatic interactions were computed using the Particle-Mesh Ewald (PME) method with a grid point density of over $1.2/\text{Å}^3$. In order to study the adsorption energies of charged and neutral AuNPs on the membrane surface, a total of nine different simulations were performed. In each of these, a single gold nanoparticle was placed on the surface of the bilayer. Two adsorption sites were chosen, one at the near geometric center of the membrane surface (C) and the other near the edge of the simulation box (X) as shown in the Figure 6.4. For the AuNP at site C, two different simulation temperatures were investigated. The details of these simulations are given in Table 6.1.

All systems were first energy minimized for 5000 steps using the conjugate gradient method. Then, the systems were allowed to evolve for a period of 50 ns. The calculations were carried out using the computational facilities of the Advanced Research Computing@Cardiff (ARCCA) Division, Cardiff University.

Table 6.1: Systems details

	Temperature (K)	type of AuNP	initial position of AuNP
1	300	neutral	C
2	300	positive	C
3	300	negative	C
4	400	neutral	C
5	400	positive	C
6	400	negative	C
7	300	neutral	X
8	300	positive	X
9	300	negative	X

6.3.2 Results and discussion

Over the 50 ns of each simulation, the positions of each individual atom of the system at each time step were saved to be used in the subsequent analysis. At each time step, the thickness of the lipid bilayer (BLT) and the area per lipid (APL) were calculated using MEMBPLUGIN [112] and these results are shown as time series data in Figure 6.5 and Figure 6.6. The average values of these quantities over the whole run for each simulation are given in Table 6.2.

It is evident that the charge on the gold nanoparticle has a serious impact on the BLT and the APL. As mentioned before in the last chapter, these changes are inversely related. In addition, the position of the adsorption site and the temperature of the simulation are also important factors in determining the thickness and area per lipid. The increase in the APL and corresponding decrease in the BLT point to the AuNP has the equivalent effect of squeezing the lipid bilayer. When the nanoparticle is placed at C, the neutral and positively charged AuNP have the greatest effect on the BLT. This suggests that these interactions are stronger and more attractive, at least in the region of the nanoparticle. Rather surprisingly, when the AuNP is placed at X, the interaction of the negative nanoparticle with the membrane is enhanced and now the negatively charged AuNP is more strongly attracted to the bilayer. When the temperature is increased to

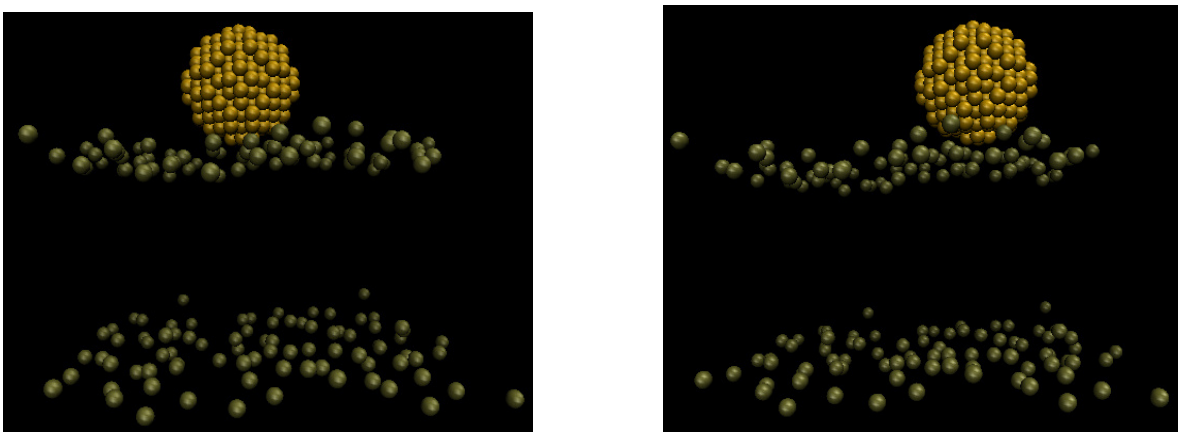

(a) C-site (side view)

(b) X-site (side view)

Figure 6.4: Figure showing two samples of the system only the phosphorous atoms of the bilayer surface and AuNP are shown.

400 K, all three AuNPs have essentially the same effect. This is consistent with the view that the nanoparticle-membrane interaction is relatively weak such that the main effect of an increased temperature is manifest purely in the atomic structure of the bilayer.

In order to better understand these results we have also calculated distance from the centre of mass of the AuNP to the centre of mass of the lipid bilayer (phosphorus). From

Table 6.2: Results

Temperature (K)	charge	site	thickness (Å)	Area per lipid (Å^2)
300	neutral	C	32.8 ± 0.3	77.5 ± 1.0
300	positive	C	34.0 ± 0.8	75.6 ± 1.6
300	negative	C	37.3 ± 1.7	68.4 ± 4.0
400	neutral	C	36.6 ± 0.6	78.7 ± 1.6
400	positive	C	36.6 ± 0.6	79.0 ± 1.6
400	negative	C	36.7 ± 0.7	78.5 ± 1.5
300	neutral	X	34.4 ± 1.0	74.4 ± 2.9
300	positive	X	32.3 ± 0.2	78.4 ± 0.5
300	negative	X	31.9 ± 0.2	80.6 ± 0.6

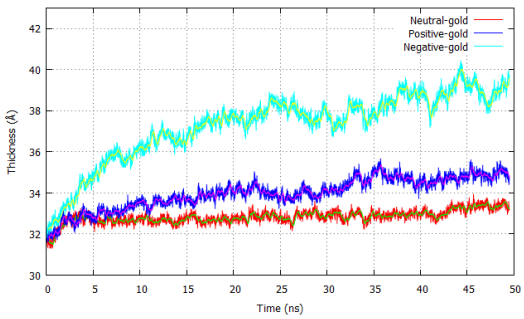

(a) C-site 300 K

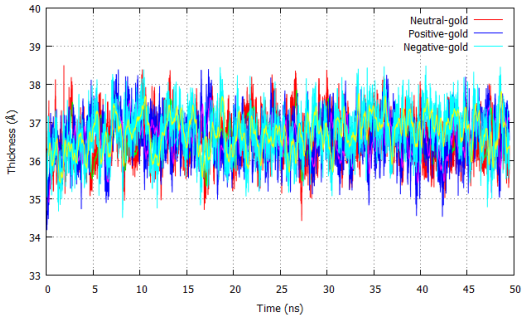

(b) C-site 400 K

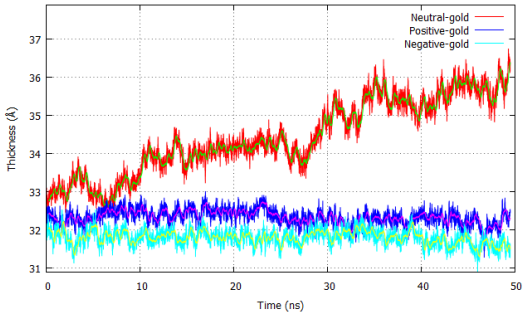

(c) X-site 300 K

Figure 6.5: The BLT of the POPC bilayer membrane for the three types of AuNP.

the results shown in the Figure 6.7, it is clear that at 300 K and with the nanoparticle placed at C, the neutral AuNP moves deeper inside the membrane surface than the others within the time window explored. Both the charged AuNPs appear to be the same distance from the centre of the bilayer. However, a snap shot of the final positions as shown in Figures 6.8, 6.9 and 6.10 reveals that while the positive AuNP partially penetrates the surface, the negative AuNP does not. Instead, the decrease in the distance may be attributed to the sagging of the membrane surface layer. When the temperature is increased to 400 K, all three AuNP penetrate deep into the bilayer as can be seen in Figure 6.7 and Figures 6.11, 6.12, and 6.13. From the results of the simulations of the AuNP at adsorption site X and at 300K (Figures 6.14, 6.15, and 6.16), it is clear that both charged AuNP's are not attracted to the inside of the membrane. The neutral AuNP

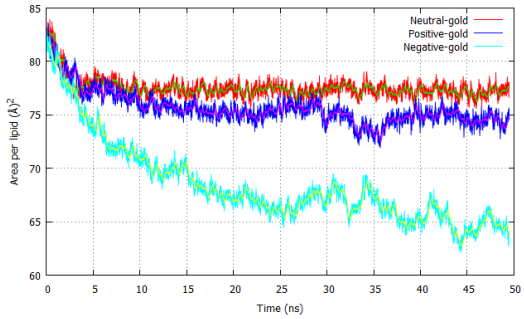

(a) C-site 300 K

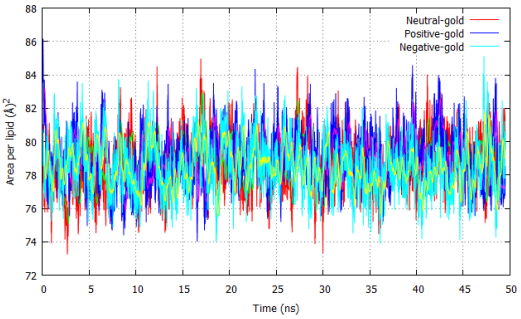

(b) C-site 400 K

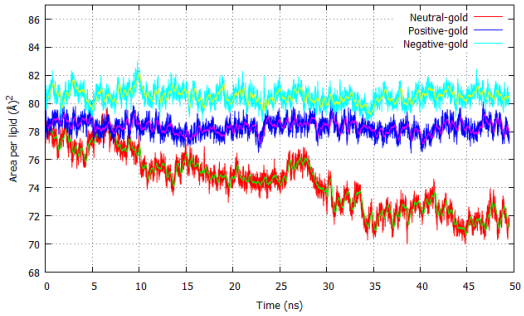

(c) X-site 300 K

Figure 6.6: The APL of the POPC bilayer membrane for the three types of AuNP.

does partially penetrate the surface, but is not as deep as when placed at site C.

6.3.3 Conclusion

In summary, the results of these simulations suggest that when gold nanoparticles are placed on a lipid bilayer surface, the interactions between the gold atoms and the surface atoms in its vicinity is crucial in determining the extent of penetration, if any, of the AuNP. Thus, the attraction between the surface and the neutral AuNP is greater at site C than at site X. This site dependent interaction is even more evident in the case of the positive AuNP, which while penetrating the surface at C does not do so at X. This points to a negatively charged region just below the surface at C and may be attributed to the carboxyl groups. In fact, this was also observed in our investigations of the diffusion of Na

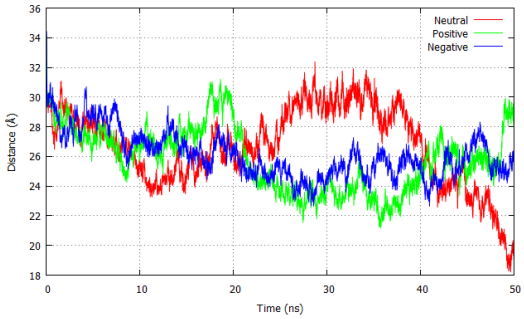

(a) C-site 300 K

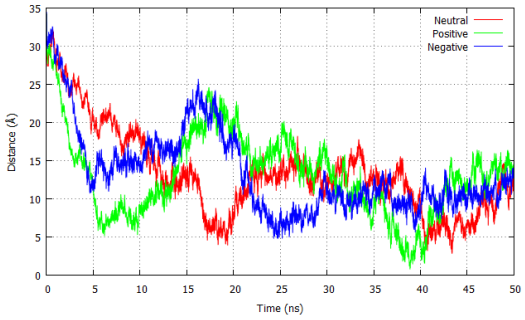

(b) C-site 400 K

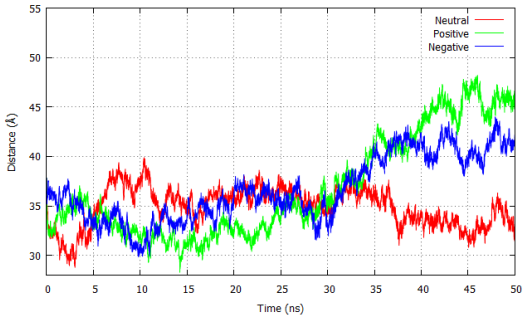

(c) X-site 300 K

Figure 6.7: Figures showing the distance between the center of mass of the POPC bilayer membrane and AuNPs .

ions reported in the last chapter. These results are consistent with experimental findings which confirm that negative charged gold nanoparticles are repelled by the surface of the bilayer. In contrast, positively gold nanoparticles tend to pass through the fluid phase of the lipid membrane and remain in the hydrophobic moiety of the floating bilayer [102].

Our simulations at 400 K were designed to give some information about the strength of the above mentioned interactions. In this case, the passage of all three AuNPs indicate that temperature and entropic effects dominate at this temperature. Again, this is not surprising when dealing with biological systems.

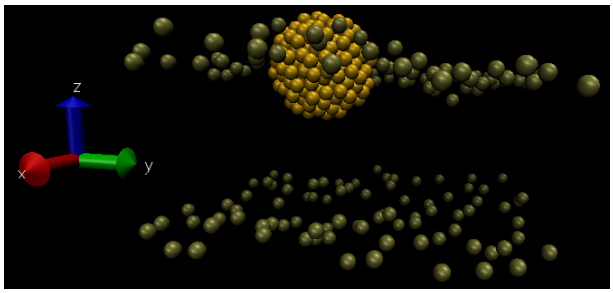

Figure 6.8: The neutral charged gold nanoparticle with headgroups of lipids (P) after 50 ns at 300 K, (nanoparticle placed at site C).

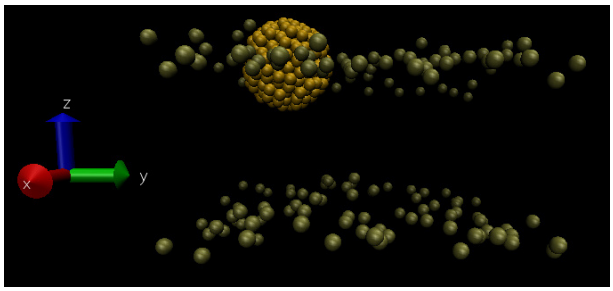

Figure 6.9: The positive gold nanoparticle with headgroups of lipids (P) after 50 ns at 300 k, (nanoparticle placed at site C).

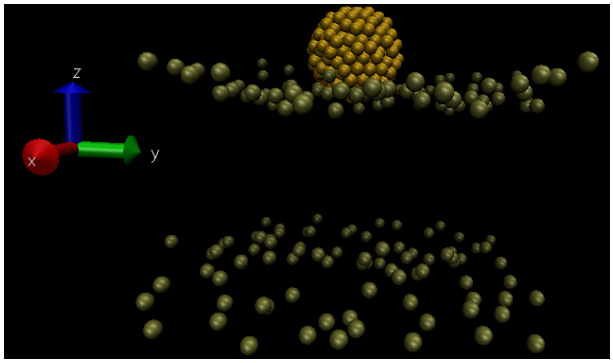

Figure 6.10: The negative charged gold nanoparticle with headgroups of lipids (P) after 50 ns at 300 K, (nanoparticle placed at site C).

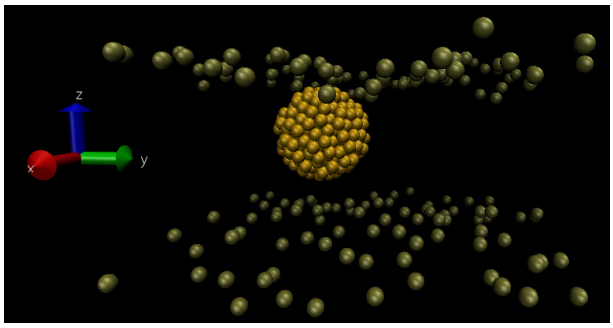

Figure 6.11: The neutral charged gold nanoparticle with headgroups of lipids (P) after 50 ns at 400 K,(nanoparticle placed at site C).

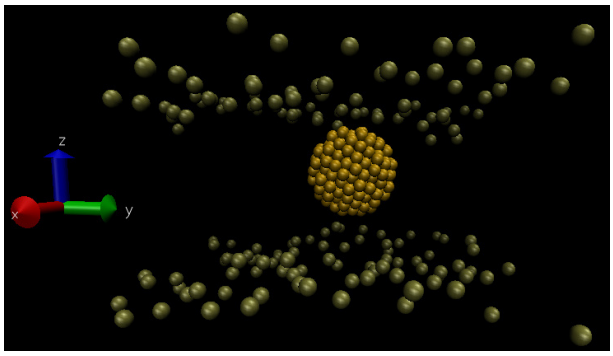

Figure 6.12: The positive charged gold nanoparticle with headgroups of lipids (P) after 50 ns at 400 k, (nanoparticle placed at site C).

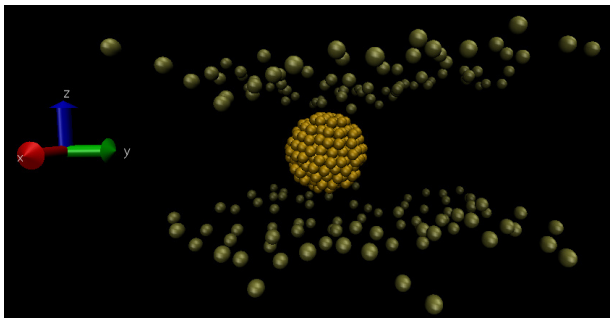

Figure 6.13: The negative charged gold nanoparticle with headgroups of lipids (P) after 50 ns at 400 K, (nanoparticle placed at site C).

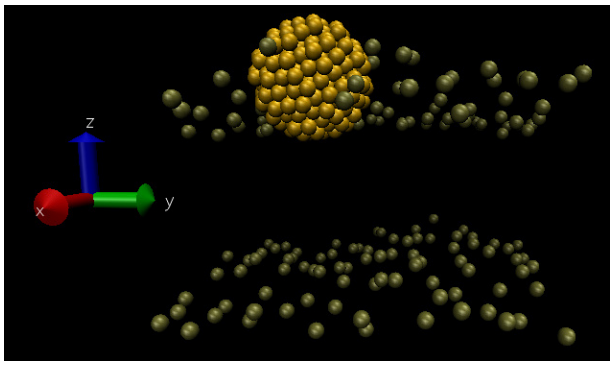

Figure 6.14: The neutral charged gold nanoparticle with headgroups of lipids (P) after 50 ns at 300 K (nanoparticle placed at site X).

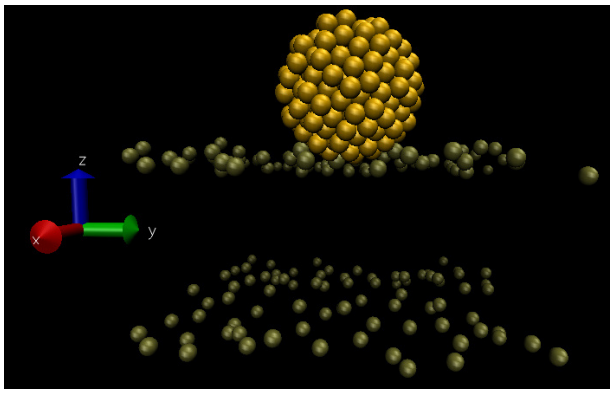

Figure 6.15: The positive gold nanoparticle with headgroups of lipids (P and N) after 50 ns at 300 K (nanoparticle placed at site X).

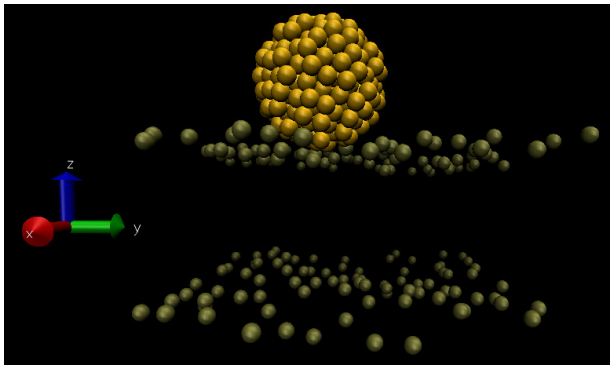

Figure 6.16: The negative charged gold nanoparticle with headgroups of lipids (P) after 50 ns at 300 K (nanoparticle placed at site X).

6.4 Free energy calculations of gold nanoparticles on the membrane surface

Gold nanoparticles larger than a certain size probably do not passively permeate through the membrane. They are likely to be taken up by an endocytosis pathway [113], which involves receptor proteins and other proteins, such as clathrin. Therefore, the free energy barrier for the nanoparticles to enter the membrane may be so high that passive membrane penetration never happens. What is relevant from the previous section is that we have shown that binding to the bilayer surface is favourable for gold nanoparticles. So, a reasonable pathway for the uptake of gold nanoparticles into a cell is that the gold nanoparticle first binds to the headgroup of a bilayer and then the nanoparticle diffuses in two dimensions on the surface of the bilayer. Therefore, to better understand the interaction between the gold nanoparticle and the surface of the lipid bilayer membrane, free energy calculations have been performed. This is because free energy calculations also take into account entropic effects which could be crucial for the diffusion of AuNPs through a membrane surface. There are different methods which have been developed to calculate free energies of condensed phase systems [77].

In many molecular dynamics simulations of chemical and biological systems the main objective is to calculate the free energy differences between different states. This can then provide information with regard to the probability of the system moving from one state to the other. These free energy calculations are different according to the type of system being studied. For example, computer simulation studies [114, 115] have been carried out in order to determine the non-monotonic differences in the free energy of two small, hydrophobic species in water as a function of their separation. Calculations of the permissibilities of lipid bilayer with importance sampling using an adaptive bias force combined with a Bayesian inference technique have been carried out to determine the free energy and diffusivity of gold nanoparticles on membrane surfaces [80].

One of the advantages of calculating the free energy of a system is that it is possible to map out the evolution of the global minimum energy which defines the state of the system in its lowest energy state. In general, the goals of these calculations are to investigate the free energy barriers that separates two states. This makes it possible to determine the stability of a system in a particular state and to determine the dynamic equilibrium between states when subject to external forces.

In our study, the free energy of the membrane-AuNP system has been determined by calculating the potential mean force as a function of the z-coordinates (or so called reaction coordinates ξ) of the system. This method has been used successfully to evaluate the ability of selected models of naked and hydroxylated carbon nanotubes to predict adsorption equilibrium constants [116]. Another study using this technique was to look for the minimum requirements in the replica exchange at different temperature using adaptive bias force simulations [117].

6.4.1 The ABF method and systems

Free energy calculations were carried out on the first three structures of the AuNP- lipid bilayer system as listed in Table 7.1. The parameters appearing in the force descriptions were taken to be the same as used in the previous section.

As before, for each simulation, the system was allowed to relax for 5000 steps in order to get to its minimum energy configuration. This was then followed by a calculation of the free energy using the MD method. The adaptive biasing force (ABF) method [39, 40] was then applied along the z component of the vector between the centre of mass of the gold nanoparticle and the centre of mass of the lipid bilayer membrane, using the Colvars module [38] with NAMD 2.10. The transition coordinate chosen to investigate the nanoparticle-membrane interaction was defined as the projection onto the z-direction of Cartesian space, i.e., the normal to the membrane, of the vector connecting the center of mass of the phosphorus atoms of the membrane to that of AuNP. The permeation

Table 6.3: Windows given for the free energy calculations

System	Window (Å)	Simulation period (ns)
Membrane & neutral gold NP	23-35	180
	23-28	60
	26.5-30	120
Membrane & positive gold NP	23-35	160
	23-28	142
	27-35	60
	27-32.5	120
	27-30	60
Membrane & negative gold NP	23-35	160
	29-35	60
	29-32.5	120

pathway was discretized in bins 0.1 Å wide, wherein samples of the local system force acting along z were accrued. Choosing this technique relies on estimating forces on the reaction coordinate which provides a convenient physical framework and guarantees long convergence [118]. The time-step has an important role in measuring the force on the biased atom within a 'bin' before the biasing force is applied. The significance of the time duration in the bin is to allow the system to relax from the non-equilibrium state to which it is introduced by the biasing force. The biased atom was kept within the outer z component boundaries of the reaction coordinate by a harmonic force implemented on the lipid bilayer membrane.

The calculations for each system were performed using a number of windows in three to five overlapping window sets as given in Table 6.3. Then, the force samples were collected in bins having widths of 0.1 Å after which the mean force is integrated to capture the small-scale variations of the free energy profile which is called the potential of mean force. These simulations were carried out for each of the systems with a simulated time for each window as shown in Table 6.3 .

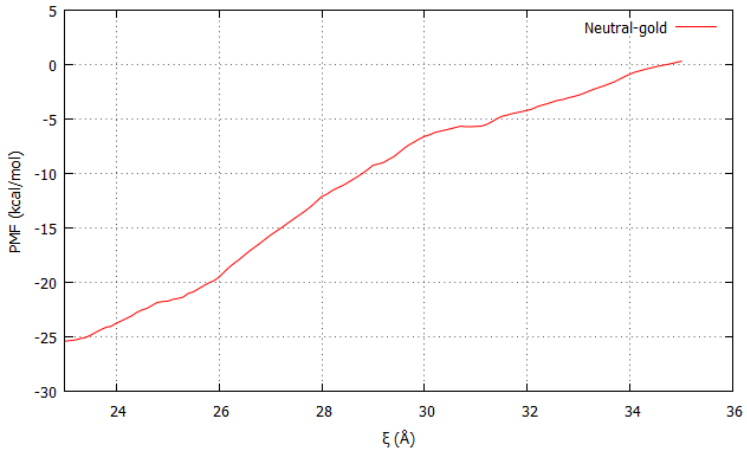

Figure 6.17: Calculated free energy as a function of reaction coordinate ξ for the neutral gold nanoparticle.

6.4.2 Results and discussions

Calculations aimed at determining the free energy of adsorbed nanoparticles on the bilayer surface were then performed for the three differently charged gold nanoparticles. This was done using the activation barrier by taking the minimum in the potential mean force (PMF) profile along the reaction coordinate ξ. Figures 6.17, 6.18, and 6.19 report the convergence studies of the potential mean force as a function of reaction coordinate for the three types of gold nanoparticles. In all cases the interactions between AuNP and the surface of the lipid bilayer are neglected at a distance larger than 31 Å.

From these plots we can see that for the negative AuNP system, the free energy shows no fluctuation for $\xi < 29.0$Å at which point the barrier is -7.91 kcal/mol. The minimum free energy occurs at $\xi = 29.2$Å with a value of -7.935 kcal/mol. The results of the simulations do not show any other barrier near the headgroups of the lipid bilayer surfaces. This means that the gold nanoparticle binds to the top of the choline group of the bilayer surfaces, which are the positive charge carriers. This prevents the negative gold nanoparticle from moving below the headgroups of the surfaces of the bilayer.

In contrast, for the neutral gold nanoparticle, the plot shows a minimum PMF at

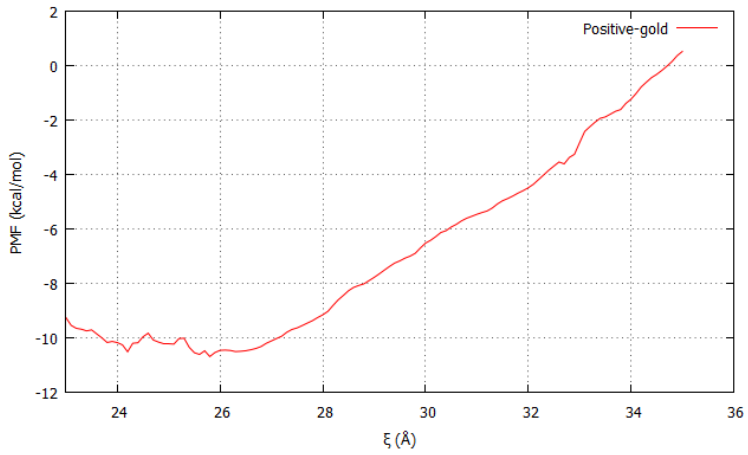

Figure 6.18: Calculated free energy as a function of reaction coordinate ξ for the positive gold nanoparticle.

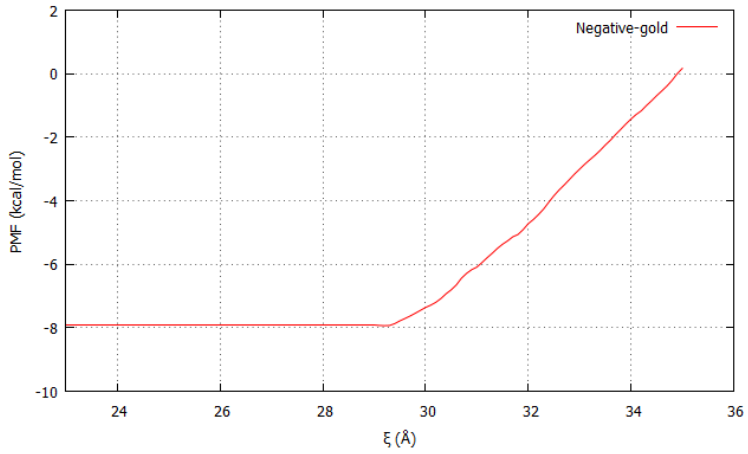

Figure 6.19: Calculated free energy as a function of reaction coordinate ξ for the negative gold nanoparticle.

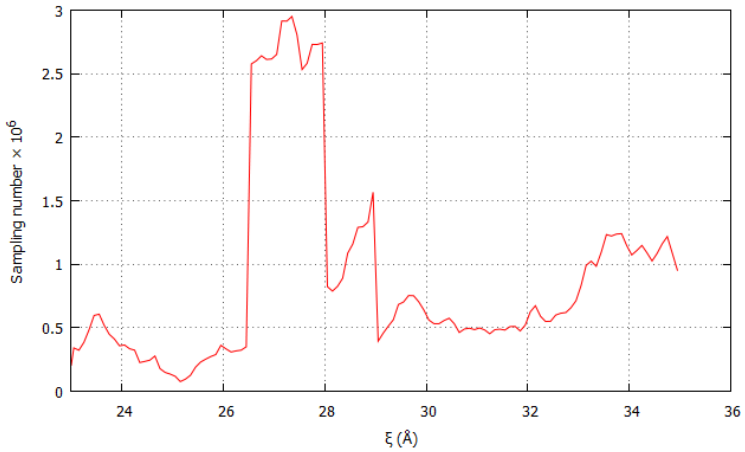

Figure 6.20: Number of force samples gathered by the ABF algorithm in a total of 360 ns (all windows) as a function of reaction coordinate ξ for the neutral gold nanoparticle.

ξ = 23.0Å and the free energy is -24.09 kcal/mol at this point. This indicates that the probability of nanoparticles around the surface of the bilayer is much higher than for the negative gold nanoparticle. The neutral gold nanoparticle partially penetrates the surface as shown in the Figure 6.32.

When the positive gold nanoparticle is placed on the bilayer surface, the minimum energy occurs at ξ = 25.6Å and has a value of -10.61 kcal/mol. As ξ is increased further, the free energy fluctuates around this value until another minimum energy is found at ξ = 25.8Å. This energy minimum is -10.69 kcal/mol. This indicates that the positive gold nanoparticles binds deep down to the phosphate groups of the surface bilayer, which are negative charge carriers, which it attempts to penetrate the surface.

Further, to determine how well the free energy converged on different parts of the domain, we analyzed the number of force samples collected by the ABF algorithm in each bin to capture every variation in the potential mean force as shown in Figures 6.20, 6.21, and 6.22.

For the negative AuNP case it is clear that there is no force sample gathered until ξ = 29.0 Å after which there is a rapid increase in sampling for $\xi > 29.05$ Å. This explains the estimate of free energy as shown in the PMF Figure 6.19. Therefore, the sampling plot

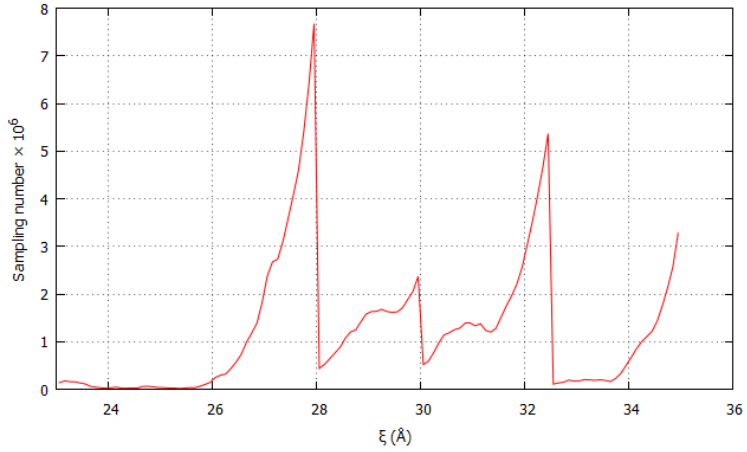

Figure 6.21: Number of force samples gathered by the ABF algorithm in a total of 542 ns (all windows) as a function of reaction coordinate ξ for the positive gold nanoparticle.

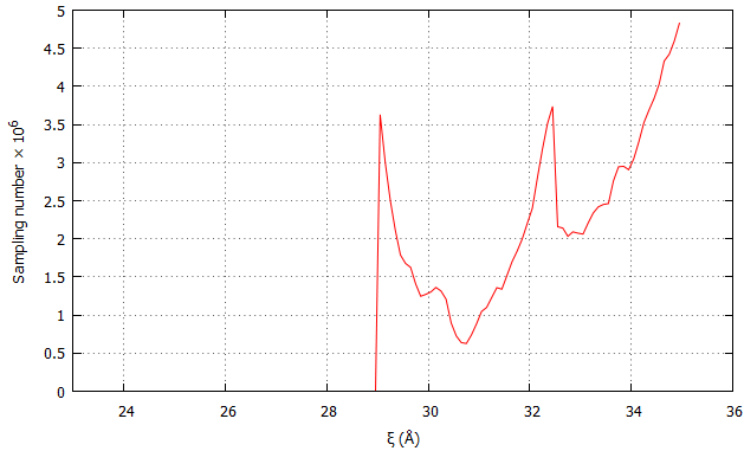

Figure 6.22: Number of force samples gathered by the ABF algorithm in a total of 340 ns (all windows) as a function of reaction coordinate ξ for the negative gold nanoparticle.

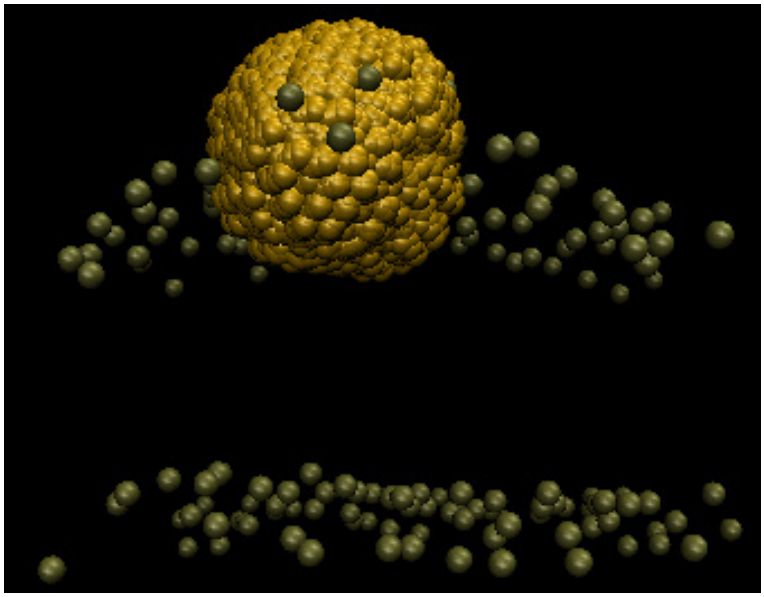

Figure 6.23: A typical trajectory for all frames from 0 to 2000 every 3 frames of the neutral gold nanoparticle on the lipid bilayer surface.

for the neutral AuNP case is adequate (agreement between two halves of the simulation is a good justification as explains later) between $24.0 < \xi < 26.5$ Å and then again at 30.0 until 32.25 Å. This is reflected in the estimate of the free energy as shown in the Figure 6.17. However, for the positive AuNP case, again there was adequate sampling and reaches maximum between $26.25 < \xi < 27.95$ Å then sampling decreases sharply at 28.05 Å. This shows that the minimum energy converges at bigger value of $\xi > 26.05$Å. Furthermore, it is better to display all conformations of gold nanoparticles on the surface during simulations by capturing every three frames of the trajectories as shown in the Figures 6.25, 6.23, and 6.24.

Then, in order to check convergence in two sections of the same trajectory, we used historical data to separate the data into two halves. This is a good justification if there is a agreement between the first and second halves. The first half and the final half of the trajectory allows us to produces a PMF with error bars. The error bars of the total mean force is estimated from the difference between the mean force for the first

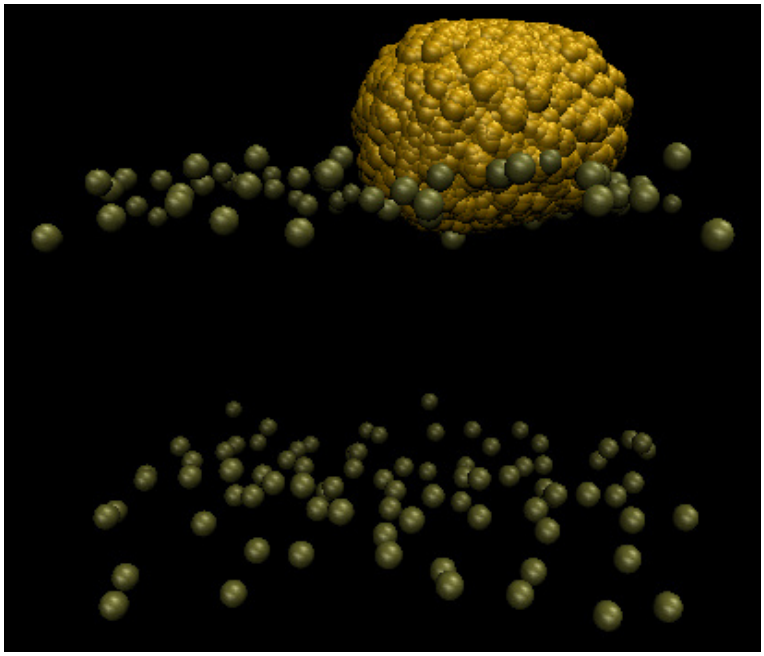

Figure 6.24: A typical trajectory for all frames from 0 to 2000 every 3 frames of the positive gold nanoparticle on the lipid bilayer surface.

and the second halves of the simulation for each window. These mean force errors are then integrated from the anchor points (stability in an otherwise uncertain situation) to take the error from the PMF. This was done by calculating the PMF values for all windows as shown in the Figures 6.26, 6.27, and 6.28. From those plots one can see there is a similarity between the first and second halves for the negative gold nanoparticle. However, for the positive and neutral ones, there is much less similarity between them. This shows that despite the counts are good in all simulations but the first and the second halves are adequate. Therefore, comparing two portions of the same trajectory is good for estimating convergence. Alternatively, it is good to check more accurately the convergence by carrying out the ABF calculations starting from different initial conformations.

The APL of the lipid bilayer POPC was calculated and found to be 64.0±0.9, 64.5±1.1, and 64.1 ± 1.1Å^2 for the neutral, negative, and positive gold nanoparticles respectively as shown in the Figures 6.29, 6.31, and 6.30. These results agree with the results of

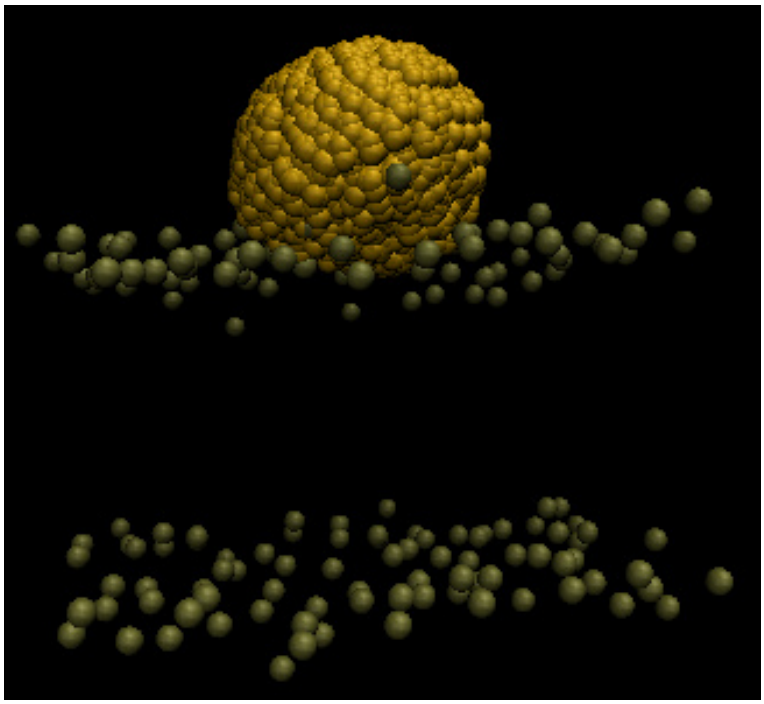

Figure 6.25: A typical trajectory for all frames from 0 to 2000 every 3 frames of the negative gold nanoparticle on the lipid bilayer surface.

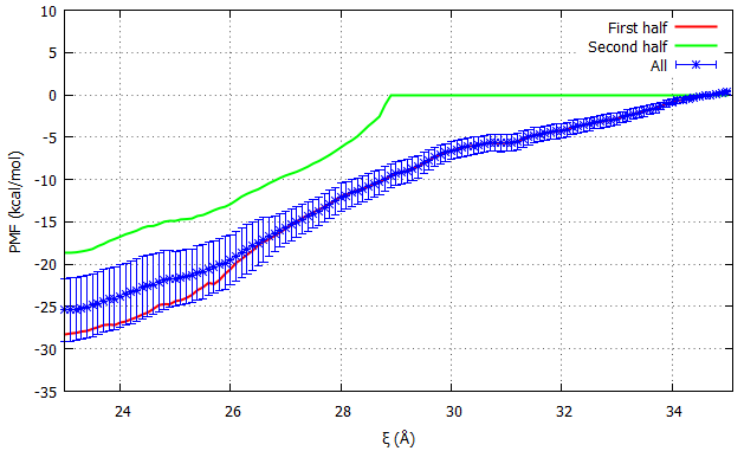

Figure 6.26: Comparison of calculated free energy between the first and the second halves of the trajectories for the neutral AuNP. Also shown is the free energy obtained when combining both halves. The error bars indicate the uncertainty in the results.

other calculations and of experimental work [32, 80, 119]. This tells us that lipid bilayer membranes in all three systems are thermally equilibrated at that temperature in these simulations.

6.4.3 Conclusion

In summary, the free energy of a gold nanoparticle adsorption at the bilayer surface was found as a function of distance along the normal axis ξ from the centre of membrane in the interval $23.0 < \xi < 35.0$Å. We found that both the positive and negative AuNP bind to the membrane but are not able to penetrate it. However, for a neutral AuNP we found a partial penetration of the nanoparticle into the bilayer as shown in the Figure 6.32. The binding of positive gold nanoparticle with lipid bilayer surfaces occurs between $25 < \xi < 29$Å. Rather surprisingly for the neutral nanoparticle, this occurs for $23.0 < \xi < 25$Å which is before 25 Å. Whilst these free energy calculations show good convergence, further investigations are needed before the binding energies may be taken to be accurate.

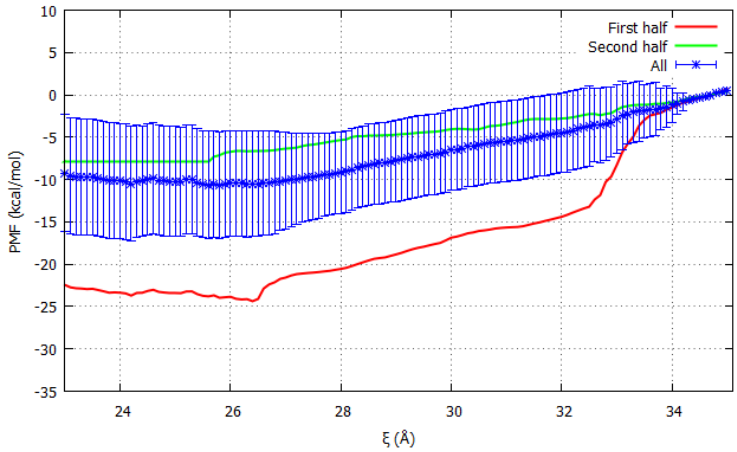

Figure 6.27: Comparison of calculated free energy between the first and the second halves of the trajectories for the positive AuNP. Also shown is the free energy obtained when combining both halves. The error bars indicate the uncertainty in the results.

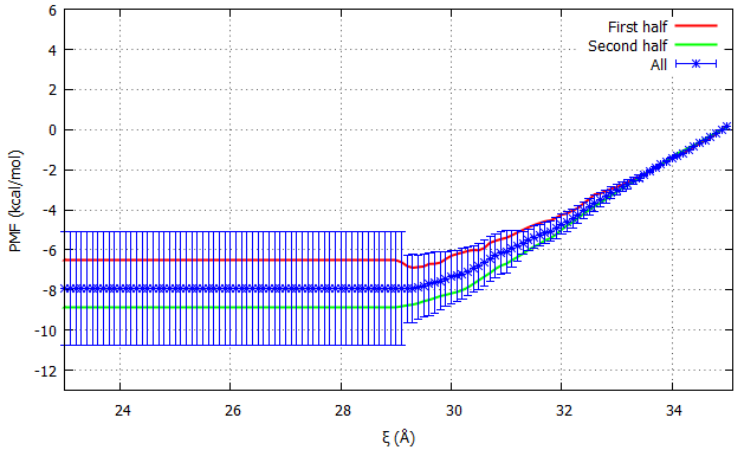

Figure 6.28: Comparison of calculated free energy between the first and the second halves of the trajectories for the negative AuNP. Also shown is the free energy obtained when combining both halves. The error bars indicate the uncertainty in the results.

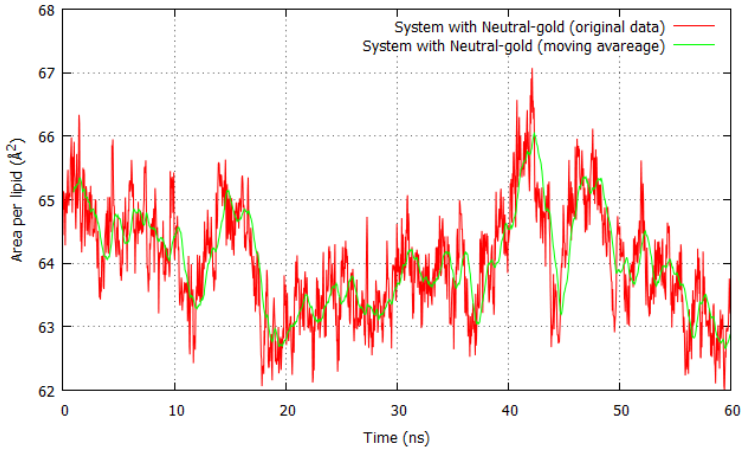

Figure 6.29: Area per lipid for the system with neutral gold nanoparticle.

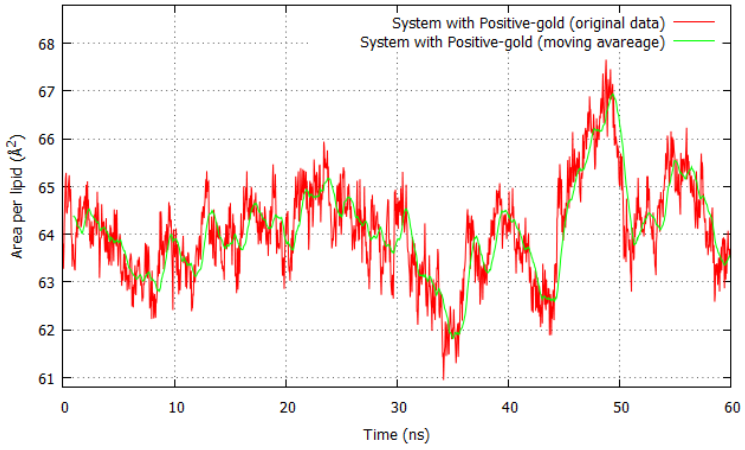

Figure 6.30: Area per lipid for the system with positive gold nanoparticle.

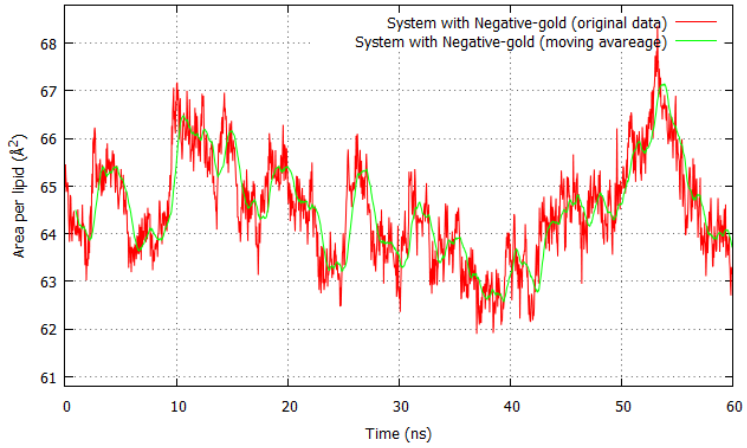

Figure 6.31: Area per lipid for the system with negative gold nanoparticle.

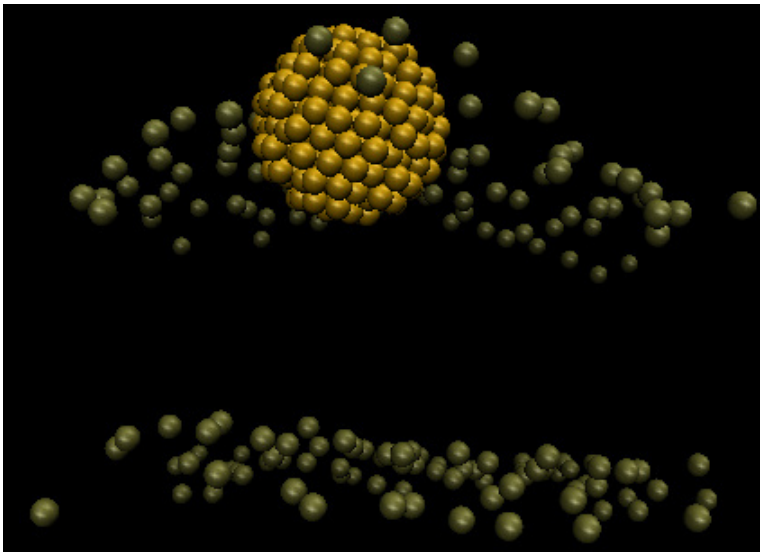

Figure 6.32: Trajectory of the neutral gold nanoparticle on the lipid bilayer surface which shows partial penetration of the AuNP by the lipid bilayer surface at 60 ns.

6.5 Constant velocity pulling of gold nanoparticles through the lipid bilayer

6.5.1 Steered molecular dynamics simulations

In order to get a better understanding of the interaction between the bilayer surface and the gold nanoparticle, the equilibrated structure of the neutral gold nanoparticle with the lipid bilayer were subjected to steered molecular dynamics (SMD) simulations. SMD is a biasing method that induces time-dependent external forces to change the biomolecular structure [120]. This allows for the study of binding and unbinding events for such systems. SMD has recently become very popular in studies of biological processes such as protein folding and unfolding, ion transportation across membrane channels, and has also provided insights into the ligand (un)binding pathway mechanisms [121]. It has also been used in determining whether the protocadherin 15-cadherin 23 bond of hair cells interface is mechanically strong [122].

In the this work, the membrane is subject to a thermodynamic (harmonic restraint) force equal and opposite to the force applied to the nanoparticle. This method has the advantage of being able to being used to investigate possible permeation pathways of nanoparticles across a lipid bilayer membrane.

6.5.2 System and method

The system of the neutral gold nanoparticle which was used in the previous section was the subject of the SMD simulations. Thus the system was placed in $80 \times 80 \times 110$ Å^3 simulation cell. The gold nanoparticle was placed geometrically at the centre of the top of bilayer. The system was kept at 300 K and pre-equilibrated for 250 ps. The nanoparticle molecule was pulled from this starting position through the lipid bilayer. Simulations were performed using the MD simulation package NAMD version 2.10. The same force fields

Table 6.4: The velocities given to the neutral AuNP

	Velocity (Å/ps)
1	-0.044
2	-0.0044
3	-0.00044

as from the previous section were used in this study. All other simulation parameters were the same as that used in the previous sections. To gather a set of samples to form an ensemble, the same target centre position was given to the nanoparticle for each applied velocity.

A difference between a set of centre of mass of gold nanoparticle and lipid bilayer membrane distance restraints were used as the pulling variable during SMD along the ξ and attached to a spring constant (10 kcal/mol/Å^2) at constant velocity. For this purpose, the moving restraint method was used and accomplished with Colvars. This meant that equal and opposite forces were applied to the nanoparticle and lipid bilayer. The simulations were performed with different pulling velocities as shown in Table 6.4 to maximize the permeation process. Note that if the applied velocity is too fast it may result in unphysical deformations of the structure and because of the lack of time for the molecule to relax in response to the applied stress may lead to unphysical results. Another reason for using low pulling velocities is that it is hard to know the magnitude of the force required to pull a nanoparticle through the lipid bilayer. So, in choosing a very low velocity gives the lipid enough time to relax. Moreover, these low pulling velocities allows the driving of a gold nanoparticle through the lipid bilayer within time frames accessible to MD simulations. For each pulling velocity, three independent SMD simulations, all with the same starting structure were carried out for 20 ns using the Colvars module with NAMD.

6.5.3 Analyzing data

To analyze the data of the constant velocity SMD simulations, we examined the force as a function of the position along the z-axis of the system. In order to achieve this, the output trajectory file was saved together with all the forces for each position as the gold nanoparticle passes through the lipid bilayer membrane.

$$\mathbf{F} = -\nabla U \tag{6.5.1}$$

$$\nabla U = \frac{1}{2}[\mathbf{vt} - (\mathbf{r} - \mathbf{r_0}).\mathbf{n}]^{\mathbf{2}} \tag{6.5.2}$$

6.5.4 Results and discussions

Song *et al* [123] carried out coarse grained MD simulations to find the minimum force required for nanoparticles to cross through lipid bilayer. They calculated the forces required for the nanoparticle to move through the first layer (first headgroup) and for when the nanoparticle leaves the lipid bialyer membrane. According to their studies, the minimum force for the first layer is less than for the second layer. We performed the SMD simulations to estimate the minimum force required to allow for a neutral gold nanoparticle to permeate through the POPC lipid bilayer membrane. First, we determined the area per lipid and the thickness of the POPC lipid bilayer membrane at different velocities and these are given in Table 6.5. It can be seen that the APL for the first two velocities are in agreement with the results of other experimental and computational investigations [32, 76]. However, for the lowest velocity in our study, the APL is much higher than the experimental value, and the thickness is much less than the actual value. This means that, the lipid bilayer membrane is not thermally relaxed and the gold nanoparticle is somehow stuck in the hydrophobic region.

Typical trajectories of the simulation after 20 ns are shown in the Figure 6.33. It is

Table 6.5: Results of the APL and BLT

Velocity (Å/ps)	thickness (Å)	Area per lipid (Å^2)
-0.044	38.7±2.2	68.4±5.9
-0.0044	38.1±4.4	69.1±9.7
-0.00044	33.1±0.5	78.8±1.6

clear that the duration of the simulation is not long enough to allow the nanoparticle to cross the lipid bilayer and to allow the lipid molecules to relax thermally after the permeation process. We have tried to determine the minimum force required for the gold nanoparticle to permeate through the lipid bilayer. However, this calculation depends on determining the minimum velocity which is difficult to find out in our case. This must be carried out by choosing a very low velocity to reach a required force to do the permeation process.

The velocity profiles at different constant velocities as a function of the z coordinate are shown Figures 6.36, 6.35, and 6.34.

6.5.5 Conclusion

One can see that for all three velocities, increasing the resistances of the headgroups toward the passing gold nanoparticle results in a decrease in its velocity. In addition, for the first two velocities considered, the velocity of the gold nanoparticle decreases more inside the hydrophobic region until it reaches the lower headgroups and then increases again when the gold nanoparticle pass cross the bilayer completely and reaches the water region. However, for the lowest velocity considered, the gold nanoparticle gets stuck in the hydrophobic region as it does not have enough time to permeate through the bilayer. Figure 6.37 shows the force profile for the different velocities considered. In general, in our case, the force required is less than 2000 pN.

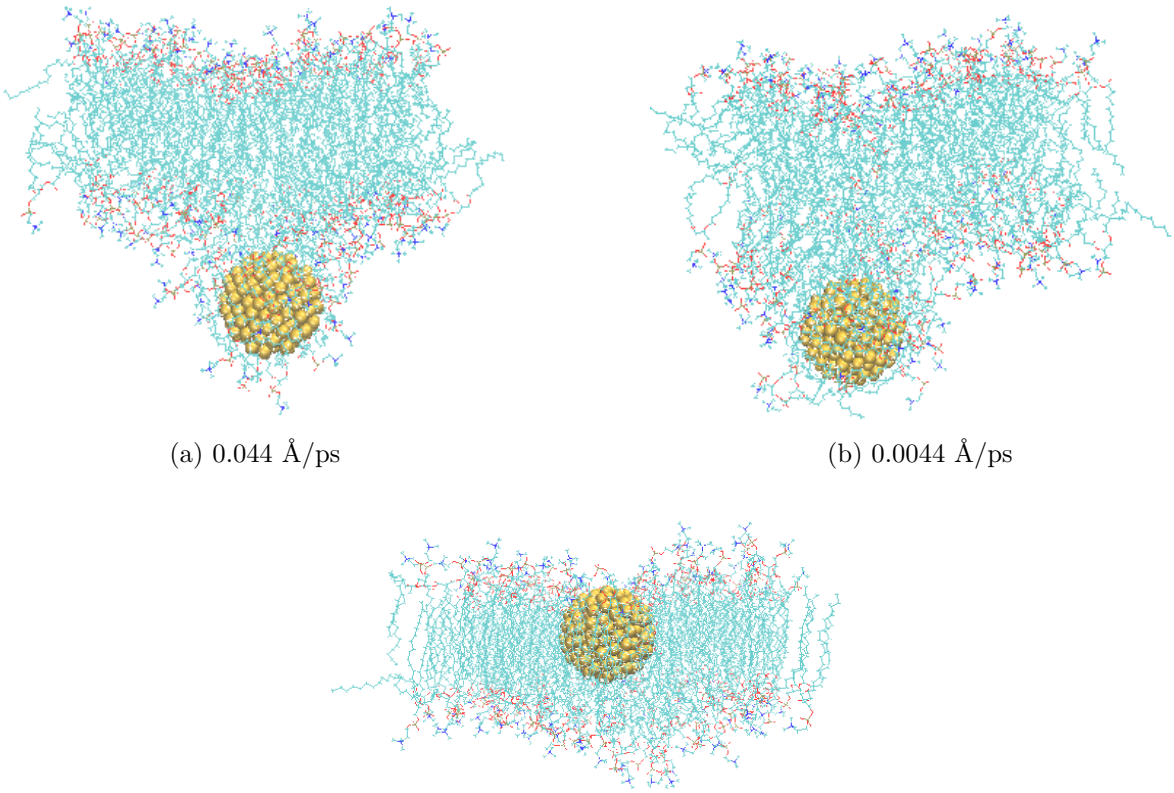

(a) 0.044 Å/ps

(b) 0.0044 Å/ps

(c) 0.00044 Å/ps

Figure 6.33: The trajectory of the AuNP after 20 ns at each constant velocity.

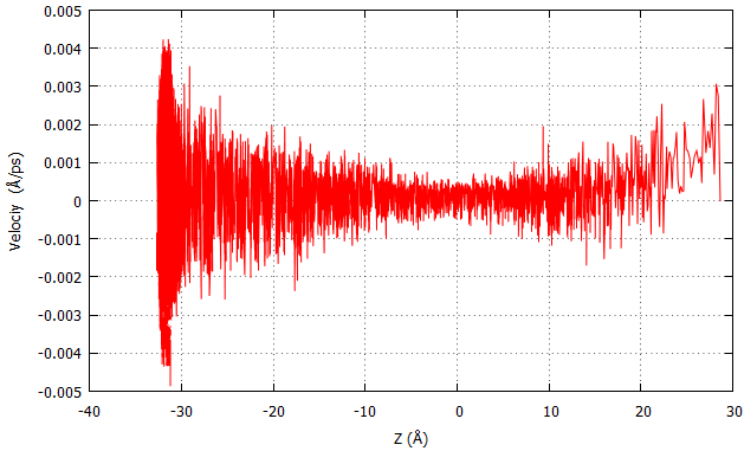

Figure 6.34: The velocity profile as a function z-coordinate when the constant velocity is 0.044 Å/ps.

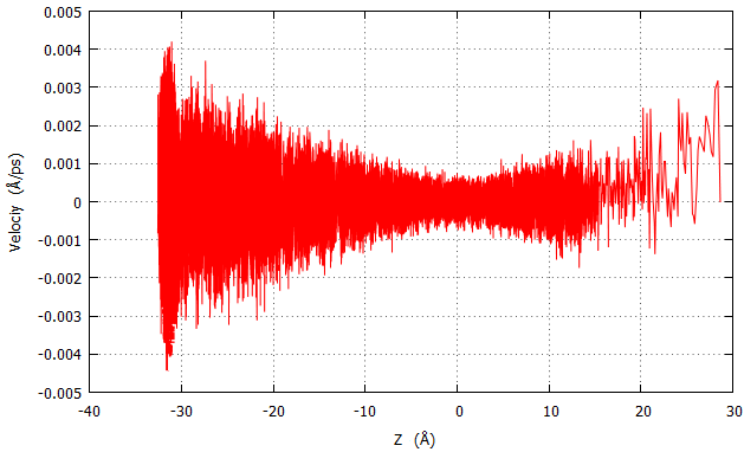

Figure 6.35: The velocity profile as a function z-coordinate when the constant velocity is 0.0044 Å/ps.

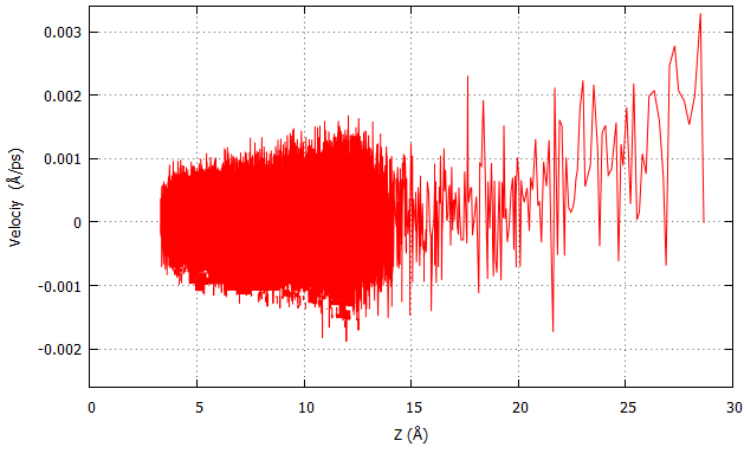

Figure 6.36: The velocity profile as a function z-coordinate when the constant velocity is 0.00044 Å/ps.

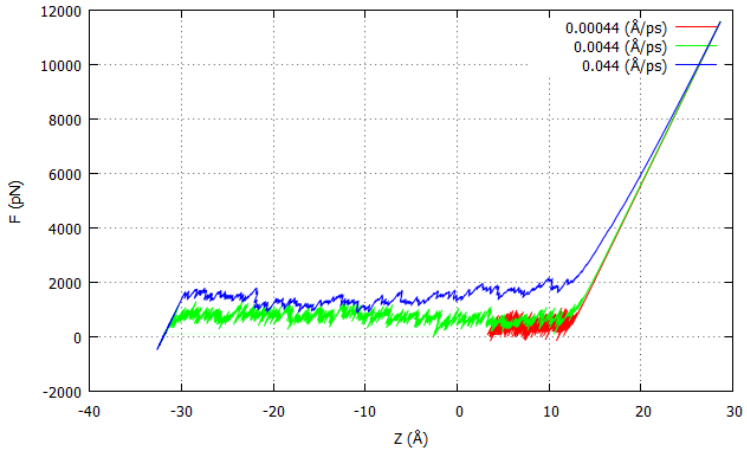

Figure 6.37: The force profile as a function z-coordinate for the different applied velocities.

Chapter 7

Coarse grained molecular dynamics simulations of the interaction a carbon nanotube with a bilayer membrane

7.1 All-atom (AA) and coarse-grained (CG) simulations of biomolecular systems

Molecular dynamics simulations are used to provide information about how large molecular systems behave when they interact with external particles or forces. In principle, simulations of this type should be on systems as large as possible and for as long as possible. In practice, however, there has to be a balance between the size of the system and approximations used in determining the total energy. This is because of the computational resources required for simulations involving many thousands of particles. Because of this, alternate strategies have been proposed.

In a coarse grained (CG) MD simulations [124], small groups of atoms are treated as single particles (beads) and the forces between these particles are derived from the interatomic forces. The effect of this is to severely reduce the number of particles in a simulation, thereby allowing for the consideration of a larger number of atoms. It has also proven to be a valuable tool to probe time and length scales of systems beyond that used in all-atom (AA) simulations. The down side of this is that the inter-particle interactions are less accurate. However, if these coarse grained particles are chosen carefully, such simulations can provide much useful information. The time and size scales for the different simulation techniques is shown in Figure 7.1.

It may also be noted that some applications do not need detailed atomistic information making them very suitable for CGMD simulations. However, using CG methods can also result in an inaccurate description of systems, including membrane systems, so CG simulations are not always recommended. There are different levels of how the coarse grains are constructed. For example, CG systems have been developed using tens or hundreds of atoms per CG bead in some studies of amino acids in biological science. By contrast, for other systems, a single CG bead is used to replace just two or three atoms.

The interaction potential between CG beads are simplified and do not include bending or torsional interactions. Electrostatic interactions are only taken into account if absolutely necessary. The important point is that CG simulations are used to provide a collective description of observed phenomena using only significant interactions. The main feature of the CG approach is that it is faster than all atom simulations. For example, in a simulation of water, 4 water molecules each comprising 3 atoms can be replaced by a single CG water bead. Additionally, the time step in the simulation can be increased by a factor of 10 or 15. So, in such a case, using a coarse grained model would result in a computational speed-up of about 100.

In this chapter, the interaction of a carbon nanotube with a lipid bilayer membrane is studied using coarse grained MD in an effort to understand the usefulness of the CGMD

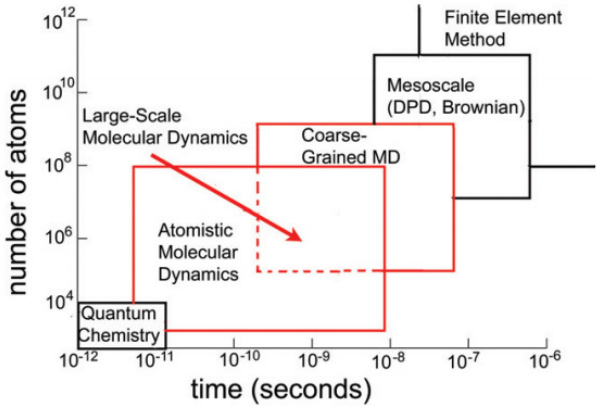

Figure 7.1: Modelling and simulation methods with associated time and length scales.

method for such simulations. First, we show that the structural information for a protein using both, all-atom (AA) and CG models, gives results that are consistent with each other. In then next section, we show the results of a test study using CGMD to model the structure of the ubiquitin protein molecule.

7.2 Equilibrium structure of the ubiquitin protein molecule

7.2.1 Introduction

Ubiquitin (UBQ) [125, 126] is a small globular protein which is found in almost all tissues of eukaryotic organisms. It consists of 76 amino acids. The structure of the UBQ based on the X-ray information is shown in figure 7.2. It shows UBQ with helices in purple and the β-sheet in blue. The turns and coils are in grey. UBQ is a key regulatory label for many different cellular processes. An example of such a process is that related to the regulation of proteins. Ubiquitin's physical and structural features make it an interesting candidate for experimental and theoretical studies of proteins. UBQ can alter its functions by the way it binds to a substrate protein which gives a number of different outputs. This

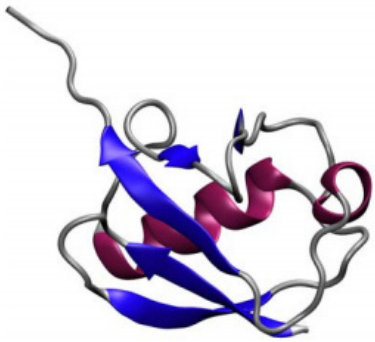

Figure 7.2: A structural view of UBQ using VMD.

process is called ubiquitination or ubiquitylation and can be affect the protein's activity, location and in the way it interacts with the other proteins. Modelling these activities has also became a major goal of research in the area of computer simulations.

In this section, the results of carrying out both, AAMD and CGMD simulations on the equilibrium structure of UBQ is reported. The purpose of this is to test the usefulness of CGMD by comparing both sets of results to see whether they are consistent with each other.

First, the equilibrium configuration of UBQ is determined by carrying out AAMD simulations. This structure was used as the initial state for the CGMD simulations. Finally, the structure resulting from the CGMD simulations was reversed back to give the atomic configuration of the molecule using the reverse coarse-graining (RCG) method [127]. This process allows us to characterize the structures obtained from a multimicrosecond CGMD simulation as well that obtained from higher resolution AAMD simulations. By comparing the results of both models, CGMD is shown to provide structural information of proteins that is consistent with that of AAMD. The comparison of the CPU (Central Processing Unit) times for both simulations are also presented.

7.2.2 Simulations

Both, the AAMD and CGMD simulations of the equilibrium properties of UBQ were carried out using NAMD. The UBQ protein structure used in this study was downloaded from the Protein Data Bank (PDB) [128].

In both sets of simulations the UBQ molecule was placed at the centre of the $60 \times 60 \times 66$ Å^3 simulation box and solvated with water using the Solvate plugin of VMD as shown in the Figure 7.3. Three dimensional periodic boundary conditions were applied. The structure with the bead positions used in the CG study was derived from all atom coordinates of protein using the Martini model [33] to define the interaction sites.

Both sets of simulations were carried out at a constant temperature of 300 K using Langevin dynamics with a Langevin damping coefficient of 1 ps^{-1}. Isotropic pressure of 1 bar was applied using a modified Nose-Hoover method. The details of the simulations are given in Table 7.1. The CHARMM27 force field [2, 129] parametrization was taken in the AAMD simulations whereas parametrization by MARTINI [33] was used to represent the bead interactions in the CGMD simulations. The calculation of non-bonded interactions is the most time consuming part of the MD simulations, so a 12 Å cutoff was applied for the van der Waals and short-range interactions. A switching function at 10 Å was added for the van der Waals interactions in order to ensure a smooth cutoff. For the long-range interactions such as electrostatic interactions, the particle-mesh Ewald (PME) method was used with a grid point density of over 1.2/ Å^3. In both sets of simulations, the energy of the system was minimized first by applying the conjugate gradient algorithm for 1000 time steps and then equilibrated at 300 K for a period of time in an NPT ensemble. The simulations were first tested on a single machine (8 core-processor) and the final calculations were carried out on the 32 core parallel computers using the computational facilities of the Advanced Research Computing@Cardiff (ARCCA) Division, Cardiff University.

Table 7.1: Simulation details

	AAMD	CGMD
number of UBQ particles	1231 atoms	163 beads
number of water particles	7392 molecules	1496 beads
total number of particles	23407 atoms	1659 beads
time step	2 fs	10 fs
damping timescale	200 fs	2000 fs
period of simulation	8 ns	6.3 ns

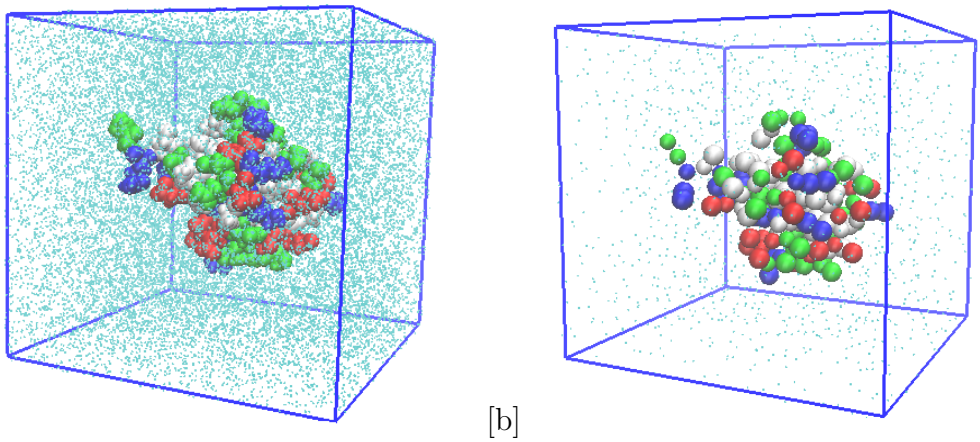

[a] [b]

Figure 7.3: The structures of the UBQ protein in the systems of : a) AA b) CG simulations.

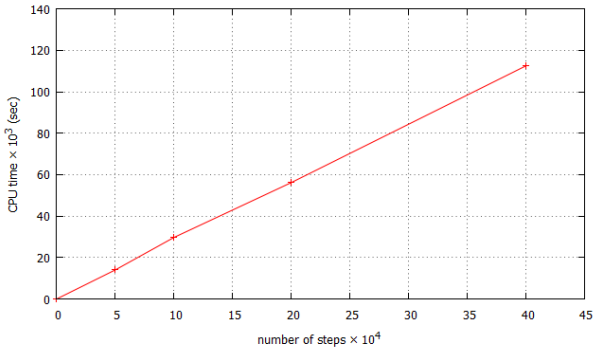

Figure 7.4: CPU time as function of number of steps in AAMD simulation for UBQ on single machine.

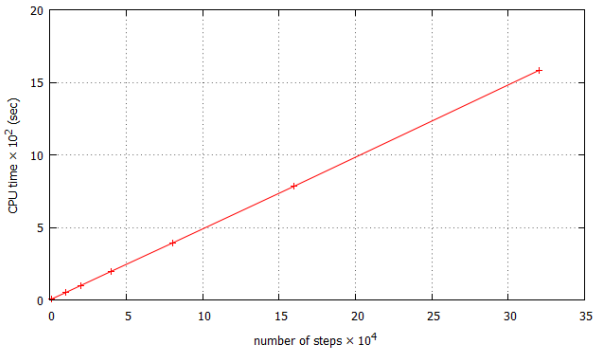

Figure 7.5: CPU time as function of number of steps in CGMD simulation for UBQ on single machine.

7.3 Results and discussions

The CPU time taken, as a function of number of steps, for both sets of simulations is shown in Figures 7.4 and 7.5. It can be seen that CGMD is faster than the AAMD simulations by about a factor of 60. In Figure 7.6 is shown the speed up as the number of nodes on the parallel machine is increased.

It is clear that the AAMD processing times improves markedly with increasing nodes. The time taken for the CGMD simulations makes it feasible to carry out preliminary calculations before embarking on a full AAMD simulation. Also, in some cases, the latter may be prohibitively expensive. In such cases, CGMD is the only viable option.

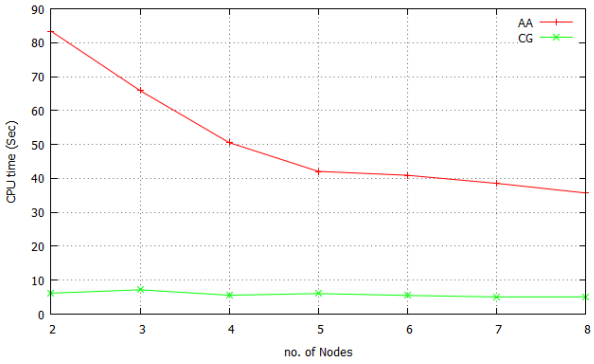

Figure 7.6: CPU time as function of number of nodes in both AAMD and CGMD simulation for UBQ on Raven cluster.

In order to compare the equilibrium structures resulting from both sets of simulations, we calculated the time variation of the root mean square deviation (RMSD) of the system. The RMSD is defined as a summation of the square distances between each atom in one structure and the corresponding atom in another structure. This is a numerical measure of the difference between the two structures which is defined by the following equations.

$$RMSD_\alpha = \sqrt{\frac{\sum_{\alpha=1}^{N_\alpha} |\mathbf{r}_\alpha(t_j) - \langle \mathbf{r}_\alpha \rangle|^2}{N_\alpha}} \tag{7.3.1}$$

Then, $\langle \mathbf{r}_\alpha \rangle$ is defined as follows:

$$\langle \mathbf{r}_\alpha \rangle = \frac{1}{N_t} \sum_{j=1}^{N_t} \mathbf{r}_\alpha(t_j) \tag{7.3.2}$$

where N_α is the number of atoms whose positions are being compared, N_t is the number of time steps over which atomic positions are being compared. $\mathbf{r}_\alpha(t_j)$ is the instantaneous position of atom α at time t_j, and $\langle \mathbf{r}_\alpha \rangle$ is the time-average value of the position of atom α to which the positions $\mathbf{r}_\alpha(t_j)$ are being compared. This measure can be used to analyse the stability of the molecule. So, if the RMSD decreases in time or deviates around a small value, it suggests that the molecule is in a stable phase. If however, the RMSD

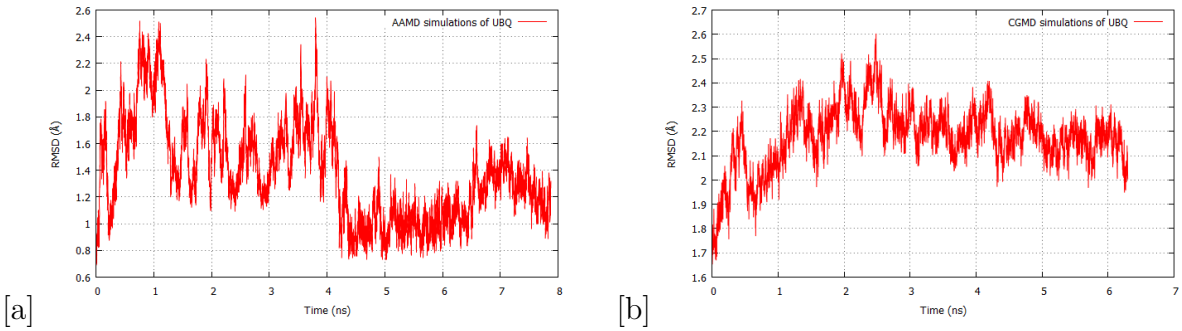

Figure 7.7: The RMSD of UBQ protein as a function of time in the: a) AA b) CG simulations.

keeps increasing, it points to an unstable structure. The RMSD values as a function of time for both sets of simulations are shown in Figure 7.7. These results indicate that both the AAMD and CGMD results in stable structures of UBQ.

The next phase was to compare the two structures in atomic detail. To do this, the RCG plugin in VMD was used to recover the atomic positions of the atoms from the bead coordinates in the CG system. This atomic configuration was then energy-minimized. Then, both sets of atomic coordinates, the original and those obtained after the reverse back, were compared. While the RMSD value of the molecule as a whole is very useful in itself, it is important to have an overview of flexible regions in protein from the thermal motion of each residue. The root mean square fluctuation (RMSF) is a time average of the RMSD per residue, as a function of the residue number. The RMSF was then calculated using the original structure as a reference as shown in the Figure 7.8.

If the RMSD value is large, the structures are dissimilar, while if it is zero means they have identical configurations. However, if the number is intermediate it suggests some similarity, as root mean square deviation is roughly related to RMSD in interatomic distances and both structures must have the same general fold. Proteins usually have well defined 3D structures compared to other polymers and have secondary structures and tertiary structures. The RMSD is always determined relative to some reference structure. The reference structure is fit to the other structure using a “measure fit”. A 1 - 2 Å RMSD

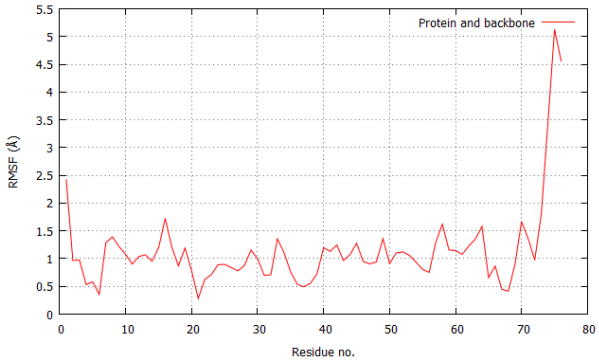

Figure 7.8: RMSF of protein and backbone with respect to the average coordinates of both simulations.

Table 7.2: Residue numbers for AAMD and CGMD systems of the UBQ.

Systems	No. of α helix	No. of β sheet	Total
1. AA	12 residues	27 residues	39 residues
2. CG	12 residues	26 residues	38 residues

value is perfectly allowable and expected for small, globular proteins [130].

Other than RMSD calculations we have also looked at the secondary structure because it is important to know if the transformation of the atoms to beads and back again has affected the characterization of the protein. We have therefore calculated, for both structures, the number of residues in the α helix and in the β sheet and this is presented in the table 7.2. It is clear that the transformation process has resulted in one residue missing. The resultant structures shown Figure 7.9 indicates that:

1. The CGMD simulations result in structures that are nearly the same as found by AAMD;

2. The transformation process and its reverse taking atoms to beads and vice versa is quite robust.

Having thus established that CGMD is a useful tool to use in systems too large to be studied using AAMD or for simulations which need to be run over very large time scales

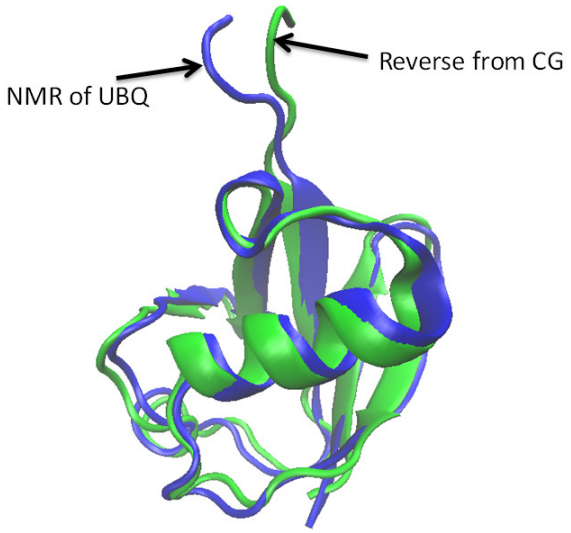

Figure 7.9: Structure UBQ from NMR and reverse back from CG simulation.

(up to 1 ms). We now report on the results obtained by using CGMD to investigate the interaction of a POPC lipid bilayer with a carbon nanotube.

7.4 Simulation studies of the interaction of a POPC lipid membrane bilayer with a carbon nanotube (CNT)

7.4.1 Introduction

The importance of the study of gold nanoparticles and their interaction with biological molecules with particular reference to medical, biological, and nanomaterial applications was mentioned in the previous chapter. In general, there has been much interest in studying nanoparticles in biological environments. Particular interest has focussed on incorporating carbon nanotubes in biological applications.

In this section, we report on our investigations studying the interactions between a

carbon nanotube (CNT) and a lipid bilayer membrane using CGMD simulations. The interactions between lipid bilayers and carbon nanotubes have been studied by computational methods by many researchers [131–133]. This has been in the context of developing nano-injectors for drug delivery and gene therapy into cells and for building novel biomaterials [134]. The penetration of a carbon nanotube into biomolecular cells such as a lipid membrane have been confirmed experimentally, although the mechanism of how they pass through cells still is not well understood [135–138]. As carbon nanotubes have unique properties, they have also been used in other nanotechnology applications such as nano-electric devices, nanowires and to build tiny transistors [18, 139, 140].

It has been reported in AA simulations, using SMD, that open-ended single-walled carbon nanotubes penetrate into a membrane and in so doing, destroy the structure of the lipid bilayer . However, it has also been found that capped single-walled carbon nanotubes causes less destruction of the lipid structure while it has a lower free energy barrier [141]. The impact of a carbon nanotube on the structure of a cholesterol molecule on a protein has been investigated where it was found that it forms a layer around the protein [142]. The stabilization of CNT inside the lipid bilayer POPC and POPE have been investigated by [131] who found that the temperature is not affected on the insertion of carbon nanotube as they calculated RMSD at different temperatures and obtained RMSDs more or less at the same level.

Membrane bilayers can be supported by carbon nanotubes in order to increase its structural stability to make for a mechanically strong surface. Carbon nanotubes can penetrate inside mammalian cells without any external help or can be inserted manually into a lipid membrane. Nevertheless, intercalcated carbon nanotubes on a lipid membrane are not yet realizable. Because of this, the interaction between CNT and lipid membranes is a growing area of interest. The complex structure of lipid membranes and its fluidity makes experiments at a molecular or cellular level intensely challenging. Thus, understanding the interactions between them has been investigated by molecular simulations.

To better understand the interaction processes, a carbon nanotube, a lipid membrane, and surrounding environment are needed. In this work, a classical CGMD simulation has been used to focus on the stability of carbon nanotubes within a membrane by using the RMSD to measure the stability.

The present study examines the energy optimization of the complex system consists of a carbon nanotube and a POPC membrane in water solution. MD simulations were carried out using the NAMD package. Also, the investigation sets out to determine the RMSD, the force between lipid bilayer with CNT throughout the simulations, and the tilt angles of carbon nanotube with respect to the normal axis of bilayer. Furthermore, the data is analyzed by VMD to confirm the structural changes during MD simulations at finite temperatures. The main purpose of these investigations is to obtain an understanding of the interaction of a CNT with POPC lipid membrane.

7.4.2 System and computational method

In this work, classical CGMD simulations of a system comprising a POPC lipid membrane bilayer and a CNT all solvated in water at 300 K, were carried out. To build the (POPC) membrane bilayer with size (50 × 50 Å), VMD has been used. VMD automatically builds a water shell around the lipids in order to properly hydrate the lipid headgroups. The Martini model was used to make the CG interaction sites of the POPC bilayer [143], with an approximate 4:1 mapping. The beads or particles in the CG structure were associated with polarity, hydrophobicity, and charge. They are assigned particle types as (e.g. P_1, P_2, C_1, C_2, Q_a, Q_d, ..etc) and interact with each other via the non-bonded potential functions. The bonded interactions were treated in the same approach used in atomistic simulations. Figure 7.10 shows an example of the resulting Martini-designed CG lipid. The water molecules were mapped as 4 water molecules to 1 CG particle. These particles were assigned a P_4 type as explained in [33]. VMD was also used to build a zigzag (10, 0) carbon nanotube (CNT) with a diameter (7.82 Å) with a

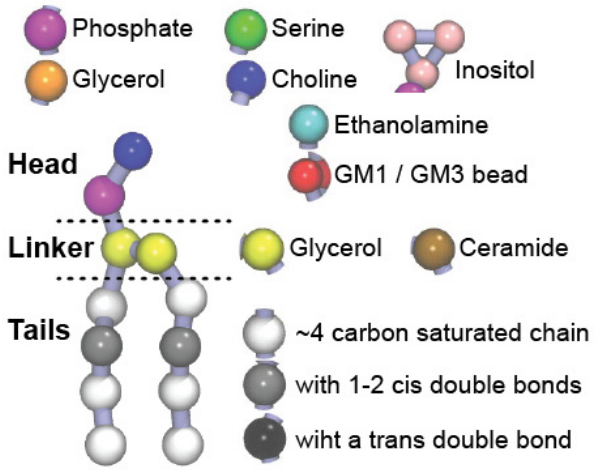

Figure 7.10: Martini lipid layout.

relatively short length of 30 Å. The CNT comprised 320 atoms, 470 bonds, 920 angles, and 1800 dihedrals. Then, in order to construct the CG CNT structure, 4 carbon atoms were mapped onto 1 CG bead, as shown in the Figure 7.11. The CG CNT structure then comprised 80 particles bonded together through the harmonic potential with a force constant of 5.9752 kcal mol^{-1} $Å^{-2}$ to sustain the geometry of the nanotube. In this study, apolar (C) [33] particle types were used to describe the carbon atoms with hydrophobic properties based on the study by Wallace [144, 145]. Parameters for the MARTINI force field [33] as applied to the CG CNT were taken from [146, 147]. To construct the final combined system, the CNT was manually placed into the center of the POPC bilayer using VMD.

Initially, an energy minimization (optimization) was carried out to optimize the structure for 2000 time steps. This was to ensure that any clashes between particles were removed. After this, the system was run for 300 ns with a times step of 10 fs (ie, 3×10^8 steps). The MD simulations was performed in the NPT ensemble at temperature of 300 K and Langevin Dynamics was used to control the temperature. The pressure was set at 1.01325 bar. The cutoff distance for all non-bonding atom interactions was set to 12 Å. Periodic boundary conditions were applied. The edges of simulation cell had dimensions

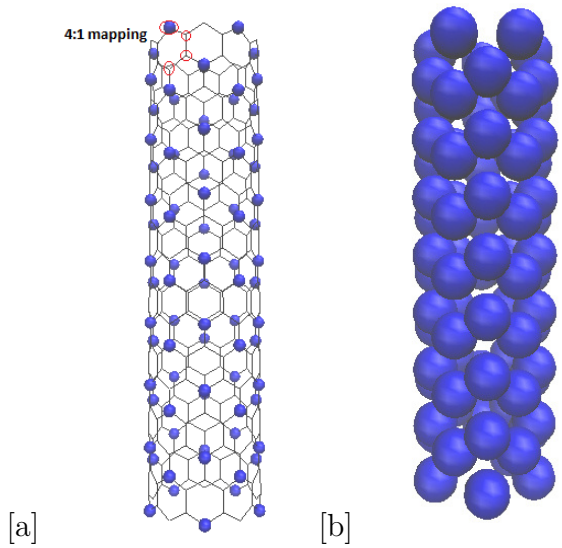

Figure 7.11: The schematic structure of CG carbon nanotube 4:1 mapping: a) the blue circles represent 4 atoms per bead as assigned by red circles b) VDW viewing.

$x = 50.0$, $y = 50.0$, $z = 93.0$ Å. Finally, the results of the simulation were analyzed using VMD.

7.4.3 Results and discussion

The CGMD simulations of the system consisting of the membrane (POPC) and a single CNT in a CG water solution were carried on the initial structure as shown in Figure 7.12. As mentioned above, this structure was first allowed to relax and minimize its energy in order to remove any steric interactions between the particles. Then, MD simulations were carried out on the system which was kept at 300 K for 300 ns using time step of 10 fs. In Figure 7.13 is shown the average temperature of the system during the simulation run. As can be seen, the temperature is stable around the initial temperature of 300 K.

The structure of the molecules at five different time steps during the course of the simulation are shown in the Figure 7.14. It can be seen that the impact between biological

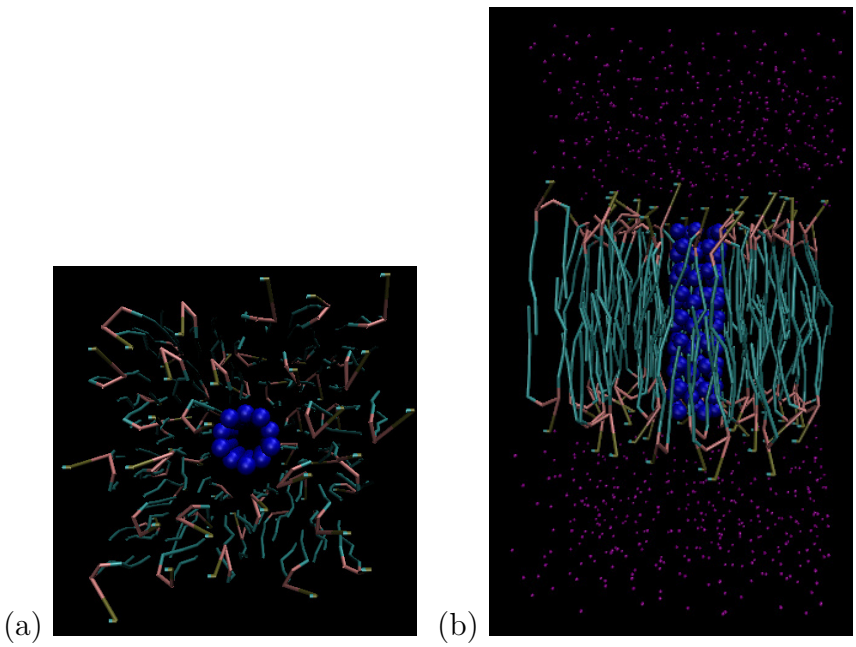

Figure 7.12: A system representation of the CG lipid membrane with CG carbon nanotube all solvated in CG water: (a) top view without water; (b) side view all the system.

membrane and carbon nanotube results in an initial movement of the latter. After 5 ns into the simulation, the CNT is seen to move and tilt away from its vertical starting position. However, this does not affect the stability of the CNT in the bilayer. Instead of forcing itself out, the CNT does remain intact within the membrane. That the CNT was stable in the membrane for the remainder of the simulation suggests that it could be used for drug delivery as suggested by other researchers [145, 148].

It is also of interest to see what happens to the the thickness of the lipid bilayer. Because the temperature of the simulation was set to be 300 K, any increase in energy resulting from the initial placement of the CNT could lead to a local melting of bilayer. If so, this could be manifest in the thickness measurement. The initial thickness of the lipid bilayer was taken to be 35.51 $\pm$ 0.40 Å which is agreement with the experimental values of Kuerka *et al* [76] and consistent with the value used in other MD simulations [149]. The varying thickness with MD simulation time is shown in the Figure 7.15.

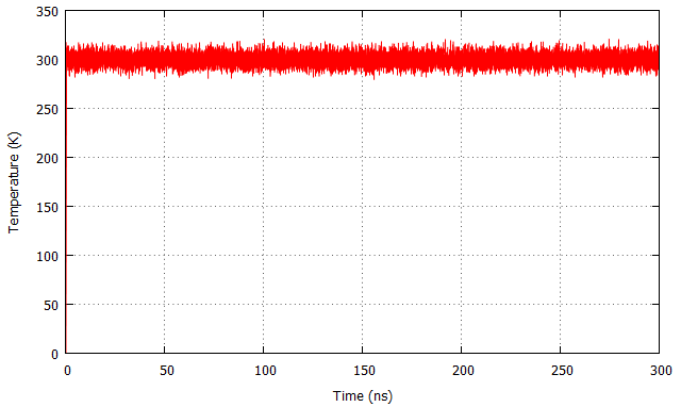

Figure 7.13: Temperature of the system of CNT with POPC during 300 ns of simulation.

In order to further analyse the structures of both the lipid bilayer and the CNT during simulations, the RMSD between the structure at 300 ns and the initial structures was calculated. In Figures 7.16 and 7.17 are shown the RMSD values for both the CNT and the POPC membrane as a function of time.

The RMSD value of the CNT is consistent with the view that it is quite stable throughout the simulation without any loss of structural integrity. However, this is not the case for the POPC membrane. Here, the RMSD values indicate that the structure is relatively stable until 150 ns and then the RMSD is increasing until 200 ns. Also, at 200 ns, there is a jump in the RMSD values after which, the bilayer regains its stability. Part of the reason for this fluctuation could be attributed to the effect of the periodic boundary conditions. The RMSD values are used to determine whether a structure is in a stable phase at a particular temperature or not, It could also be used as a means to measure structural damage as in the case of protein docking [150].

We have also determined the RMSF which as mentioned earlier gives information on the relative stability of the residues. From Figure 7.18 of the RMSF of the CNT, we note that the fluctuation of the carbon particles in the middle of the CNT structure are more stable than those near the headgroup of the lipids. This can be understood by noting that the type of the carbon particles (hydrophobic) interacts strongly with the hydrophilic

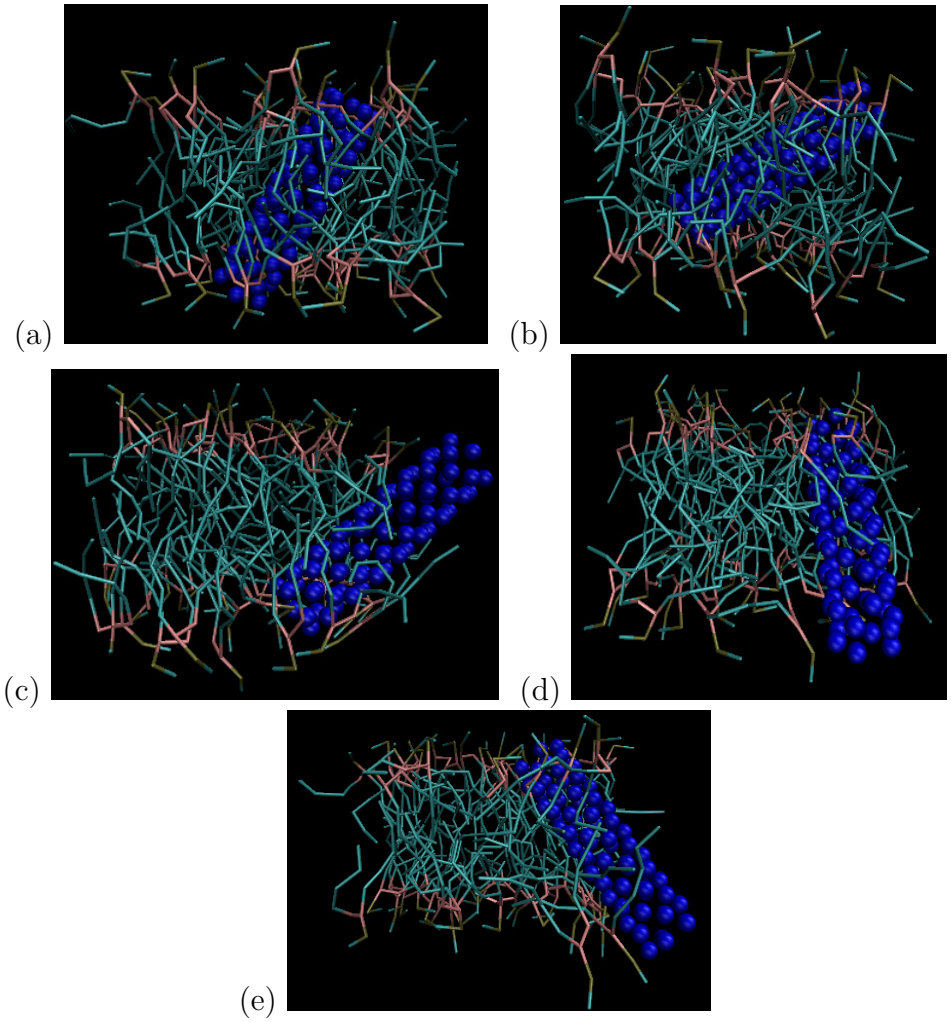

Figure 7.14: Visualization of the CG membrane (POPC) and the CG carbon nanotube (CNT) during different times of MD simulation: (a) 5 ns; (b) 25 ns; (c) 50 ns; (d) 200 ns; and (e) 300 ns. Picture created using VMD.

headgroup. This results in those carbon particles having the highest values of the RMSF.

To get a better understanding of the interaction between the POPC lipid bilayer and CNT, we calculated the force between CNT particles and the lipid bilayer membrane at all three principal directions, as shown in the figure 7.19. It should be explained that the force acting on CNT on each side are nearly similar and fluctuates between (40, -40) kcal.mol^{-1} Å^{-1}. This is because of the upper and lower leaflets of the lipids interact with

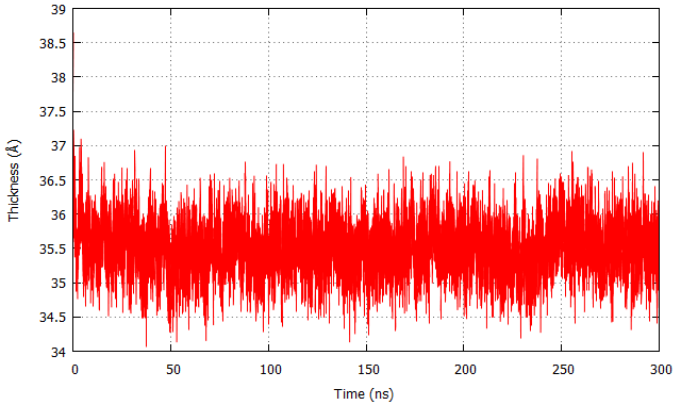

Figure 7.15: The thickness of the POPC lipid bilayer during simulations.

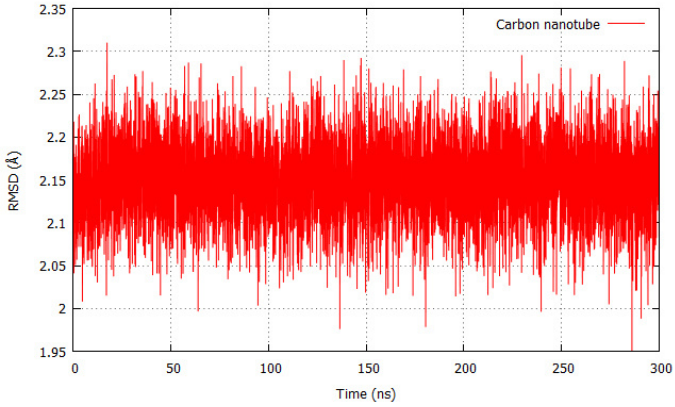

Figure 7.16: The RMSD value of the CNT at 300 K during 300 ns evolution time.

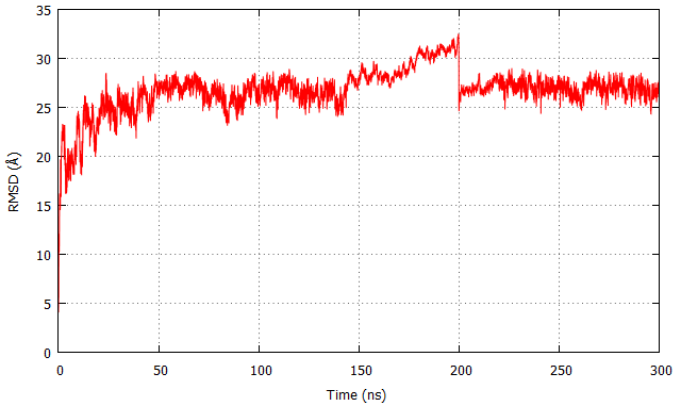

Figure 7.17: The RMSD value of the POPC at 300 K during 300 ns evolution time.

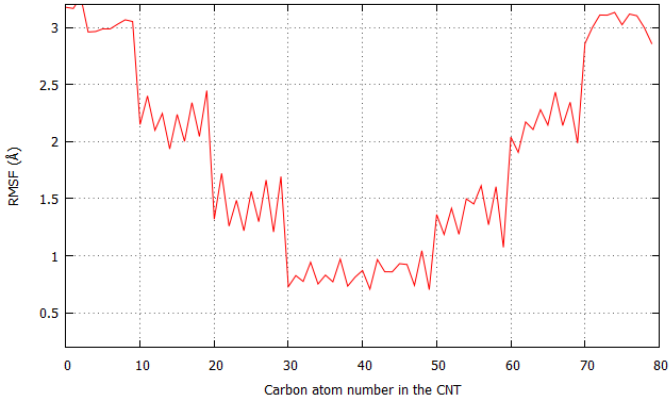

Figure 7.18: The RMSF of the CNT atoms at 300 K during 300 ns evolution time.

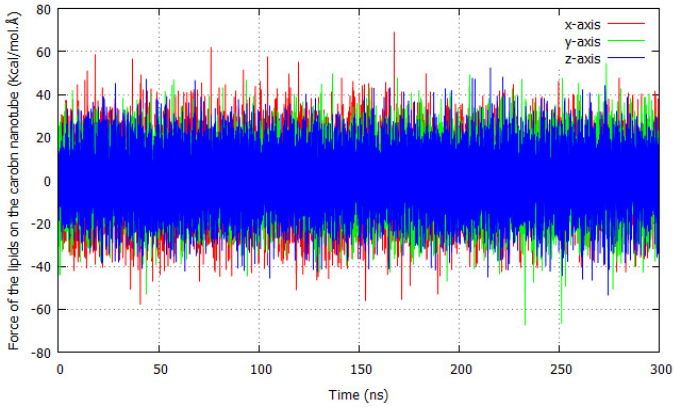

Figure 7.19: The force of the lipids on the nanotube at three axis during 300 ns evolution time.

the CNT equally. These calculations were carried out using a Lennard-Jones interparticle potential.

The tilt angle between the CNT and the normal axis of lipid bilayer membrane has also been calculated and as shown in the Figure 7.20. We see that there are oscillations of the CNT around 50 angle.

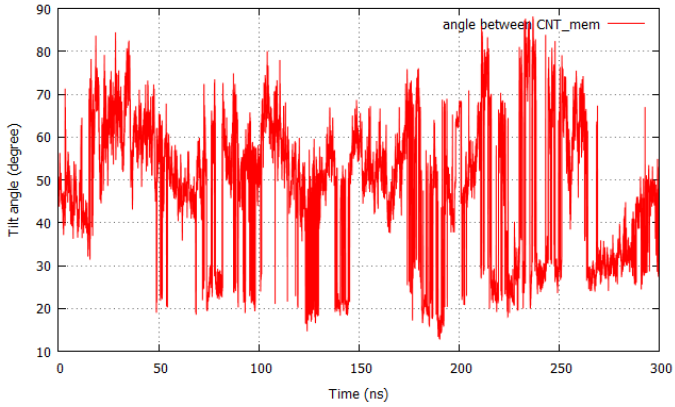

Figure 7.20: The tilt angle between carbon nanotube and the normal axis lipid membrane (z) during 300 ns evolution time.

7.5 Conclusion

We have used both AAMD and CGMD to simulate UBQ protein. A comparison of the results in structures are similar enough to give confidence that CGMD is a useful tool in carrying out simulations of large bio-molecular systems. Based on the results of the UBQ protein, it is clear that CGMD is computationally much faster than AAMD. Our preliminary studies of the interaction of a CNT with a lipid bilayer points indicates that such nano-tubes inserted into a membrane could be stable. This means that it could be used as an agent in the delivery of drugs. It would be good if these simulations could be repeated using AA simulations to confirm the validity of these results.

Chapter 8

Conclusion

There has been some interest in integrating lipid bilayer membrane for designing a new devices in many applications such as modern science and nanomedicine [3]. Studying the permeabilities of lipid bilayer membranes has also attracted much interest in order to understand targetted drug delivery in bio-medical applications. The toxicity of nanoparticles and the possible dangers associated with these nanoparticles entering cells has meant that this is another topic of concern to the general public. For all these reasons, understanding the physics and chemistry of lipid bilayer membanes is of paramount importance. During this project, four aspects of these membranes have been studied. The integrity and robustness of membranes were investigated by a calculation of their elastic properties with and without defects. Then, the factors that influence the diffusion of ions, atoms and molecules across the a membrane were studied. This was followed by a detailed analysis of how gold nanoparticles interacted with these bilayers. Finally, in an effort to look forward to carrying out very large scale simulations, a coarse-grained molecular dynamics simulation was carried out on a system comprising a carbon nanotube and a lipid bilayer membrane.

In Chapter 4, AAMD simulations using NAMD package were performed to calculate the elastic constants of the POPC bilayer using CHARMM36 force fields. We have applied

the homogenous deformation method to determine the change in energy as a bilayer is put under strain. This together with studying the effect of creating defects in the bilayer allows us to study the stability of the bilayer. Interestingly, single leaflet removal appears to affect the integrity of the bilayer and results in any major change in their elastic properties. The accuracy of our calculations has been tested by comparing the values of the calculated bulk moduli of lipid bilayers with experimental data.

In Chapter 5, permeation particles through the POPC bilayer was investigated in much detail. The first task was to find the diffusion coefficient of ions through POPC lipid bilayer using different configurations. One of the configurations was a membrane surrounded by water which had one ion just below the headgroup of the lipid molecule. We found that while the Na ions bonded to the phosphate group, the Cl ions did not bind to either the phosphate groups or the choline groups at the surface. In addition, for the other configurations when the lipid bilayer POPC was surrounded by an aqueous solution, the results confirm that Na ions are bound deep down below the surface and stayed there for a period of time.

In all our simulations, there was no permeation of ions when the concentration of NaCl on either side of a single membrane in the simulation cell was different or equal. In order to properly model the effect of having different solutions on either side of a membrane, further investigation were performed by constructing a system of two bilayers separated by different solutions in the simulation cell. Then these solutions were made to be asymmetric, one with weak charge imbalance and the other with strong charge imbalance. In the case of weak charge imbalance, while the ions (particularly the Na ion) appeared to show a tendency to diffuse across the lipid bilayer, permeation did not occur over the duration of the simulation. By contrast, when the charge imbalance was quite strong, the ions diffused through the lipid membrane across what appeared to be a pore until the solutions on either side of the membrane became near neutral. These results are in qualitative agreement with those of other researchers. By calculating the

diffusion coefficients, we were able to establish that the ions diffused more rapidly across the pores than water molecules. Interestingly, we found although the Na ions were the first to begin to move through the pore due to their lower potential barrier, the Cl ions have faster diffusion rates. The diffusion coefficients of the water molecules was less than that of the ions but were still larger by factor of five than the self-diffusion coefficient of these molecules in bulk water.

The study of the interaction of gold nanoparticles with a membrane surface is important in order to obtain an understanding of the first step in the translocation process. This is because gold nanoparticles beyond a certain sizes are not able to cross the bilayer membrane unless they are taken by an endocytosis pathway [106]. Our investigations of gold nanoparticles with a diameter of 2.2 nm adsorbed on the POPC lipid bilayer membrane forms the content of Chapter 6. In this study the differently charged nanoparticles were placed at different sites on the surface in order to determine the importance of these variables. In addition, two different temperatures were considered. We found that the results suggested that interaction between nanoparticle with the surface bilayer is greater for the neutral gold nanopartilce than the charged ones. Moreover, the positively charged gold nanoparticles tend to bind deep down to the phosphate group. However, the negatively charged AuNPs do not do so. To better evaluate the energies associated with these adsorption sites, free energy calculations which take into account entropy effects were performed. The initial results suggest that again the neutral gold nanoparticles partially penetrate the headgroups while the charged ones do not. However, the charged nanoparticles bind to the surface according to the headgroups charge carriers. The negative AuNP bind to the choline groups which they are positive carriers while positive AuNP bind to the phosphate groups which are negative carriers. Unfortunately, the potential mean force convergence was not fully achieved for these calculations and more work needs to done before we are able to obtain accurate free energies associated with the three systems. Coupled with this study, we carried out SMD simulations and were able to show that it is

possible to pull AuNPs of this size across the membrane. This has great implications, but again, further investigations need to be carried out to determine the minimum velocity (or force) required for the permeation process. These calculations are computationally intensive and should provide the basis for a detailed study into toxicological investigations of the effect of nanoparticle impact on living cells.

Finally, in Chapter 7 we have performed CG MD simulation for the biomolecular systems with nanoparticles. In order to ensure the results are similar with AAMD simulations, first we have performed AA and CG simulations of UBQ protein. The agreement between both sets of simulations give confidence that CGMD is a useful methodology to apply for such biological systems. Hence, we have the confidence to use CGMD instead of AAMD in simulations of very large systems because they are faster than AAMD and computationally cheap. We then applied CGMD to simulate the interaction of a carbon nanotube with the POPC lipid bilayer membrane. We found that such carbon nanotubes inserted into a membrane could be stable which means that they could be used in nanomedicine application such as an agent in the delivery of drugs.

8.1 Future plans

This thesis has demonstrated the usefulness of MD simulations in studying the diffusion of particles through lipids and the adsorption sites of gold nanoparticles on the surface of a lipid bilayer membrane. There are many opportunities in several different directions for extending the work reported in this thesis. In particular, as has already been stated, the investigations of the the adsorption of gold nanoparticles on the surface of the lipid bilayer needs to be further explored. The free energy calculations are computationally expensive and perhaps it might be useful to investigate other approaches for determining the free energy of these systesm. Once this is done, it could give us a better understanding of the binding the nanoparticles through the lipid bilayer surfaces and allow better analysis of

the existing results. Also in the section of SMD studies, more work is needed to produce data that could be used to determine the minimum velocity required for the translocation of gold nanopartilce across membrane layers.

The work described in Chapter 7 to investigate the stability of carbon nanotube inside the bilayer membrane using CGMD simulations is at a very preliminary stage. We have but shown the usefulness of applying CGMD to these types of systems. However this needs further investigations including carrying out AAMD simulation for very long time periods (nearly 300 ns).

Bibliography

[1] Chris Oostenbrink, Alessandra Villa, Alan E Mark, and Wilfred F Van Gunsteren. A biomolecular force field based on the free enthalpy of hydration and solvation: The GROMOS force-field parameter sets 53A5 and 53A6. *Journal of Computational Chemistry*, 25(13):1656–1676, 2004.

[2] Petia Zvezdanova Gatzeva-topalova, Lisa Rosa Warner, Arthur Pardi, and Marcelo Carlos. CHARMM General Force Field (CGenFF): A force field for drug-like molecules compatible with the CHARMM all-atom additive biological force fields. *Journal of Computational Chemistry*, 18(11):1492–1501, 2011.

[3] Edina C Wang and Andrew Z Wang. Nanoparticles and Their Applications in Cell and molecular biology. *Integr. Biol*, 6(1):9–26, 2015.

[4] Horacio Poblete, Anirudh Agarwal, Suma S Thomas, Cornelia Bohne, Ranjithkumar Ravichandran, Jaywant Phospase, Jeffrey Comer, and Emilio I Alarcon. New Insights into Peptide-Silver Nanoparticle Interaction: Deciphering the Role of Cysteine and Lysine in the Peptide Sequence. *Langmuir*, 32(1):265–273, 2016.

[5] G Karp. *Cell and Molecular Biology: Concepts and Experiments*. John Wiley & Sons, 2009.

[6] Mitchnick M D Mark, Robert Lee, Bob Becker, Bruce Frank, Garry Gwozdz, Laurie

Goldman, and Judith Cohen. Protein Structure. *Particle Sciences - Drugs development services*, 8:1–2, 2009.

[7] P L Yeagle. *The Structure of Biological Membranes, Third Edition.* Taylor & Francis, 2011.

[8] Bernard S Brown. Biological membranes. *Biochemical Society*, pages 1–49, 2001.

[9] A Benedetto, R J Bingham, and P Ballone. Structure and dynamics of POPC bilayers in water solutions of room temperature ionic liquids. *J Chem Phys*, 142(12):124706, 2015.

[10] Richard Randel, Hannah C Loebl, and Clarence C Matthai. Molecular dynamics simulations of polymer translocations. *Macromolecular Theory and Simulations*, 13(5):387–391, 2004.

[11] H Loebl and C Matthai. Simulation studies of protein translocation in mitochondria. *Physica A: Statistical Mechanics and its Applications*, 342(3-4):612–622, 2004.

[12] G Plopper, S.L.A.R.S.B.A.H.G. Plopper, D Sharp, and E Sikorski. *Lewin's Cells.* Jones & Bartlett Learning, LLC, 2013.

[13] Anders Wallqvist and Raymond D Mountain. Molecular Models of Water: Derivation and Description. *Reviews in Computational Chemistry*, 13:183–247, 2007.

[14] D Ratner M Ratner. *Nanotechnology: A Gentle Introduction To The Next Big Idea.* Pearson Education, 2003.

[15] D Patrick O'Neal, Leon R Hirsch, Naomi J Halas, J Donald Payne, and Jennifer L West. Photo-thermal tumor ablation in mice using near infrared-absorbing nanoparticles. *Cancer Letters*, 209(2):171–176, 2004.

[16] John Turkevich, Peter C Stevenson, and J Hillier. A Study of the Nucleation and Growth Processes in the Synthesis of Colloidal Gold. *Discussions of the Faraday Society*, 11(c):55–75, 1951.

[17] Xiaohua Huang and Mostafa A El-Sayed. Gold nanoparticles: Optical properties and implementations in cancer diagnosis and photothermal therapy. *Journal of Advanced Research*, 1(1):13–28, 2010.

[18] M Scarselli, P Castrucci, and M De Crescenzi. Electronic and optoelectronic nano-devices based on carbon nanotubes. *Journal of Physics: Condensed Matter*, 24(31):313202, 2012.

[19] Jeroen W G Wilder, Liesbeth C Venema, Andrew G Rinzler, Richard E Smalley, and Cees Dekker. Electronic structure of atomically resolved carbon nanotubes. *Nature*, 391(6662):59–62, 1998.

[20] Kurt Binder. *Monte Carlo and Molecular Dymanics Simulations in Polymers Science*. Oxford University Press, 1995.

[21] M Kotelyanskii and D N Theodorou. *Simulation Methods for Polymers*. Taylor & Francis, 2004.

[22] Jarosaw Meller. Molecular Dynamics. *Encyclopedia of Life Sciences (ELS), John Wiley & Sons*, pages 1–8, 2001.

[23] Erik R Lindahl. Molecular Dynamics Simulations. *Molecular Modeling of Proteins SE - 1*, 443:3–23, 2008.

[24] Godehard Sutmann. *Classical Molecular Dynamics*, volume 10. John von Neumann Institute for Computing, 2002.

[25] Loup Verlet. Computer "Experiments" on Classical Fluids. I. Thermodynamical Properties of Lennard-Jones Molecules. *Phys. Rev.*, 159:98–103, Jul 1967.

[26] Jean M Standard. The Verlet Algorithm for Molecular Dynamics Simulations. *Illinois State University, Chemistry.* (May):1–9, 2013.

[27] G S Grest and Kurt Kremer. Molecular dynamics simulation for polymer in the presence of a heat bath. *Physical Review A*, 33(5):3628–3631, 1986.

[28] Michael P Allen. Introduction to molecular dynamics simulation. *John von Neumann Institute for Computing.*, 23(2):1–28, 2004.

[29] Michael Levitt, Miriam Hirshberg, Ruth Sharon, and Valerie Daggett. Potential energy function and parameters for simulations of the molecular dynamics of proteins and nucleic acids in solution. *Computer Physics Communications*, 91(1-3):215–231, 1995.

[30] James C Phillips, Rosemary Braun, Wei Wang, James Gumbart, Emad Tajkhorshid, Elizabeth Villa, Christophe Chipot, Robert D Skeel, Laxmikant Kalel, and Klaus Schulten. Scalable molecular dynamics with NAMD. *Journal of Computational Chemistry*, 26(16):1781–1802, 2005.

[31] Jay W Ponder and David A Case. Force fields for protein simulations. *Advances in Protein Chemistry*, 66:27–85, 2003.

[32] Jeffery B Klauda, Richard M Venable, J Alfredo Freites, Joseph W O'Connor, Douglas J Tobias, Carlos Mondragon-Ramirez, Igor Vorobyov, Alexander D MacKerell, and Richard W Pastor. Update of the CHARMM All-Atom Additive Force Field for Lipids: Validation on Six Lipid Types. *Journal of Physical Chemistry B*, 114(23):7830–7843, 2010.

[33] Siewert J Marrink, H Jelger Risselada, Serge Yefimov, D Peter Tieleman, and Alex H De Vries. The MARTINI Force Field : Coarse Grained Model for Biomolecular Simulations. *Journal of Physical Chemistry B*, 111(June):7812–7824, 2007.

[34] William Humphrey, Andrew Dalke, and Klaus Schulten. {VMD} – {V}isual {M}olecular {D}ynamics. *Journal of Molecular Graphics*, 14:33–38, 1996.

[35] N Mathews. VMD User′s Guide. page 200, 2012.

[36] M Bhandarkar, A Bhatele, E Bohm, R Brunner, F Buelens, C Chipot, A Dalke, S Dixit, G Fiorin, P Freddolino, P Grayson, J Gullingsrud, A Gursoy, D Hardy, C Harrison, W Humphrey, D Hurwitz, A Hynninen, N Jain, N Krawetz, S Kumar, D Kunzman, J Lai, C Lee, R Mcgreevy, C Mei, M Nelson, J Phillips, B Radak, O Sarood, A Shinozaki, D Tanner, D Wells, G Zheng, and F Zhu. NAMD User ' s Guide. 2016.

[37] Christophe Chipot. Frontiers in free-energy calculations of biological systems. *Wiley Interdisciplinary Reviews: Computational Molecular Science*, 4(1):71–89, 2014.

[38] Giacomo Fiorin, Michael L Klein, and Jérôme Hénin. Using collective variables to drive molecular dynamics simulations. *Molecular Physics*, 111(22-23):3345–3362, 2013.

[39] Eric Darve and Andrew Pohorille. Calculating free energies using average force. *Journal of Chemical Physics*, 115(20):9169–9183, 2001.

[40] Jeffrey Comer, James C Gumbart, Jérôme Hénin, Tony Lelièvre, Andrew Pohorille, and Christophe Chipot. The Adaptive Biasing Force Method: Everything You Always Wanted To Know but Were Afraid To Ask. *The journal of physical chemistry. B*, 119(3):1129–1151, 2014.

[41] M Winterhalter and W Helfrich. Effect of Surface Charge on the Curvature Elasticity. *Journal of Physical Chemistry*, 92:6865–6867, 1988.

[42] Leonid V Chernomordik and Michael M Kozlov. Mechanics of membrane fusion. *Nature structural & molecular biology*, 15(7):675–683, 2008.

[43] Daniel Schmidt and Roderick MacKinnon. Voltage-dependent K^+ channel gating and voltage sensor toxin sensitivity depend on the mechanical state of the lipid membrane. *Proceedings of the National Academy of Sciences of the United States of America*, 105(49):19276–19281, 2008.

[44] H Aranda-Espinoza, A Berman, N Dan, P Pincus, and S A Safran. Interaction between inclusions embedded in membranes. *Biophys. J.J.*, 71(2):648–656, 1996.

[45] Felix Campelo, Harvey T McMahon, and Michael M Kozlov. The Hydrophobic Insertion Mechanism of Membrane Curvature Generation by Proteins. *Biophysical Journal*, 95(5):2325–2339, 2008.

[46] M Tajparast and M I Glavinović. Strain, stress and energy in lipid bilayer induced by electrostatic/electrokinetic forces. *Biochimica et Biophysica Acta (BBA) - Biomembranes*, 1818(3):829–838, 2012.

[47] Tayebeh Jadidi, Hamid Seyyed-Allaei, M Reza Rahimi Tabar, and Alireza Mashaghi. Poisson's Ratio and Young's Modulus of Lipid Bilayers in Different Phases. *Frontiers in bioengineering and biotechnology*, 2(April):8, 2014.

[48] M Parrinello and Rahman A. Crystal Structure and Pair Potentials: A Molecular Dynamics Study. *Physical Review Letters*, 45(14):1196–1199, 1980.

[49] M Parrinello. Polymorphic transitions in single crystals: A new molecular dynamics method. *Journal of Applied Physics*, 52(12):7182, 1981.

[50] J R Ray and A Rahman. Statistical ensembles and molecular dynamics studies of anisotropic solids. *The Journal of Chemical Physics*, 80(1984):4423, 1984.

[51] R N Thurston and K Brugger. Third-Order Elastic Constants and the Velocity of Small Amplitude Elastic Waves in Homogeneously Stressed Media. *Physical Review*, 133(6A):A1604–A1610, 1964.

[52] Tahir Çain and John R Ray. Third-order elastic constants from molecular dynamics: Theory and an example calculation. *Physical Review B*, 38(12):7940–7946, 1988.

[53] M T Dove. *Structure and Dynamics: An Atomic View of Materials*. Oxford Master Series in Condensed Matter Physics 1. OUP Oxford, 2003.

[54] V Hauk. *Structural and Residual Stress Analysis by Nondestructive Methods: Evaluation - Application - Assessment*. Elsevier Science, 1997.

[55] Robert B Best, Xiao Zhu, Jihyun Shim, Pedro E M Lopes, Jeetain Mittal, Michael Feig, and Alexander D MacKerell. Optimization of the Additive CHARMM All-Atom Protein Force Field Targeting Improved Sampling of the Backbone ϕ, ψ and Side-Chain χ 1 and χ 2 Dihedral Angles. *Journal of Chemical Theory and Computation*, 8(9):3257–3273, 2012.

[56] P P Ewald. Die Berechnung optischer und elektrostatischer Gitterpotentiale. *Annalen der Physik*, 369:253–287, 1921.

[57] S Halstenberg, T Heimburg, T Hianik, U Kaatze, and R Krivanek. Cholesterol-induced variations in the volume and enthalpy fluctuations of lipid bilayers. *Biophys J*, 75(1):264–271, 1998.

[58] N I Liu and R L Kay. Redetermination of the pressure dependence of the lipid bilayer phase transition. *Biochemistry*, 16(15):3484–6, 1977.

[59] Gilles Pieffet, Alonso Botero, Günther H Peters, Manu Forero-Shelton, and Chad Leidy. Exploring the local elastic properties of bilayer membranes using molecular dynamics simulations. *The journal of physical chemistry. B*, 118(45):12883–91, 2014.

[60] B Pontes, Y Ayala, A C C Fonseca, L F Romão, and R F Amaral. Membrane Elastic Properties and Cell Function. *PLoS one*, 8(11):1435–1439, 2013.

[61] C C Matthai and N H March. The application of condensed matter methods to the study of the conformation and elastic properties of biopolymers and the transport of DNA through cell membranes. *Theoretical Chemistry Accounts*, 130(4-6):1155–1167, 2011.

[62] N H March and Clarence C Matthai. The application of quantum chemistry and condensed matter theory in studying amino-acids, protein folding and anticancer drug technology. *Theoretical Chemistry Accounts*, 125(3-6):193–201, 2010.

[63] J R Jones, D L G Rowlands, and C B Monk. Diffusion coefficient of water in water and in some alkaline earth chloride solutions at 25 ^{o}C. *Trans. Faraday Soc.*, 61:1384–1388, 1965.

[64] L G Longsworth. The mutual diffusion of light and heavy water. *Journal of Physical Chemistry*, 64(12):1914–1917, 1960.

[65] Jui H Wang. Effect of Ions on the Self-diffusion and Structure of Water in Aqueous Electrolytic Solutions. *The Journal of Physical Chemistry*, 58(9):686–692, 1954.

[66] Jui Hsin Wang. Self-diffusion structure of liquid water. II. Measurement of self-diffusion of liquid water with O18 as tracer. *Journal of the American Chemical Society*, 73(9):4181–4183, 1951.

[67] R Mills. Self-diffusion in normal and heavy water in the range 1-45.deg. *Journal of Physical Chemistry*, 77(5):685–688, 1973.

[68] Manfred Holz, Stefan R Heil, and Antonio Sacco. Temperature-dependent self-diffusion coefficients of water and six selected molecular liquids for calibration in accurate 1H NMR PFG measurements. *Physical Chemistry Chemical Physics*, 2(20):4740–4742, 2000.

[69] Pekka Mark and Lennart Nilsson. Structure and Dynamics of the TIP3P, SPC, and SPC/E Water Models at 298 K. *The Journal of Physical Chemistry A*, 105(43):9954–9960, 2001.

[70] In Chul Yeh and Gerhard Hummer. System-size dependence of diffusion coefficients and viscosities from molecular dynamics simulations with periodic boundary conditions. *Journal of Physical Chemistry B*, 108(40):15873–15879, 2004.

[71] J Postma. Phd thesis (2nd edn.). *University Rijkuniversiteit Groningen, The Netherlands*, 1985.

[72] J J López Cascales, J García de la Torre, S J Marrink, and H J C Berendsen. Molecular dynamics simulation of a charged biological membrane. *Journal of Chemical Physics*, 104(February):2713–2720, 1996.

[73] David J Hardy, Zhe Wu, James C Phillips, John E Stone, Robert D Skeel, and Klaus Schulten. Multilevel summation method for electrostatic force evaluation. *Journal of Chemical Theory and Computation*, 11(2):766–779, 2015.

[74] Andrey A Gurtovenko and Ilpo Vattulainen. Membrane potential and electrostatics of phospholipid bilayers with asymmetric transmembrane distribution of anionic lipids. *Journal of Physical Chemistry B*, 112(15):4629–4634, 2008.

[75] Andrey A Gurtovenko and Ilpo Vattulainen. Ion leakage through transient water pores in protein-free lipid membranes driven by transmembrane ionic charge imbalance. *Biophysical journal*, 92(6):1878–1890, 2007.

[76] Norbert Kučerka, Stephanie Tristram-Nagle, and John F Nagle. Structure of fully hydrated fluid phase lipid bilayers with monounsaturated chains. *Journal of Membrane Biology*, 208(3):193–202, 2006.

[77] D Frenkel and B Smit. Understanding molecular simulation: From algorithms to applications. *Academic Press*, 2001.

[78] E L Cussler. *Diffusion: Mass Transfer in Fluid Systems*. Cambridge Series in Chemical Engineering. Cambridge University Press, 2009.

[79] E Samson, J Marchand, and K A Snuder. Calculation of ionic diffusion coefficients on the basis of migration test results. *Materials and Structures*, 36(257):156–165, 2003.

[80] Jeffrey Comer, Klaus Schulten, and Christophe Chipot. Calculation of lipid-bilayer permeabilities using an average force. *Journal of Chemical Theory and Computation*, 10(2):554–564, 2014.

[81] Rainer A Böckmann, Agnieszka Hac, Thomas Heimburg, and Helmut Grubmüller. Effect of sodium chloride on a lipid bilayer. *Biophysical journal*, 85(3):1647–55, 2003.

[82] Markus S Miettinen, Andrey a Gurtovenko, Ilpo Vattulainen, and Mikko Karttunen. Ion dynamics in cationic lipid bilayer systems in saline solutions. *The journal of physical chemistry. B*, 113(27):9226–9234, 2009.

[83] Jonathan N Sachs and Thomas B Woolf. Understanding the Hofmeister effect in interactions between chaotropic anions and lipid bilayers: Molecular dynamics simulations. *Journal of the American Chemical Society*, 125(29):8742–8743, 2003.

[84] Ilja V Khavrutskii, Alemayehu A Gorfe, Benzhuo Lu, and J Andrew McCammon. Free energy for the permeation of Na^+ and Cl^- ions and their Ion-pair through a zwitterionic dimyristoyl phosphatidylcholine lipid bilayer by umbrella integration with harmonic fourier beads. *Journal of the American Chemical Society*, 131(5):1706–1716, 2009.

[85] Stephen R Popielarski, Suzie H Pun, and Mark E Davis. A nanoparticle-based model delivery system to guide the rational design of gene delivery to the liver. 1. Synthesis and characterization. *Bioconjugate Chemistry*, 16(5):1063–1070, 2005.

[86] Yogesh B Patil, Suresh K Swaminathan, Tanmoy Sadhukha, Linan Ma, and Jayanth Panyam. The use of nanoparticle-mediated targeted gene silencing and drug delivery to overcome tumor drug resistance. *Biomaterials*, 31(2):358–365, 2010.

[87] Robby A Petros and Joseph M DeSimone. Strategies in the design of nanoparticles for therapeutic applications. *Nature Reviews Drug Discovery*, 9(8):615–627, 2010.

[88] Robert Langer. Drug Delivery and targeting. *Nature Reviews*, 1998.

[89] Xiangsheng Liu, Nan Huang, Huan Li, Qiao Jin, and Jian Ji. Surface and size effects on cell interaction of gold nanoparticles with both phagocytic and nonphagocytic cells. *Langmuir : The ACS journal of surfaces and colloids*, 29(9138-9148):9138–9148, 2013.

[90] Agnieszka Z Wilczewska, Katarzyna Niemirowicz, Karolina H Markiewicz, and Halina Car. Nanoparticles as drug delivery systems. *Pharmacological Reports*, 64(5):1020–1037, 2012.

[91] Rainer Fischer, Mariola Fotin-Mleczek, Hansjörg Hufnagel, and Roland Brock. Break on through to the other side-biophysics and cell biology shed light on cell-penetrating peptides. *ChemBioChem*, 6(12):2126–2142, 2005.

[92] Pascale R Leroueil, Stephanie A Berry, Kristen Duthie, Gang Han, Vincent M Rotello, Daniel Q McNerny, James R Baker, Bradford G Orr, and Mark M Banaszak Holl. Wide varieties of cationic nanoparticles induce defects in supported lipid bilayers. *Nano Letters*, 8(2):420–424, 2008.

[93] Andrew D Maynard, Robert J Aitken, Tilman Butz, Vicki Colvin, Ken Donaldson, Günter Oberdörster, Martin a Philbert, John Ryan, Anthony Seaton, Vicki Stone, Sally S Tinkle, Lang Tran, Nigel J Walker, and David B Warheit. Safe handling of nanotechnology. *Nature*, 444(November):267–269, 2006.

[94] Pascale R Leroueil, Seungpyo Hong, Almut Mecke, James R Baker, Bradford G Orr, and Mark M Banaszak Holl. Nanoparticle interaction with biological membranes: Does nanotechnology present a janus face? *Accounts of Chemical Research*, 40(5):335–342, 2007.

[95] Theresa M Allen and Pieter R Cullis. Drug delivery systems: Entering the mainstream. *Science*, 303(5665):1818–1822, 2004.

[96] Jia Qi Lin, Yong Gang Zheng, Hong Wu Zhang, and Zhen Chen. A simulation study on nanoscale holes generated by gold nanoparticles on negative lipid bilayers. *Langmuir*, 27:8323–8332, 2011.

[97] Xiaoyin Xiao, Gabriel A Montaño, Thayne L Edwards, Amy Allen, Komandoor E Achyuthan, Ronen Polsky, David R Wheeler, and Susan M Brozik. Surface charge dependent nanoparticle disruption and deposition of lipid bilayer assemblies. *Langmuir : the ACS journal of surfaces and colloids*, 28(50):17396–403, 2012.

[98] Günter Oberdörster, Eva Oberdörster, and Jan Oberdörster. Nanotoxicology: An emerging discipline evolving from studies of ultrafine particles. *Environmental Health Perspectives*, 113(7):823–839, 2005.

[99] Ivan H El-Sayed, Xiaohua Huang, and Mostafa A El-Sayed. Surface plasmon resonance scattering and absorption of anti-EGFR antibody conjugated gold nanoparticles in cancer diagnostics: Applications in oral cancer. *Nano Letters*, 5(5):829–834, 2005.

[100] Zhi-Yi Zhang and Bradley D Smith. High-generation polycationic dendrimers are unusually effective at disrupting anionic vesicles: membrane bending modell. *Bioconjugate Chemistry*, 11(6):805–814, 2000.

[101] Babak Y Moghadam, Wen Che Hou, Charlie Corredor, Paul Westerhoff, and Jonathan D Posner. Role of nanoparticle surface functionality in the disruption of model cell membranes. *Langmuir*, 28(47):16318–16326, 2012.

[102] Sabina Tatur, Marco Maccarini, Robert Barker, Andrew Nelson, and Giovanna Fragneto. Effect of Functionalized Gold Nanoparticles on Floating Lipid Bilayers. *Langmuir*, 29(22):6606–6614, 2013.

[103] Kai Yang and Yu-Qiang Ma. Computer simulation of the translocation of nanoparticles with different shapes across a lipid bilayer. *Nature Nanotechnology*, 5(8):579–583, 2010.

[104] Xubo Lin, Yang Li, and Ning Gu. Nanoparticle's size effect on its translocation across a lipid bilayer: A molecular dynamics simulation. *Journal of Computational and Theoretical Nanoscience*, 7(1):269–276, 2010.

[105] Francesco Stellacci, Randy P Carney, Reid C Van Lehn, Darrell J Irvine, Alfredo Alexander-Katz, Yu-Sang Yang, and Prabhani U Atukorale. Effect of Particle Diameter and Surface Composition on the Spontaneous Fusion of Monolayer-Protected Gold Nanoparticles with Lipid Bilayers. 13(9):4060–4067, 2013.

[106] Sulin Zhang, Huajian Gao, and Gang Bao. Physical Principles of Nanoparticle Cellular Endocytosis. (9):8655–8671, 2015.

[107] L Whetten Robert, T Khoury Joseph, M Alvarez Marcos, Murthy Srihari, Vezmar Igor, L Wang Z, W Stephens Peter, L Cleveland Charles, D Luedtke W, and Landman Uzi. Nanocrystal gold molecules. *Advanced Materials*, 8(5):428–433, 1996.

[108] Şakir Erkoç. Stability of gold clusters: Molecular-dynamics simulations. *Physica E: Low-Dimensional Systems and Nanostructures*, 8(3):210–218, 2000.

[109] Charles Cleveland, Uzi Landman, Thomas Schaaff, Marat Shafigullin, Peter Stephens, and Robert Whetten. Structural Evolution of Smaller Gold Nanocrystals: The Truncated Decahedral Motif. *Physical Review Letters*, 79(10):1873–1876, 1997.

[110] Ana Vila Verde, Jacqueline M Acres, and Janna K Maranas. Investigating the specificity of peptide adsorption on gold using molecular dynamics simulations. *Biomacromolecules*, 10(8):2118–2128, 2009.

[111] Louise B Wright, P Mark Rodger, Stefano Corni, and Tiffany R Walsh. GolP-CHARMM: First-Principles Based Force Fields for the Interaction of Proteins with Au (111) and Au (100). *Journal of Chemical Theory and Computation*, 9(3):1616–1630, 2013.

[112] Ramon Guixà-González, Ismael Rodriguez-Espigares, Juan Manuel Ramîrez-Anguita, Pau Carriò-Gaspar, Hector Martinez-Seara, Toni Giorgino, and Jana Selent. MEMBPLUGIN: Studying membrane complexity in VMD. *Bioinformatics*, 30(10):1478–1480, 2014.

[113] Cheng Teng Ng, Florence Mei Ai Tang, Jasmine Li, Cynthia Ong, Lanry Lin Yue Yung, and Boon Huat Bay. Clathrin-Mediated Endocytosis of Gold Nanoparticles in *vitro*. *The Anatomical Record*, 298(2):418–427, 2015.

[114] Shekhar Garde, Gerhard Hummer, Angel E Garcia, Michael E Paulaitis, and Lawrence R Pratt. Origin of entropy convergence in hydrophobic hydration and protein folding. *Phys. Rev. Lett.*, 77(24):4966–8, 1996.

[115] William S Young and Charles L Brooks Iii. A reexamination of the hydrophobic effect: Exploring the role of the solvent model in computing the methaneâĂŞmethane

potential of mean force. *The Journal of Chemical Physics*, 106(1997):9265–9269, 1997.

[116] Jeffrey Comer, Ran Chen, Horacio Poblete, Ariela Vergara-Jaque, and Jim E Riviere. Predicting Adsorption Affinities of Small Molecules on Carbon Nanotubes Using Molecular Dynamics Simulation. *ACS Nano*, 9(12):11761–11774, 2015.

[117] Jeffrey Comer, Benoît Roux, and Christophe Chipot. Achieving ergodic sampling using replica-exchange free-energy calculations. *Molecular Simulation*, 40(1-3):218–228, 2014.

[118] T Lelièvre, K Minoukadeh, and Communicated F Otto. Long-time convergence of an adaptive biasing force method. *Nonlinearity*, 21(6):1155, 2008.

[119] Norbert Kučerka, Stephanie Tristram-Nagle, and John F Nagle. Structure of Fully Hydrated Fluid Phase Lipid Bilayers with Monounsaturated Chains. *Journal of Membrane Biology*, 208(3):193–202, 2006.

[120] Barry Isralewitz, Jerome Baudry, Justin Gullingsrud, Dorina Kosztin, and Klaus Schulten. Steered molecular dynamics investigations of protein function. *Journal of Molecular Graphics and Modelling*, 19(1):13–25, 2001.

[121] Yan Gu, Indira H Shrivastava, Susan G Amara, and Ivet Bahar. Molecular simulations elucidate the substrate translocation pathway in a glutamate transporter. *Proceedings of the National Academy of Sciences of the United States of America*, 106(8):2589–2594, 2009.

[122] Marcos Sotomayor, Wilhelm a Weihofen, Rachelle Gaudet, and David P Corey. Structure of a force-conveying cadherin bond essential for inner-ear mechanotransduction. *Nature*, 492(7427):128–32, 2012.

[123] Bo Song, Huajun Yuan, Cynthia J Jameson, and Sohail Murad. Role of surface ligands in nanoparticle permeation through a model membrane: a coarse-grained molecular dynamics simulations study. *Molecular Physics*, 110(February 2014):2181–2195, 2012.

[124] M S Sheel. Coarse graining and multiscale techniques. *University of California Santa Barbara*. pages 1–14, 2009.

[125] Keith D Wilkinson. The discovery of ubiquitin-dependent proteolysis. *Proceedings of the National Academy of Sciences of the United States of America*, 102(43):15280–2, 2005.

[126] Cecile M Pickart and Michael J Eddins. Ubiquitin: Structures, functions, mechanisms. *Biochimica et Biophysica Acta - Molecular Cell Research*, 1695(1-3):55–72, 2004.

[127] Amy Y Shih, Peter L Freddolino, Stephen G Sligar, and Klaus Schulten. Disassembly of nanodiscs with cholate. *Nano Letters*, 7(6):1692–1696, 2007.

[128] H M Berman, J Westbrook, Z Feng, G Gilliland, T N Bhat, H Weissig, I N Shindyalov, and P E Bourne. The Protein Data Bank. *Nucleic acids research*, 28(1):235–242, 2000.

[129] Alexander D Mackerell, Michael Feig, and Charles L Brooks. Extending the treatment of backbone energetics in protein force fields: Limitations of gas-phase quantum mechanics in reproducing protein conformational distributions in molecular dynamics simulation. *Journal of Computational Chemistry*, 25(11):1400–1415, 2004.

[130] Oliviero Carugo and Sándor Pongor. A normalized root-mean-square distance for comparing protein three-dimensional structures. *Protein Science*, 10(7):1470–1473, 2008.

[131] Shityakov Sergey and Dandekar Thomas. Molecular Dynamics Simulation of POPC and POPE Lipid Membrane Bilayers Enforced by an Intercalated Single-Wall Carbon Nanotube. *Nano*, 06(01):19–29, 2011.

[132] Vamshi K Gangupomu and Franco M Capaldi. Interactions of Carbon Nanotube with Lipid Bilayer Membranes. *Journal of Nanomaterials*, 2011:1–6, 2011.

[133] Hongming Wang, Servaas Michielssens, Samuel L C Moors, and Arnout Ceulemans. Molecular dynamics study of dipalmitoylphosphatidylcholine lipid layer self-assembly onto a single-walled carbon nanotube. *Nano Research*, 2(12):945–954, 2009.

[134] K Kostarelos, A Bianco, and M Prato. Promises, facts and challenges for carbon nanotubes in imaging and therapeutics. *Nature nanotechnology*, 4(10):627–633, 2009.

[135] Paul Cherukuri, Sergei M Bachilo, Silvio H Litovsky, and R Bruce Weisman. Near-Infrared Fluorescence Microscopy of Single-Walled Carbon Nanotubes in Phagocytic Cells. *J. Am. Chem. Soc.*, 126:15638–15639, 2004.

[136] Alexandra E Porter, Mhairi Gass, Karin Muller, Jeremy N Skepper, Paul a Midgley, and Mark Welland. Direct imaging of single-walled carbon nanotubes in cells. *Nature nanotechnology*, 2(11):713–7, 2007.

[137] A E Porter, M Gass, J S Bendall, K Muller, and A Goode. Uptake of noncytotoxic acid-treated single-walled carbon nanotubes into the cytoplasm of human macrophage cells. *ACS Nano*, 3(6):1485–1492, 2009.

[138] Vittoria Raffa, Gianni Ciofani, Stephanos Nitodas, Theodoros Karachalios, Delfo D'Alessandro, Matilde Masini, and Alfred Cuschieri. Can the properties of carbon nanotubes influence their internalization by living cells? *Carbon*, 46(12):1600–1610, 2008.

[139] A I Zhbanov, N I Sinitsyn, and G V Torgashov. Nanoelectronic Devices Based on Carbon Nanotubes. *Radiophysics and quantum electronics*, 47(5):435–452, 2004.

[140] Xinluo Zhao, Yoshinori Ando, Yi Liu, Makoto Jinno, and Tomoko Suzuki. Carbon nanowire made of a long linear carbon chain inserted inside a multiwalled carbon nanotube. *Physical Review Letters*, 90(18):187401, 2003.

[141] Przemyslaw Raczynski, Krzysztof Gorny, Mateusz Pabiszczak, and Zygmunt Gburski. Nanoindentation of biomembrane by carbon nanotubes - MD simulation. *Computational Materials Science*, 70:13–18, 2013.

[142] Zygmunt Gburski, Krzysztof Gorny, and Przemyslaw Raczynskii. The impact of a carbon nanotube on the cholesterol domain localized on a protein surface. *Solid State Communications*, 150(9-10):415–418, 2010.

[143] S J Marrink, A H de Vries, and A E Mark. Coarse grained model for semiquantitative lipid simulations. *The Journal of Physical Chemistry*, pages 750–760, 2004.

[144] E Jayne Wallace and Mark S P Sansom. Carbon nanotube/detergent interactions via coarse-grained molecular dynamics. *Nano Letters*, 7(7):1923–1928, 2007.

[145] E Jayne Wallace and Mark S P Sansom. Blocking of carbon nanotube based nanoinjectors by lipids: A simulation study. *Nano Letters*, 8(9):2751–2756, 2008.

[146] Luca Monticelli. On atomistic and coarse-grained models for C60 fullerene. *Journal of Chemical Theory and Computation*, 8(4):1370–1378, 2012.

[147] Jirasak Wong-Ekkabut, Svetlana Baoukina, Wannapong Triampo, I-Ming Tang, D Peter Tieleman, and Luca Monticelli. Computer simulation study of fullerene translocation through lipid membranes. *Nature Nanotechnology*, 3(6):363–368, 2008.

[148] Mickaël Lelimousin and Mark S P Sansom. Membrane perturbation by carbon nanotube insertion: Pathways to internalization. *Small*, 9(21):3639–3646, 2013.

[149] Hui-Hsu Gavin Tsai, Jian-Bin Lee, Jian-Ming Huang, and Ratna Juwita. A molecular dynamics study of the structural and dynamical properties of putative arsenic substituted lipid bilayers. *International journal of molecular sciences*, 14(4):7702–15, 2013.

[150] M T Pakpahan, M Rusmerryani, K Kawaguchi, H Saito, and H Nagao. Evaluation of scoring functions for protein-ligand docking. *AIP Conference Proceedings*, 1518(1), 2013.